FUNDAMENTALS OF KELVIN PROBE FORCE MICROSCOPY AND ITS APPLICATIONS IN THE CHARACTERIZATION OF SOLAR CELLS

by

Fei Lan

Bachelor of Engineering, University of Science and Technology of China, 2011

Submitted to the Graduate Faculty of

Swanson School of Engineering in partial fulfillment

of the requirements for the degree of

Doctor of Philosophy in Electrical Engineering

University of Pittsburgh

2017

UNIVERSITY OF PITTSBURGH

SWANSON SCHOOL OF ENGINEERING

This dissertation was presented

by

Fei Lan

It was defended on

April 7th, 2017

and approved by

William E Stanchina, Ph.D., Professor, Department of Electrical and Computer Engineering

Hong Koo Kim, Ph.D., Professor, Department of Electrical and Computer Engineering

Zhi-Hong Mao, Ph.D., Associate Professor, Department of Electrical and Computer Engineering

Paul W Leu, Ph.D., Associate Professor, Department of Industrial Engineering

Dissertation Director: Guangyong Li, Ph.D., Associate Professor, Department of Electrical and Computer Engineering

FUNDAMENTALS OF KELVIN PROBE FORCE MICROSCOPY AND ITS APPLICATIONS IN THE CHARACTERIZATION OF SOLAR CELLS

Fei Lan, PhD

University of Pittsburgh, 2017

Kelvin probe force microscopy (KPFM) is capable of detecting surface potential (SP) distribution of various materials in nanoscales. Such technique provides quantitative basis for the analysis of electronic properties such as band alignment of semiconductors, junction structure of solar cells and work function of materials. However, because electrostatic force is a long-range force, SP images obtained by KPFM is usually a distorted and blurred reproduction of the real SP distribution of the sample. In this work, KPFM imaging system is modeled as a time-invariant system with measurement equals the convolution of the point spread function (PSF) of the KPFM system with the true SP distribution of the sample. To reverse the distortion, PSF of the KPFM system is first calibrated by comparing the SP distribution of a calibration electrode pair measured by KPFM and the ideal SP distribution simulated with COMSOL. Then, with the calibrated PSF, a non-linear algorithm based on total variation regularization is implemented to reconstruct the SP distribution from the measurements.

In addition, the applications of KPFM in the characterization of solar cells are demonstrated in this work. First, KPFM system is utilized to clarify the electrical role of single walled carbon nanotube (SWNT) in organic solar cells. Usually, SWNTs are introduced in organic solar cells to improve the carrier mobility in these cells. However, the charge transport mechanisms between SWNTs and polymers in organic solar cells are unclear. To clarify the problem, KPFM is utilized in the observation of the SP change in SWNTs when they are placed in hole-enriched and electron-enriched environment. By comparing the SP change of SWNTs, charge transport mechanisms between SWNTs and polymers in organic solar cells are revealed. Finally, KPFM is utilized in the characterization of the cross-sectional surface of planar perovskite solar cells. With the SP profiles of the cross-sectional surface, electric field, junction structures as well as charge injection barriers inside the cells are revealed. These characterizations contribute to the in-depth understanding of the working mechanisms of the solar cell devices, which are valuable for their further optimization.

TABLE OF CONTENTS

LIST OF TABLES

LIST OF FIGURES

PREFACE

This dissertation would not have been possible without the guidance of my committee members, help from my friends and support from my family. First, I would like to express my gratitude to my advisor, Dr. Guangyong Li, for his patient guidance and insightful suggestions during my doctoral program. I really appreciate Dr. William E Stanchina, Dr. Hong Koo Kim, Dr. Zhi-Hong Mao and Dr. Paul W Leu for serving on my committee and providing valuable suggestions for this dissertation.

I thank all my lab members for their kind help and all my friends for the joy they bring along.

Finally, I thank my parents Zhiwei Lan and Tiangui Gu for their unconditional love and support for all these years.

1.0 INTRODUCTION

Kelvin probe force microscopy (KPFM), as an advanced mode of atomic force microscopy (AFM), has been proven to be capable of detecting surface potential (SP) distribution of various materials with a resolution in nanoscales. Such technique provides quantitative basis for the analysis of electronic properties such as band alignment of semiconductors, structure of solar cells, work function of materials and etc. [1-3].

KPFM measures the contact potential difference between the sample and the KPFM probe by detecting the electrostatic force between them. However, because electrostatic force is a long-range force, SP image obtained by KPFM is usually a distorted and blurred reproduction of the real SP distribution of the sample surface [4]. A widely accepted model of how this long-range electrostatic force affects the measurements of KPFM was derived by Jacobs et al. in 1998 [5], where they modeled the interaction between the probe and the sample surface as a set of ideal conductors with mutual capacitances. The calculation of capacitances was then completed with an assumption of uniform magnitude electric field along the field lines. Strassburg et al., on the other hand, developed an electrostatic force model based on a boundary element method [6]. As demonstrated in their work, the PSF of a system with specific probe shape and tip-sample distance could be derived by modeling the sample surfaces as dipole layers with difference charge densities. Several other works have also reported on the simulation of PSF and its application in the deconvolution of KPFM signals [7, 8]. To make the problem solvable, most of the simulations assume a regular probe with symmetric shape [6-8]. Based on such assumption, the resultant PSF will be an estimation of the actual system PSF but not the accurate one. Taking into consideration the real probe shape, a new approach to experimentally calibrate the PSF of our KPFM system is developed. In this work, PSF of our KPFM system is calibrated by comparing the SP distribution of a calibration electrode pair measured by KPFM and the ideal SP distribution simulated with COMSOL. Then, with the calibrated PSF, KPFM images are reconstructed using a non-linear algorithm based on total variation regularization.

The other aspect of this work is the application of KPFM in the characterization of solar cells. With a resolution in nanoscales, KPFM is a useful tool in revealing the working mechanisms of semiconductor devices. In this work, KPFM is first utilized in the observation of SP change of single-walled carbon nanotube (SWNT) in hole-enriched and electron-enriched environment, through which the charge transport mechanisms in SWNT doped organic solar cells are revealed. In addition, cross-sectional surfaces of perovskite solar cells are characterized with KPFM, with the acquired SP profiles, electric field distribution inside the solar cells are revealed, junction structures of the solar cells are clarified and charge injection barriers that undermine the performance of the cells are identified. In all, KPFM measurements are essential in the understanding of working mechanisms of semiconductor devices which provide important guidance for the design and optimization of these devices.

1.1 INTRODUCTION TO ATOMIC FORCE MICROSCOPY

AFM is one kind of the scanning probe microscopies that are widely used in the surface characterizations. The first demonstration of AFM appeared in 1986 when Binnig and Quate utilized a probe with a ultra-small tip at the end of a cantilever to raster scan the sample surface [9]. In 1987, Wickramasinghe et al. modified the previous technique with a setup that uses a vibrating tip in close proximity to the sample surface and optical heterodyne to accurately measure the vibration. They demonstrated a lateral resolution of 50 Å with the new setup [10] . Modern AFM utilizes a piezo actuated probe to interact with the sample surface and measure sample surface topography. With this very basic setup, there are many advanced modes that can be realized through modifying the setup of AFM. These include current AFM (C-AFM) [11], scanning capacitance microscopy (SCM) [12], electrostatic force microscopy (EFM) [13], scanning spread resistance microscopy (SSRM) [14], KPFM and etc.. These advanced modes of AFM enable the characterization of other physical properties along with the topography. C-AFM for example, enables the measurement of current through probe and sample, providing information concerning spatial distribution of conductivity of the sample [11]; SCM, on the other hand, provides information concerning local capacitance between the sample surface and the probe [15]. In this thesis, one of the most commonly used advanced modes, KPFM, is mainly discussed and used in the characterization.

1.2 INTRODUCTION TO KELVIN PROBE FORCE MICROSCOPY

KPFM is widely used in the characterization of semiconductors, nanostructures as well as electrical devices. Different from the basic AFM mode where the probes are usually non-conductive, probes used in KPFM are coated with conductive metal such as Pt and Ir so that DC voltages can be applied to the probe through kelvin controller. Modern KPFM technique is developed from classic kelvin probe technique, a contactless method that measures the contact potential different between the probe and the sample.

1.2.1 Classic Kelvin Probe technique

In classic kelvin probe technique, sample under test is positioned at a certain distance from the conductive probe, forming a capacitor which can be approximated using a parallel-plate module, as demonstrated in Figure 1.1. A mechanical oscillation is then applied to the capacitor, causing the distance between the probe and the sample to change which can be expressed as:

$$d = d_0 + d_m \cos(\omega_m t) \tag{1.1}$$

where d_0 is the oscillation equilibrium position, d_m is the oscillation amplitude, and ω_m is oscillation frequency. The capacitance between the probe and the sample can be expressed as:

$$C(\mathrm{t}) = \frac{\varepsilon S}{d} = \frac{\varepsilon S}{d_0 + d_m \cos(\omega_m t)} \tag{1.2}$$

in which ε is the electric permittivity and S is the area of the probe.

Due to the mechanical oscillation introduced to the parallel capacitor system, current is generated in this system and is expressed as:

$$i(\mathrm{t}) = \frac{d}{dt}(CV_{CPD}) = V_{CPD}\frac{dC}{dt} \tag{1.3}$$

where C is capacitance between the probe and the sample which is expressed in Equation 1.2 and V_{CPD} is the contact potential difference between the probe and the sample.

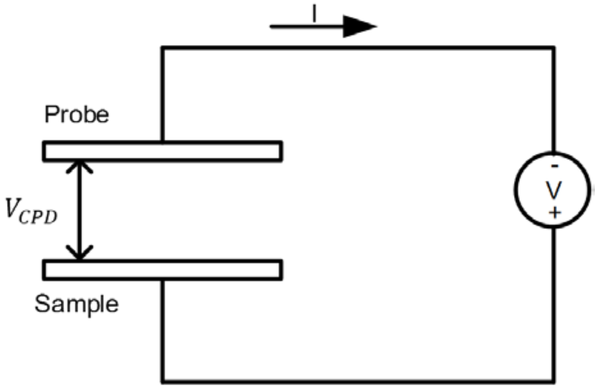

Figure 1.1. Schematic of classic kelvin probe technique.

Suppose V_{CPD} is not zero, which means there exists contact potential difference between the probe and the sample, according to Equation 1.3, current will be generated in the circuit. To measure the contact potential difference V_{CPD} between the probe and the sample, a bias voltage is usually applied in between the probe and the sample as shown in Figure 1.1, then the expression for the current generated in the circuit is modified as:

$$i(\mathrm{t}) = \frac{d}{dt}C(V_{CPD} - V) = (V_{CPD} - V)\frac{dC}{dt} \tag{1.4}$$

To nullify the current in the circuit, the bias voltage should satisfy V=V_{CPD}. In this way, V_{CPD} can measured by recording the DC bias that nullifies the current.

Similar technique is adopted in the realization of KPFM.

1.2.2 Working Principle of Kelvin Probe Force Microscopy

In KPFM system, a DC voltage V_{dc} together with an AC voltage V_{ac} (at electric frequency ω_e) are applied to its conductive probe as bias signal which can be expressed as [16]:

$$V = V_{dc} + V_{ac}\sin(\omega_e t) \tag{1.5}$$

With this bias signal, the electrostatic force between the probe and the sample can be express as:

$$F = \frac{1}{2}\frac{\partial C}{\partial z}[(\emptyset + V_{dc})^2 + \frac{1}{2}V_{ac}^2 + 2(\emptyset + V_{dc})V_{ac}\sin(\omega_e t) - \frac{1}{2}V_{ac}^2\cos(2\omega_e t)] \quad (1.6)$$

where C and $\emptyset$ are the capacitance and contact potential difference between the probe and the sample surface, respectively. Because lock-in amplifiers are insensitive to DC component and 2nd harmonic term ($2\omega_e$) does not contain information concerning contact potential difference $\emptyset$, the first harmonic term is utilized in the measurement of contact potential difference, and is expressed as:

$$F(\omega_e) = \frac{\partial C}{\partial z}(\emptyset + V_{dc})V_{ac}\sin(\omega_e t) \quad (1.7)$$

This term causes the KPFM probe to oscillate at electrical frequency ω_e. If DC bias V_{dc} is controlled through the feedback loop to the point where $V_{dc} = -\emptyset$, oscillation amplitude at ω_e is nullified. Then by recording the feedback signal V_{dc} we will be able to measure the contact potential difference between the KPFM probe and the sample surface.

KPFM has a history of 26 years up to now [17], during which two basic scanning modes have been developed: single-pass scan and dual-pass lift-up scan. For dual-pass lift-up scan, topography image is obtained by tapping mode in the first scan, and SP images are obtained in the second scan when the probe is lift up to follow the topography. On the other hand, for single-pass scan, topography image as well as SP distribution of the sample surface are obtained simultaneously in a single scan. It is believed that spatial resolution of the single-pass scan is higher than that of dual-pass lift-up scan because topographical errors caused by electrostatic force are minimized for single-pass scan due to the active suppressing of electrostatic force during the scan process [16].

In this work, single-pass scan mode was utilized with AFM model SPM 5500 by Agilent. Traditionally, single-pass scan was implemented in a noncontact AFM mode which limits the

KPFM to smooth surface in vacuum condition and at a low speed. The ambient single-pass scan KPFM was first achieved by Ziegler et al. using amplitude modulation (AM) detection in feedback loop [18], but now, KPFM can also be performed with frequency modulation (FM) detection.

Schematic of both amplitude modulation KPFM (AM-KPFM) and frequency modulation KPFM (FM-KPFM) are shown in Figure 1.2. In AM-KPFM, lock-in amplifier A1 (LIA1) and lock-in amplifier A2 (LIA2) are connected in parallel. LIA1 helps maintain the oscillation amplitude of the KPFM probe at mechanical frequency ω_m by adjusting tip-sample distance. While for LIA2, lock-in frequency is at electric frequency ω_e and by adjusting the DC biases applied to the conductive probe, electrostatic force between the tip and the sample at frequency ω_e is nullified, and the contact potential difference between KPFM probe and the sample surface is recorded.

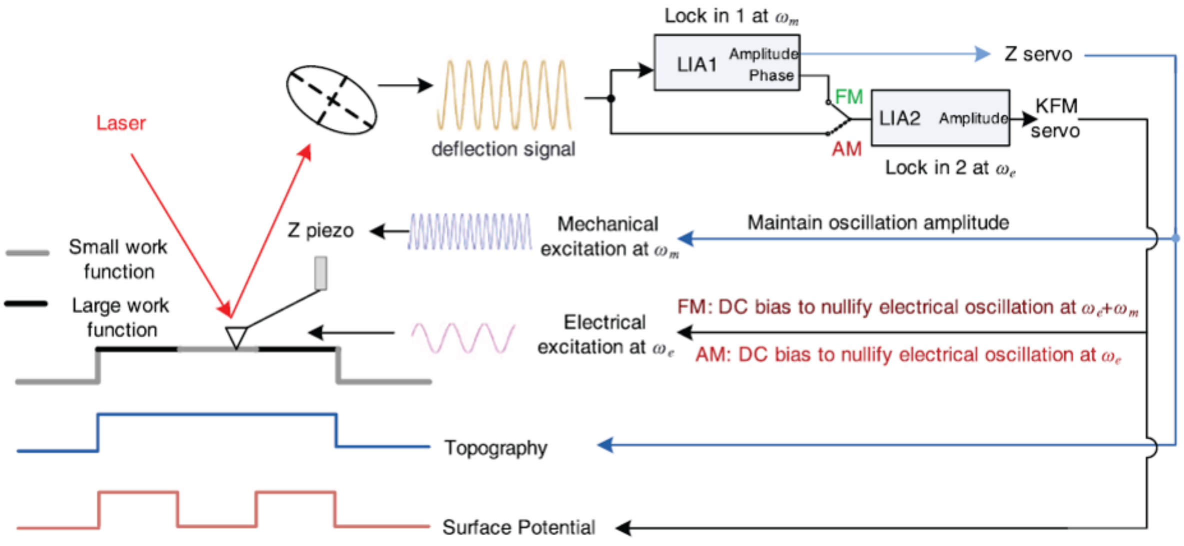

Figure 1.2. Working principle of KPFM (AM-KPFM mode and FM-KPFM mode).

On the other hand, for FM-KPFM, LIA1 and LIA2 are connected in series where the output signal from LIA1 is sent to LIA2 as input. Similar to AM-KPFM, in FM-KPFM, LIA1 works at

ω_m and acquires topography image by adjusting tip-sample distance to maintain a constant oscillation amplitude. However, LIA2 in FM-KPFM detects and nullify oscillation at $\omega_m \pm \omega_e$ to measure the contact potential difference.

Compared with AM-KPFM, FM-KPFM usually has a higher resolution because it detects force gradient which is more confined to the proximity of the tip apex. However, for SPM5500 system, the setup of FM-KPFM has higher complexity than AM-KPFM and AM-KPFM are still widely used in the nanoscale characterization. Hence, this work focuses on the improvement of resolution and the applications of AM-KPFM.

1.3 MOTIVATION AND DISSERTATION ORGANIZATION

Although KPFM has a resolution in nanoscale, its lateral resolution and accuracy is degraded by the averaging effect of PSF [8]. With broader application and more demanding characterization work, the need to improve its resolution is urgent. In addition, with the versatile SPM 5500 system, various characterization conditions can be set up and various characterization work can be fulfilled. In this thesis, we first demonstrate a systematic method to improve the resolution and accuracy of KPFM images and then the application of our SPM 5500 system is demonstrated with the characterization work performed on solar cells.

The organization of this thesis is as follows: in chapter 1, background of this thesis, working principle of KPFM and the motivation for this work are introduced. In chapter 2, PSF of our KPFM system is calibrated experimentally and the corresponding results are used in the deconvolution of KPFM images. Chapter 3 presents the application of KPFM in the characterization of the charge transport mechanisms between SWNTs and polymers in organic solar cells. Chapter 4 is another application of KPFM where the cross-sectional surfaces of perovskite solar cells are characterized by KPFM to reveal the junction structure, charge transport mechanisms as well as charge injection barriers in these cells. Chapter 5 concludes the thesis and discusses about the future work.

2.0 DECONVOLUTION OF KPFM IMAGES

Because electrostatic force is a long-rang force, SP measurement obtained by KPFM is usually a blurred and distorted reproduction of the real SP distribution of the sample surface. To reconstruct the SP images from the blurred measurements, PSF of the KPFM system as well proper deconvolution algorithms are needed. In this chapter, a novel approach to experimentally calibrate the PSF of our KPFM system is presented. This calibration method not only provides a direct way to obtain the PSF, but also improves the accuracy of the PSF by taking into account the real probe shape. The calibrated PSF is then applied to a total variation regularization based non-linear deconvolution algorithm for the reconstruction of SP images. This iterative deconvolution algorithm improves the resolution of KPFM measurement while suppressing noises, which greatly helps the interpretation of KPFM data.

2.1 KPFM IMAGING MODEL AND POINT SPREAD FUNCTION

Due to the long-range electrostatic force, KPFM imaging system is modeled as the convolution of the SP distribution of the sample and the PSF of the imaging system. As expressed in Equation 2.1,

$$g(x,y) = f(x,y) * h(x,y) + n(x,y) \tag{2.1}$$

where $g(x,y)$ is the KPFM measurement, $f(x,y)$ is the true SP distribution of the sample, $h(x,y)$ is the PSF of the imaging system and $n(x,y)$ is the additive noise. The convolution process often results in the blurring of acquired images, leading to the decrease in resolution and loss of fidelity of the measurements. The degradation of resolution is demonstrated with a simulated PSF based on Strassburg's electrostatic force model [6]. Shown in Figure 2.1 (a) is the simulated PSF with a tip-sample distance of 5 nm. The profile of the probe used in the calculation is composed of two parts—a conical shaped body and a hemispherical shaped tip end. Tip length is chosen to be 10 um and tip radius is 15 nm based on typical manufacture's data [16]. As reported in our previous work, if feature size under test is too small, there will be a large discrepancy between sample's true SP and SP acquired by KPFM. Results are recreated in Figure 2.1 (b) where the simulated KPFM measurements of circular electrodes are shown. In the simulation, we assumed a uniform SP of 1 V on the electrode and 0 V on the rest of the sample. Also, the radiuses of the electrodes were varied to demonstrate the correlation between feature size and KPFM accuracy. From Figure 2.1 (b), it can be concluded that smaller feature size results in a larger discrepancy between KPFM measurement and the actual SP due to the averaging effect of PSF. From the simulation, with this specific tip-sample system, feature radius of at least 50 nm is needed for an accurate measurement. Figure 2.1 (c) demonstrates the degradation of resolution caused by KPFM imaging process. When two small features are closely located, only one blurred and broaden feature can be detected in the KPFM measurement due to the convolution with the PSF. Such blurring caused by PSF often leads to the misinterpretation and misunderstanding of the measurement data.

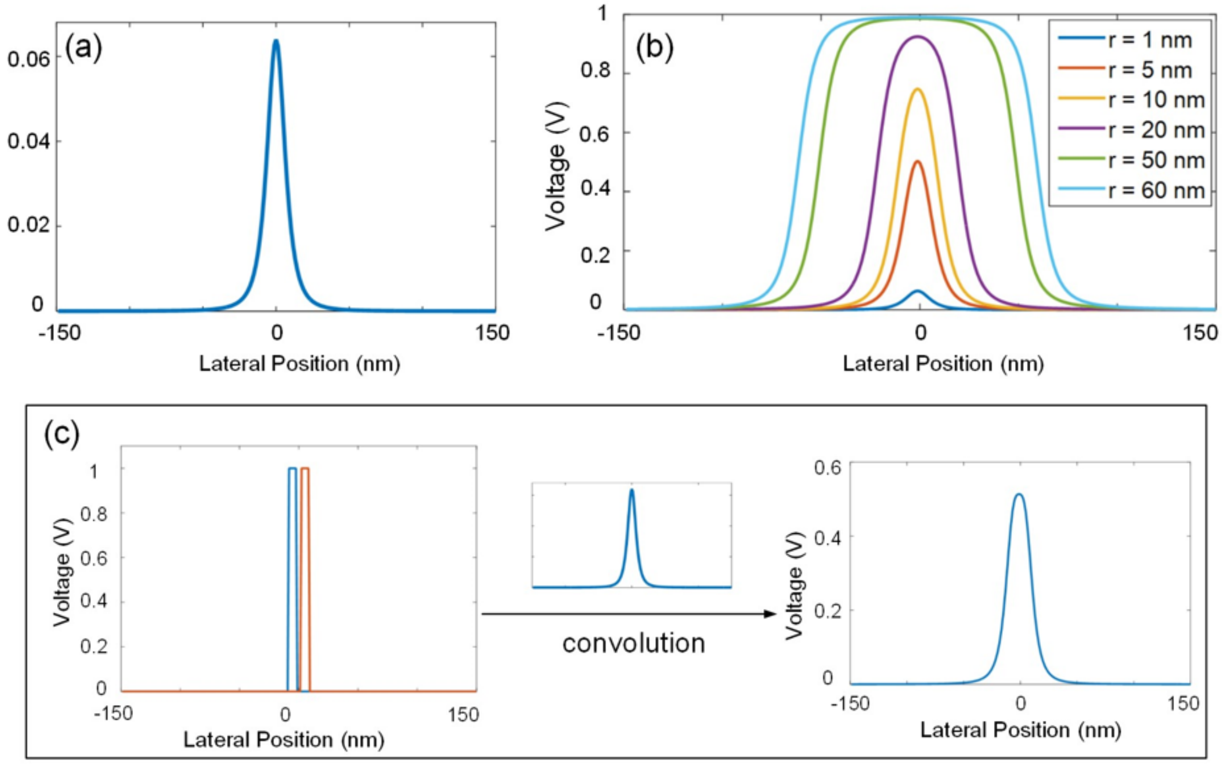

Figure 2.1. Demonstration of the averaging effect of PSF in KPFM imaging system. (a) Simulated PSF with tip-sample distance of 5 nm, tip apex radium of 15 nm and tip height of 10 um; (b) The simulated KPFM measurements of electrodes with 1 V applied voltage with respect to their radiuses r as labeled in the figure; (c) Demonstration of degradation in resolution caused by convolution process.

2.2 EXPERIMENTAL CALIBRATION OF THE PSF

Based on Strassburg's electrostatic force model, PSF of a KPFM imaging system is largely dependent on the probe shape. To make the problem solvable, most of the simulations assume the probes used in the measurement to have simple geometry and are symmetric [6, 8]. With such assumption, the simulated PSF will be an estimation of the actual system PSF but not the accurate one. In this section, instead of simulation, a new approach to experimentally calibrate the PSF of our KPFM system is presented.

2.2.1 Fabrication and characterization of calibration electrode

The calibration electrode pair used in this work was fabricated with standard photolithography and E-beam lithography process on a silicon substrate with 150 nm thick silicon oxide layer. A pair of electrodes was first fabricated through photolithography, then, more delicate features were patterned by E-beam lithography, as demonstrated in Figure 2.2. The metal used for our electrode pair is palladium (Pd) considering its good stability as well as smooth metal surface. The final electrode pair has a thickness of 50 nm with Pd deposited by an E-beam evaporator.

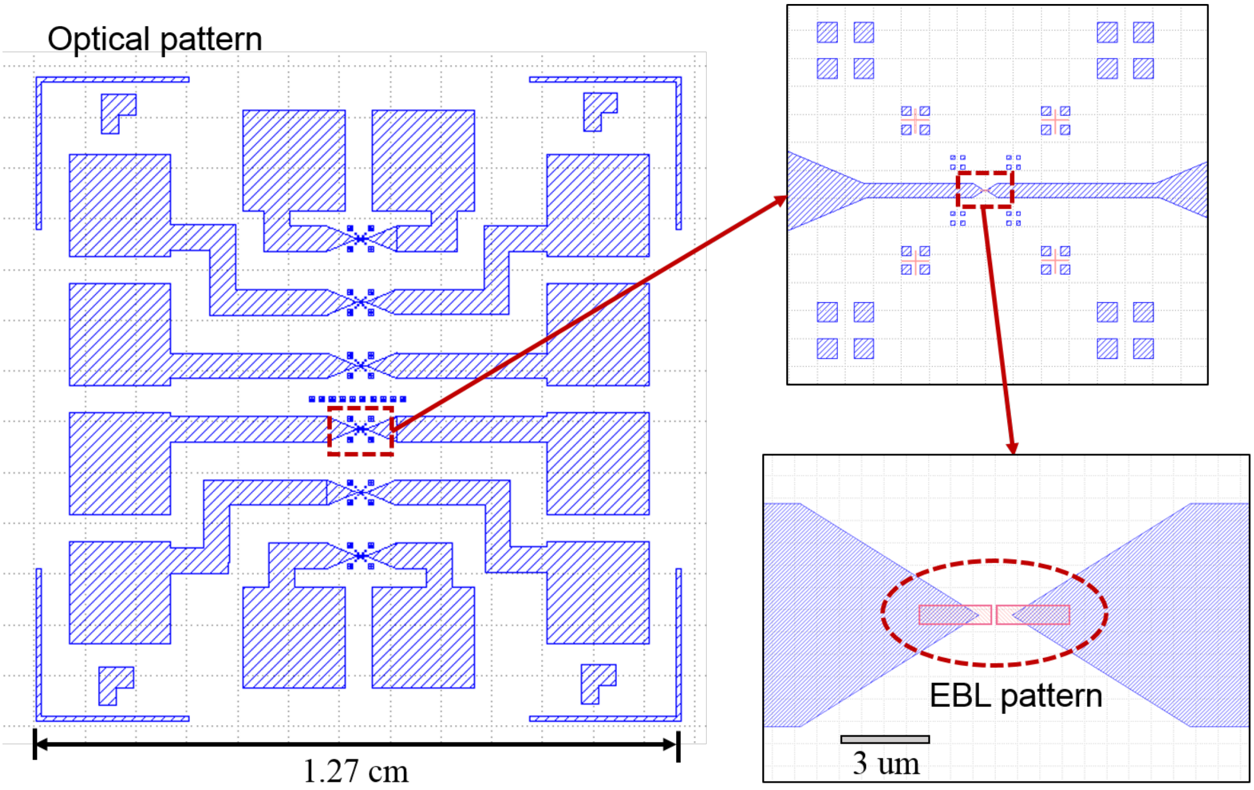

Figure 2.2. Pattern design of the calibration electrode pair. The gap between the electrode pair fabricated by photolithography is around 3 μm, E-beam lithography was used to reduce the gap to several hundred nanometers by patterning a pair of rectangular electrode in-between.

KPFM measurement was carried out with Agilent SPM 5500 system using SCM-PIT KPFM probe fabricated by Bruker. The electric oscillation frequency used was 13.311 KHz and the tip-sample distance calculated from force distance curve is 31 nm. In KPFM measurement, the two electrodes were biased with specific voltages supplied by a voltage source, as shown in Figure 2.3, and the electrode pair was placed perpendicular to the KPFM probe. The relative position between the sample and the KPFM probe is important because, unlike the results obtained from simulations, real PSF of a tip-sample system is not rotationally symmetric.

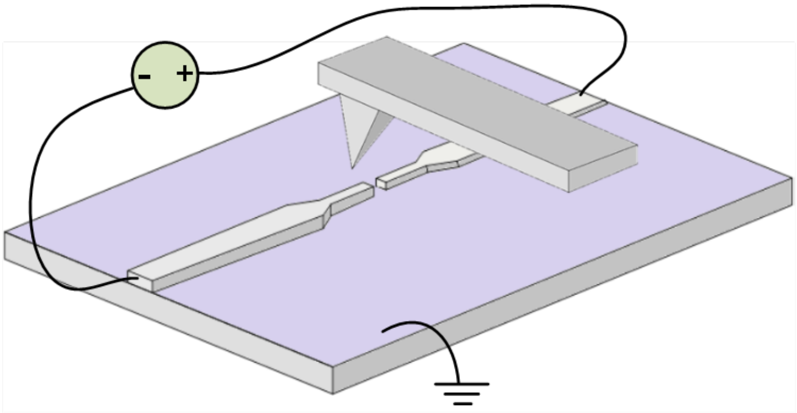

Figure 2.3. Schematic of the setup of the calibration system.

The topography of the calibration electrode is shown in Figure 2.4 (a). Because silicon oxide is non-conductive, charges could be trapped on silicon oxide surface, especially at edges of the fabricated patterns. However, since the trapped charges do not migrate with different biases, the subtraction of SP signals with different biases can help to eliminate the SP signal caused by trapped charges. To do so, KPFM measurement was first performed when both electrodes were biased at 0 V, the corresponding SP image is shown in Figure 2.4 (b). Then KPFM measurement was taken when the left electrode was biased at -1 V while the right electrode was biased at +1 V, the corresponding SP measurement is shown in Figure 2.4 (c). The subtraction of these two measurements removes SP signals caused by trapped charges and gives the corrected SP distribution of the calibration sample with -1 V bias on the left electrode and +1 V bias on the right electrode. After noise removal using median filter, the corrected KPFM result is shown in Figure 2.4 (d).

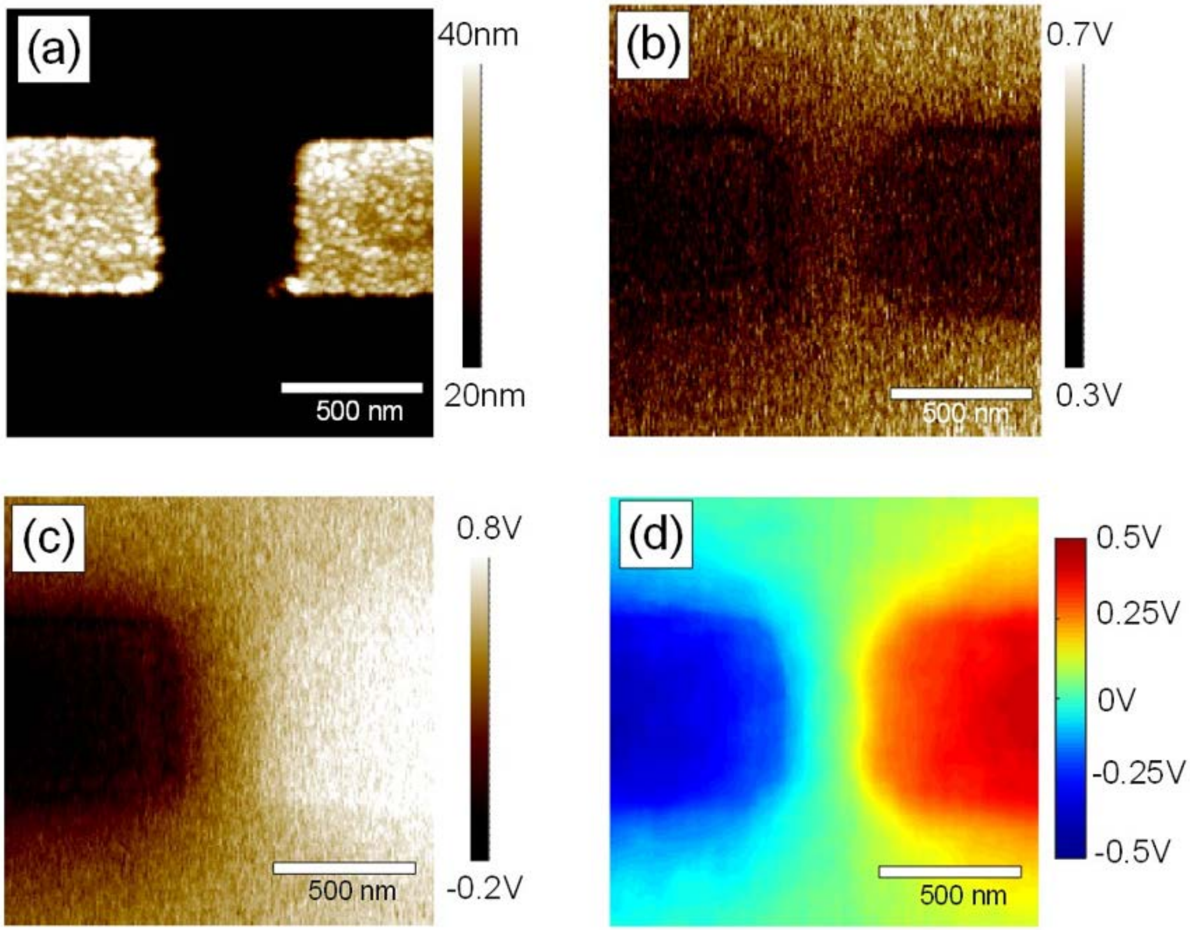

Figure 2.4. KFPM measurement of calibration electrode pair. (a) Topography image of the calibration electrode pair; (b) SP image of the calibration electrode pair with 0 V bias at both electrodes; (c) SP image of the calibration electrode pair with -1 V bias on the left electrode and +1 V bias on the right electrode; (d) SP image of the calibration electrode pair with corrected SP distribution.

2.2.2 Simulation of ideal SP of calibration electrode

After acquiring KPFM measurement of the calibration electrode pair, the ideal SP distribution of the calibration electrode pair was simulated in COMSOL. Topography image of the calibration electrode was imported into COMSOL and the electrode model was built based on the outline of the measured electrode shape. Sharpe edges in the topography image were smoothed to make the simulation tolerable with COMSOL. Other parameters such as metal thickness, substrate dielectric etc. were also incorporated into COMSOL software. Initial voltages applied to the electrode model were again -1 V on left electrode and +1 V on right electrode, respectively. Zero charge were used as the boundary condition to compute SP distribution with no surface charge. And charge conservation node was added to include equations for charge conservation based on Gauss' law. Finally, with coarse mesh at locations far from electrode center and a much finer mesh compared to electrode size in electrode center, simulation of SP distribution was obtained. Simulation was performed with a much larger area of 200 um by 100 um than the size of KPFM measurement, which is 1.5 um by 1.5 um to ensure its fidelity. Simulation result is shown in Figure 2.5. The inset figure is a zoomed-in image with the same size to our KPFM measurement, which is also the ideal SP distribution of our calibration electrode with this specific bias.

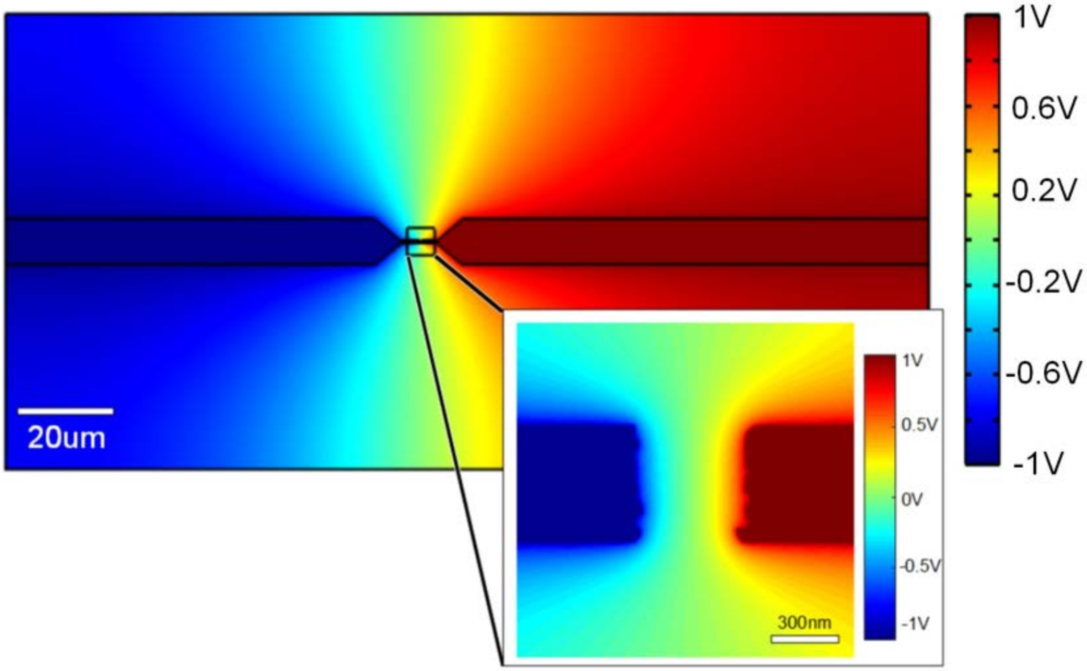

Figure 2.5. Simulated SP distribution of the calibration electrode pair with left electrode biased at -1 V and right electrode biased at +1 V. Simulation is completed in COMSOL software. Inset figure is a zoomed-in image with the same size as our KPFM measurement.

2.2.3 Experimentally calibrate PSF of the KPFM system

With acquired KPFM measurement and simulated ideal SP distribution of our calibration electrode pair, Lucy-Richardson (L-R) algorithm was applied to calibrate the PSF of our system. L-R algorithm is an iterative algorithm with iteration process being described as [19]:

$$h_{m+1}(x,y) = h_m(x,y)\left[f(-x,-y) * \frac{g(x,y)}{f(x,y) * h_m(x,y)}\right] \tag{2.2}$$

where $h_i(x,y)$ is the estimation of the PSF of our system at *ith* iteration; $f(x,y)$ is the ideal SP distribution of the calibration electrode with $f(-x,-y)$ being its corresponding adjoint matrix and

$g(x,y)$ is the measured SP distribution. The basic idea of this iteration process is to calculate the most likely $h_i(x,y)$ with known $f(x,y)$ and observed $g(x,y)$. The iteration process was implemented with functions available in MATLAB.

The calibrated PSF is shown in Figure 2.6. Figure 2.6 (a) is the calibrated PSF, Figure 2.6 (b) is its top view and Figure 2.6 (c) is the SEM image of a SCM-PIT probe provided by Bruker [20]. As can be seen from the calibrated PSF, different from the Gaussian-like, symmetric PSF typically obtained from simulations [6], the real PSF is asymmetric. Also, the shape of the calibrated PSF mimics the geometry of the probe used in the measurement. This agrees with our understanding that the shape of a PSF is dependent on the profile of the probe being used. Later, with this calibrated PSF, reconstruction algorithm is applied to reverse the blurring effect of PSF and reconstruct SP images.

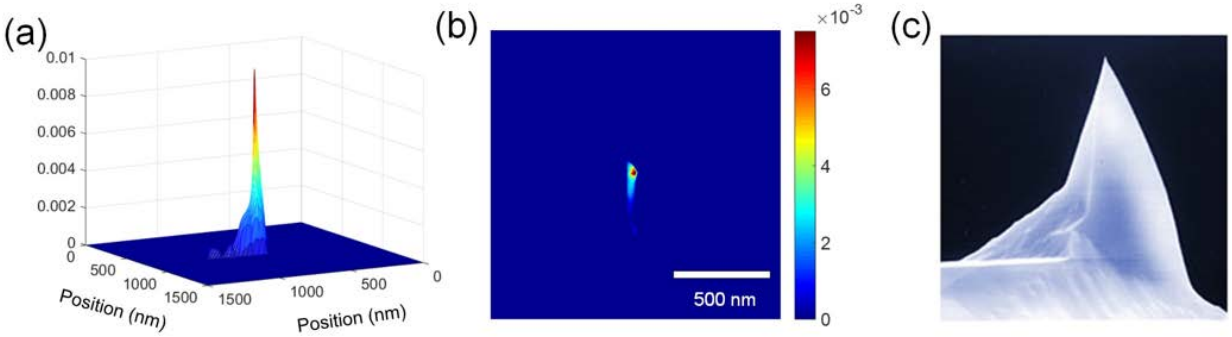

Figure 2.6. Calibration results of the PSF. (a) Calibrated PSF of the Agilent 5500 SPM system with SCM-PIT KPFM probe; (b) Top view of the calibrated PSF; (c) SEM image of the SCM-PIT KPFM probe tip provided by Bruker website [20].

2.3 DECONVOLUTION OF KPFM IMAGES WITH TOTAL VARIATION REGULARIZATION BASED NONLINEAR ALGORITHM

In this section, a nonlinear algorithm based on total variation regularization is used in the reconstruction of KPFM image. The reason for the choice of nonlinear algorithm instead of the linear ones is that nonlinear reconstruction method is much better at conserving the resolution of the original signals. SP images of both 1-D and 2-D materials are used in the deconvolution process to demonstrate the effectiveness of our deconvolution algorithm.

2.3.1 Nonlinear deconvolution algorithm based on total variation regularization

We can formulate an optimization problem to retrieve the SP signals f from the blurred KPFM measurement g with the calibrated PSF h. The optimization problem is equivalent to the minimization of the following function:

$$\min \quad \{\frac{\lambda}{2}\left||f(x,y) * h(x,y) - g(x,y)|\right|^2 + \left||\nabla f(x,y)|\right|_1\} \qquad (2.3)$$

where ||·|| denotes vector 2-norm and $||\cdot||_1$is the vector 1-norm. The first term of this function is to force the reconstructed result to be the most likely estimation of the undistorted signal. The second term is the total variation regularization which helps to smooth reconstructed signals and eliminate noise. The balance between these two terms is achieved with parameter λ which is a positive real number. Intuitively, it can be concluded from Equation 2.3 that with a larger λ, more stress will be on the first term and reconstructed result will be more constrained to resemble the estimation of the undistorted image. On the other hand, a smaller λ emphasizes the suppressing of noise level but could lead to the loss of fidelity in reconstructed signals. Usually, the optimal value of λ is chosen based on specific images under processing and might vary greatly with different images.

To solve the optimization problem, augmented Lagrangian method was used. Since convolution is a linear operation, it can be expressed with matrices. Now denoting that the convolution with PSF $h(x, y)$ is associated with an operator H, and introducing u as the intermediate variable, the optimization problem is equivalent to [21, 22]:

$$\min_{f,u} \frac{\lambda}{2}||\mathrm{H}f - g||^2 + ||u||_1, \text{ subject to } u = \nabla f \tag{2.4}$$

and the corresponding augmented Lagrangian problem can be written as:

$$L(f, u, y;\ \lambda, \beta) = \frac{\lambda}{2}||\mathrm{H}f - g||^2 + ||u||_1 - z^T(u - \nabla f) + \frac{\beta}{2}||u - \nabla f||^2 \tag{2.5}$$

where z is the Lagrange multiplier associated with constraint $u = \nabla f$, and β is the regularization parameter associated with penalty term $||u - \nabla f||^2$. To find the saddle point of this problem, the alternating direction method was used to solve the following sub-problems iteratively [23]:

$$f_{k+1} = \arg\min_{f} \frac{\lambda}{2}||\mathrm{H}f - g||^2 - z_k^T(u_k - \nabla f) + \frac{\beta}{2}||u_k - \nabla f||^2 \tag{2.6}$$

$$u_{k+1} = \arg\min_{u} ||u||_1 - z_k^T(u - \nabla f_{k+1}) + \frac{\beta}{2}||u - \nabla f_{k+1}||^2 \tag{2.7}$$

$$z_{k+1} = z_k - \beta(u_{k+1} - \nabla f_{k+1}) \tag{2.8}$$

To solve the f-subproblem, we find the optimality condition of Equation 2.6:

$$\frac{\partial L}{\partial f} = \lambda \mathrm{H}^T(\mathrm{Hf} - \mathrm{g}) + \nabla^T z - \beta \nabla^T(u - \nabla f) = 0 \tag{2.9}$$

Performing Fourier transform to Equation 2.9, we obtain the solution to the f-subproblem [23]:

$$f = \mathcal{F}^{-1}\left[\frac{\mathcal{F}[\lambda \mathrm{H}^T g + \beta \nabla^T u - \nabla^T z]}{\lambda|\mathcal{F}[\mathrm{H}]|^2 + \beta|\mathcal{F}[\nabla^2]|}\right] \tag{2.10}$$

The solution to u-subproblem has a closed form of [24, 25]:

$$u_{x,y} = \begin{cases} \left(1 - \frac{1}{\beta}\frac{1}{||w||}\right) w_{x,y}, & ||w|| > \frac{1}{\beta} \\ 0, & ||w|| \leq \frac{1}{\beta} \end{cases} \tag{2.11}$$

where $w_{x,y} = \nabla_{x,y} f + \frac{1}{\beta} z_{x,y}$ and represents the x and y component of the matrix w, respectively. With solutions to the subproblems and initial values of $f_0 = g, u_0 = \nabla f_0$, f and u can be updated iteratively. The Lagrange multiplier z is also calculated in each iteration using Equation 2.8. Convergence was checked at the end of each iteration using $\varepsilon = ||f_{k+1} - f_k||^2 / ||f_k||^2$: if ε is less than the predefined tolerance, the iteration ends. The tolerance used in this work is 10^{-6}.

2.3.2 Deconvolution results

Using the deconvolution algorithm mentioned above, we demonstrate the successful deconvolution of SP images of a Zinc Oxide (ZnO) nanorod (1-D material) and a graphene oxide flake (2-D material) on semiconductor polymer surface. They are chosen because of their availability in our lab.

Firstly, the deconvolution of SP image of a nanorod using the total variation regularization algorithm is demonstrated. Figure 2.7 shows the deconvolution results. Figure 2.7 (a) is the topography image of a ZnO nanorod on poly(3-hexylthiophene-2,5-diyl) (P3HT) and Phenyl-C61-butyric acid methyl ester (PCBM) blend and Figure 2.7 (b) is the corresponding SP image. Due to the band alignment between ZnO and P3HT/PCBM polymer blend, electrons were accumulating at ZnO/polymer interfaces. This can be observed from Figure 2.7 (b) where the interfaces of ZnO and P3HT/PCBM are much darker than the rest of the image, indicating the accumulation of electrons. To deconvolute the measured SP image, we first reconstructed the SP image in

MATLAB, as shown in Figure 2.7 (c). Reconstruction algorithm was then applied to the SP data and the deconvoluted image is shown in Figure 2.7 (d). Figure 2.7 (c) and Figure 2.7 (d) have the same colormap and color scale, providing a direct comparison between the original measurement and the deconvoluted image. Compared to Figure 2.7 (c), noises in Figure 2.7 (d) were reduced; also, the electron accumulation at the interfaces between ZnO and P3HT/PCBM is much more obvious and clearer, which is an indication of resolution improvement. Cross sections (indicated by the black dashed lines drawn on Figures 2.7 (c) and (d)) are shown in Figure 2.7 (e) for a closer observation. In Figure 2.7 (e), the blue dashed curve is the cross section of the original SP image and the orange solid curve is the cross section of the deconvoluted SP image. Compared to the original SP signal, the deconvoluted signal is much smoother and the charge accumulation is more evident due to the enhanced signal intensity. In this deconvolution, since the features (the nanorod) are relatively small, emphasis is on the restoration of the accuracy of SP signals. To do so, the regularization parameter λ was chosen to be 100. This enforce the deconvoluted image to represent the maximum likelihood of the undistorted image while loosen the stress on the removal of noises.

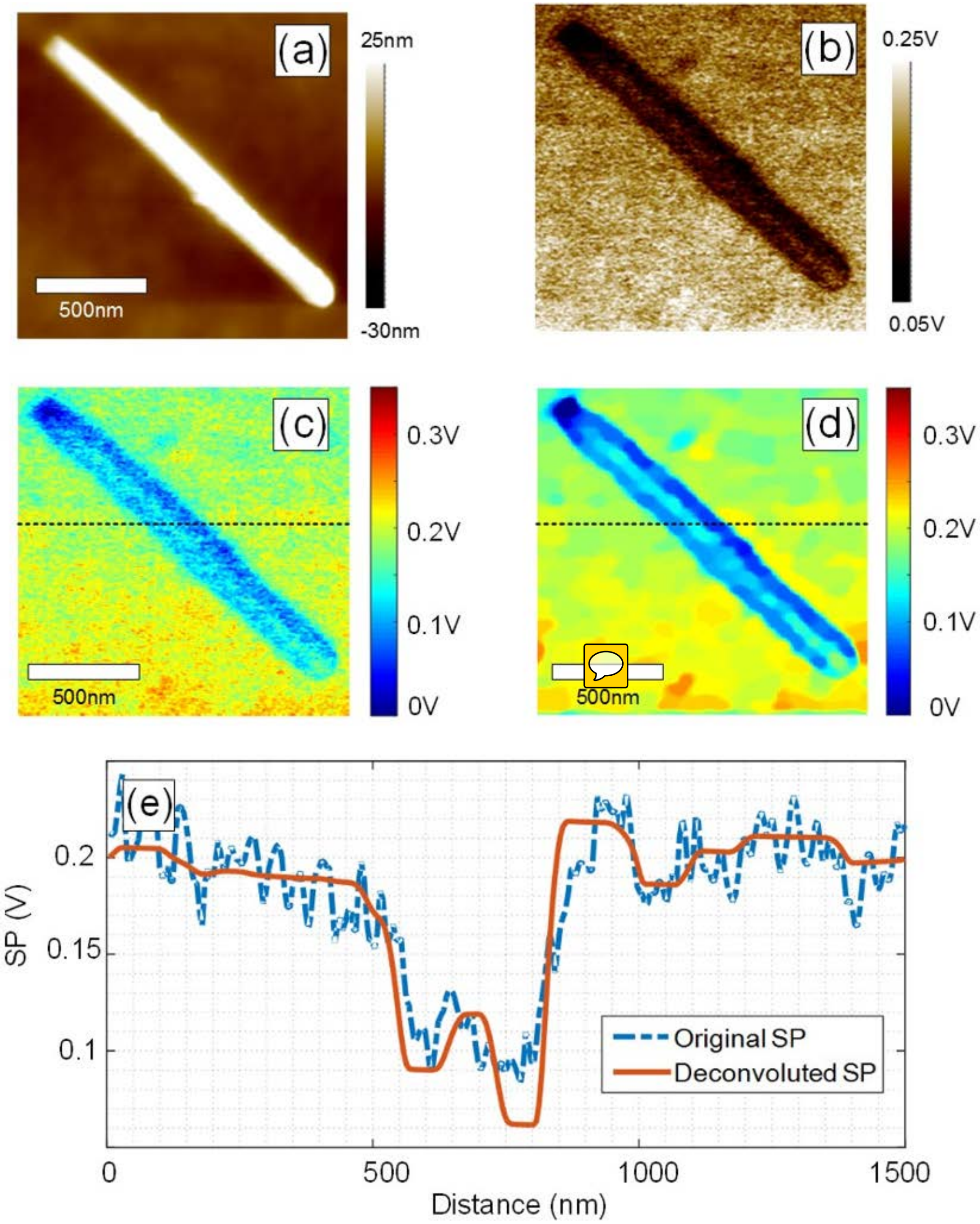

Figure 2.7. Deconvolution results of SP distribution of ZnO nanorod on P3HT/PCBM surface. (a) Topography of ZnO nanorod on P3HT/PCBM surface; (b) SP distribution of the ZnO nanorod; (c) Recreation of (b) in MATLAB; (d) Deconvoluted SP image of the ZnO nanorod; (e) Cross section signals of the original and the deconvoluted images: blue dashed curve is the cross section of the original SP image indicated by black dashed line drawn on (c) and orange solid curve is the cross section of the deconvoluted SP image indicated by black dashed line drawn on (d).

Next, the reconstruction algorithm was performed on a 2-D material graphene oxide, where the emphasis is on the removal of noises. Shown in Figure 2.8 are the measurement and deconvolution results of a graphene oxide flake on P3HT/PCBM blend. Figure 2.8 (a) is the topography image and Figure 2.8 (b) is its SP image. From the SP image, it can be observed that the whole image is buried in noise. For the purpose of a direct comparison with the deconvoluted image, SP image was recreated in MATLAB and is shown in Figure 2.8 (c). Deconvolution algorithm based on total variation regularization was again applied and the corresponding result is shown in Figure 2.8 (d). Compared with the raw image, the noise in deconvoluted image is greatly suppressed. This can also be observed from the cross-sectional signals shown in Figure 2.8 (e). Cross sections indicated by black dashed lines drawn on Figures 2.8 (c) and (d) are shown in Figure 2.8 (e), where the dashed blue curve is the cross section of the original SP image and the orange solid curve is the cross section of the deconvoluted SP image. Since the feature (the graphene oxide flake) in this measurement is relatively large compares with the resolution of KPFM, the value of the measured SP should maintain a relatively high fidelity as we discussed previously. Hence, the focus is on the removal of noises. To do so, the regularization parameter λ was chosen to be 10, much smaller than the value we had for the ZnO nanorod. As a result, SP image of the graphene oxide flake was significantly smoothed.

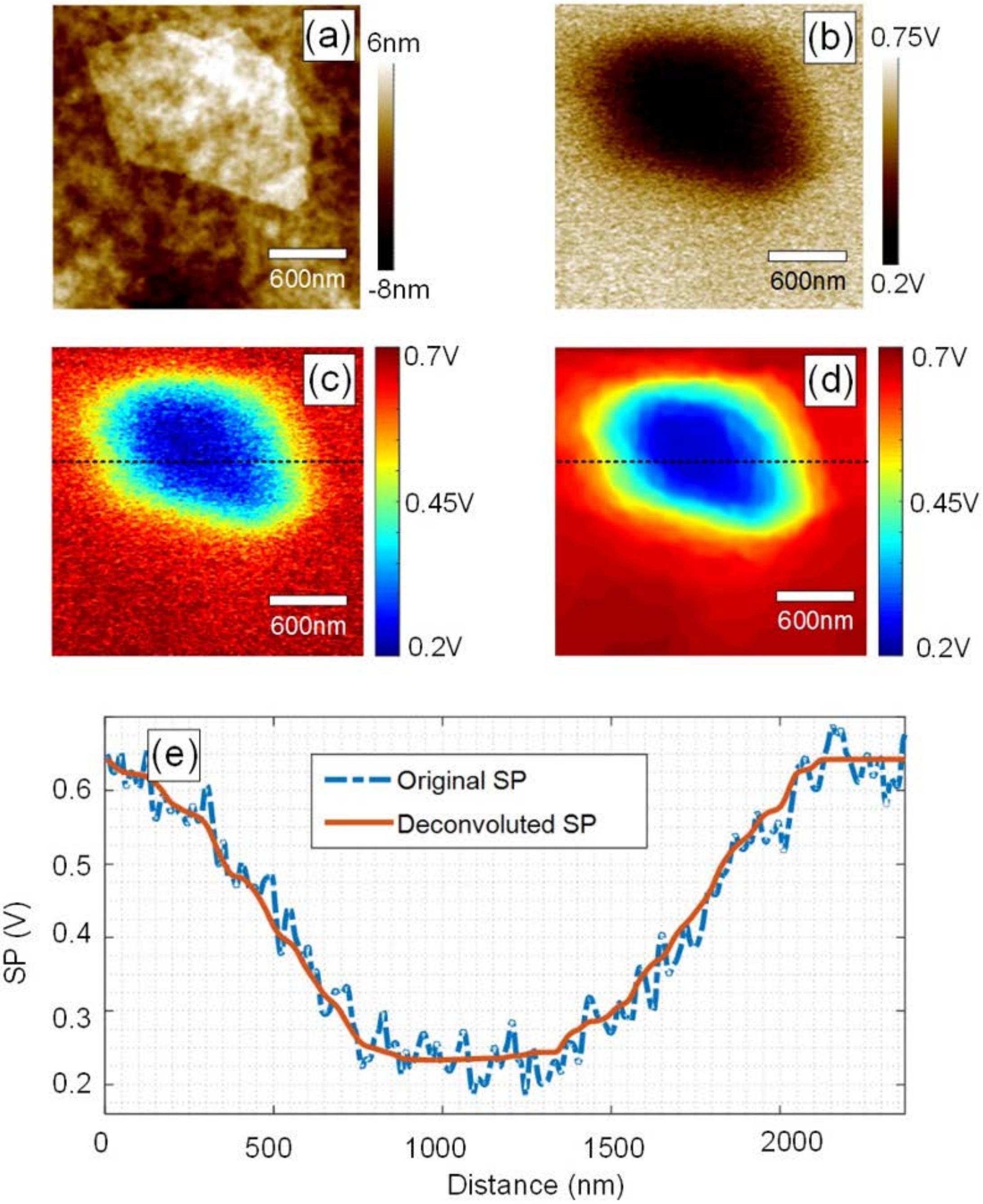

Figure 2.8. Deconvolution results of SP distribution of graphene oxide on P3HT/PCBM surface. (a) Topography of graphene oxide on P3HT/PCBM surface; (b) SP distribution of the graphene oxide flake; (c) Recreation of (b) in MATLAB; (d) Deconvoluted SP image of the graphene oxide flake; (e) Cross section signals of the original and deconvoluted images: blue dashed curve is the cross section of the original SP image indicated by black dashed line drawn on (c) and orange solid curve is the cross section of the deconvoluted SP image indicated by black dashed line drawn on (d).

2.4 SUMMARY

In this chapter, a novel way to experimentally calibrate the PSF of our KPFM system is demonstrated. This calibration method not only provides a more direct way to obtain the PSF than regular simulation approach, but also improves the accuracy of the PSF by taking into account the real probe shape. Moreover, a nonlinear reconstruction algorithm based on total variation regularization is applied to the deconvolution of KPFM signals. This iterative algorithm suppresses the noise and improves the resolution of KPFM measurement which greatly helps the interpretation of KPFM data.

3.0 CHARACTERIZATION OF CHARGE TRANSPORT BETWEEN SINGLE-WALLED CARBON NANOTUBE AND POLYMER

The application of KPFM is widely found in the characterization of semiconductor devices for the purpose of understanding their electrical properties. In this chapter, KPFM is utilized in the characterization of charge transport between SWNTs and polymers in organic solar cells. SWNTs are usually doped into organic solar cells to improve their carrier mobility, however, the charge transport mechanisms between SWNTs and polymers in organic solar cells are unclear and under debate. In this chapter, KPFM is utilized to address this controversial problem. By comparing the SP change of SWNTs on electron-enriched and hole-enriched sample surfaces respectively, it is concluded that electrons are blocked from SWNT while holes are favored to transfer to SWNT from the polymer. In addition, to proper explain the charge transfer behavior, a band alignment model of P3HT/SWNT heterojunction is proposed. Then, the charge transport behavior is further verified by hole mobility measurement of samples with and without the doping of SWNTs using space charge limited current (SCLC) method. SCLC results indicate that the existence of small amount of SWNT (wt. 0.5%) promotes device hole mobility to around 15-fold, indicating SWNT acts as hole transport channel.

3.1 BACKGROUND

Even though organic solar cells typically have lower efficiencies than their inorganic counterparts, they attract much attentions due to their low fabrication cost and high flexibility [26-28]. The cost to fabricate organic solar cells is potentially lower [29] because techniques such as roll to roll printing, simple brush and ink jet process can be incorporated into the fabrication process. While for inorganic ones, considering the structure and materials used, high vacuum and high energy are usually needed. Additionally, materials used in organic solar cells makes them highly flexible [30, 31]. Organic solar cells also have merits such as high optical absorption coefficient and the easiness to tune polymer molecules to obtained desired chemical and physical properties.

The first organic solar cell appeared in 1959 when Kallman and Pope fabricated a solar cell using anthracene single crystal which ended up with an open circuit voltage of 0.2 V and a power conversion efficiency (PCE) of $2 * 10^{-4}\%$ [32]. The first generation organic solar cells were fabricated by sandwiching a single layer of organic material in-between two metallic conductors which serve as electrodes [27]. Work function of the two metallic conductors were chosen to be different so that they create an electric field in the organic layer, which assists the exciton dissociation and also charge transportation in the cell. The defect of this structure is that the dissociation of excitons is inefficient and the resultant short circuit current and open circuit voltage are very low. The next breakthrough for organic solar cells was the invention of donor and acceptor bi-layer structure by Tang in 1986 [33]. Compare with the single layer structure, this bi-layer structure enhances exciton dissociation at donor-acceptor interface and extends the active region into both donor and acceptor domains. Also, the transport of charge carriers in the bi-layer structure is separated in donor and acceptor phases which greatly reduces the charge recombination. Moreover, the band gap between the two layers can be tuned so as to better match the solar spectrum. As a result, PCE of 1% was reported for such structure under AM2 illumination ($691\ \mathrm{W}/m^2$) [33]. However, this structure still suffers from a major issue—the low exciton dissociation efficiency. Usually, to achieve a good light absorption for a polymer, thickness of the polymer should be at least several tens of nanometers. This thickness is much larger than the exciton diffusion length of polymer which is typically 10 nm [34]. Because of this, most of the generated excitons will decay before they can find exciton dissociation interfaces. The problem of low exciton dissociation efficiency in organic solar cells was solved in 1995 with the introduction of bulk heterojunction (BHJ) structure. In BHJ, donor/acceptor materials were blended with each other creating numerous donor/acceptor interfaces for exciton dissociation [34]. Now, with optimizations, PCE of organic solar cell has been boosted to over 10% [35].

Generally speaking, the limitation of PCE in BHJ organic solar cells stems from the narrow absorption spectrum of polymer, the low dielectric constant of organic materials and the disordered BHJ structure in the active layer. To further improve the PCEs, new materials are incorporated into heterojunction structure so as to broaden absorption spectrum as well as enhance carrier mobility. SWNT, for instance, attracts much attention as a doping material for heterojunction organic solar cell due to its high carrier mobility [36]. Other benefits of the introduction of SWNT into organic solar cells include the potential to increase open circuit voltage and broaden the absorption spectrum of organic solar cells [37-39].

The incorporation of carbon nanotubes (CNTs) into photovoltaic devices with conjugated polymer was first reported by Kymakis and Amaratunga [40]. Since then this type of photovoltaic devices has received a tremendous amount of attention [41-43]. Organic solar cells based on polymer/CNTs composite were reported to possess high open-circuit voltage [37-39] which may reach up to 1.8 V [44]. However, these polymer/CNTs based photovoltaic devices usually showed limited efficiency compared with those based on polymer/fullerene bulk heterojunctions. One possible reason is that interfacial areas between polymer and CNT are insufficient for exciton dissociation considering the insolubility and low concentration of CNT in polymer (<1%) [45]. A more commonly adopted way to increase efficiency is using CNT as doping material for polymer/fullerene bulk heterojunction based solar cell [42, 46-48]. The introduction of CNTs into the polymer/fullerene bulk heterojunction improves the power conversion efficiency even without annealing, suggesting that the presence of CNTs either ameliorates the nanoscale morphology or improves the carrier mobility [49]. Experimental studies indicate that the performance of organic solar cells can be dramatically enhanced after introduction of proper amount of CNTs to active layer [46, 50, 51], while an excessive amount of CNTs, on the other hand, reduces the efficiency due to the increased bimolecular recombination as well as possible circuit shorting [46]. Thus, a proper ratio of CNT to polymer is critical for the improvement of PCE of CNT doped polymer solar cells.

Another issue that is critical in enhancing the performance of polymer based solar cells is balancing the carrier mobility considering the relatively low hole mobility in polymers. Thus, understanding the charge transfer mechanism at the polymer/CNT interface, that is, whether CNTs work as donor (transporting holes) or acceptor (transporting electrons), is of great interest to the research community.

Many studies concerning the interaction mechanism between CNT and polymer have been reported. Photoluminescence, for instance, has been used in characterizing CNT behavior in polymer blend. The photoluminescence quenching at the presence of CNT indicates that either charge transfer or energy transfer exists in such a blend [52, 53]. Study by Geng et al. showed photoluminescence of polymer quenched at the presence of CNT. Based on this observation, they concluded that the electron is transferred to CNT [52]. Nish et al., on the other hand, believe energy, instead of electron, in the form of exciton is transported to CNT [53]. They conducted photoluminescence excitation mapping to relate the initial absorption to final emission signal: while absorption is clearly caused by the polymer, the emission spectrum is closely related to electron transitions of CNT. Thus they believe energy is directly transferred to CNT.

A recent study by Stranks et al., using the femtosecond spectroscopic technique, has proven charge separation at the CNT/polymer interface (SWNT/P3HT) [54]. They observed that incorporating only small fractions (1%) of SWNTs allows photon-to-charge conversion with efficiencies comparable to those for conventional (60:40) P3HT-fullerene blends. However, their report also shows that excessive CNTs harm the charge separation.

Until now, the role of CNT as donor (transporting holes) or acceptor (transporting electron) is still controversial. The majority of research groups assume that CNTs work as acceptors [40, 47, 49] and as a result, the hot excited electrons will finally go to nanotubes and then be extracted by the external circuit. By examining all of the literature that support electron transfer, we found that their experimental results can also be well-explained by a hole transfer mechanism. Photoluminescence quenching observed by Geng et al. [52], for example, could be the result of hole transported to CNT. Also, Kymakis's observation of reduction in recombination when incorporating CNT which they explained by increased electron mobility could also be due to enhanced hole transport after incorporating CNT [47]. Additionally, one major problem that cannot be explained by assuming CNT as acceptor is the high open circuit voltage (close to or more than 1 V) observed in polymer/CNT solar cells [38, 39, 44]. If the CNT is assumed as an acceptor, the open circuit voltage should be much smaller as the open circuit voltage is linearly dependent on the band offset between the lowest unoccupied molecular orbital (LUMO) energy level of the CNT and the highest occupied molecular orbital (HOMO) energy level of the polymer, which should be less than a few hundred millivolts. The van Hove singularity of CNTs suggests that there exist wide band energy levels (E22) but carriers in these bands usually have a very short lifetime (less than 130 fs [55]) and quickly relax to the base band E11, where carriers have a longer lifetime (large than 30 ps [56]); thus van Hove singularity is unlikely the reason for the high open circuit voltage.

There are also groups that support CNTs as hole transporting channels in CNT/polymer blends [57, 58]. It is demonstrated by Chaudhary et al. that the incorporation of CNT improved hole mobility in the device but not electron mobility, which supports the hole transporting nature of CNT [51]. A recent finding by Dissanayake et al., in addition, experimentally proved that SWNT extracts holes but not electrons in the SWNT/P3HT blend [57]. They first fabricated devices based on metal/P3HT/ITO junctions, and by measuring photocurrent they found that the direction of photocurrent only depends on the difference between work function of metal and ITO. However, for devices of the same structure but with SWNT in contact with metal electrode, the direction of photocurrent is determined by P3HT/SWNT heterojunction despite the work function of metal used. Even when the work function of metal is lower than ITO (Al, for example), with the presence of SWNT, the current direction indicates that the hole is transferred to metal electrode. This is different from the observation of electron transferred to electrodes with lower work function in devices without SWNT and thus implies that SWNT behaves as effective hole extraction material.

Despite the experimental results above, no direct observations concerning the charge transfer mechanism between polymer and CNT is reported. To directly tackle the puzzle, KPFM is used to investigate the polymer/SWNT heterojunction. KPFM is able to differentiate work function of surfaces at nanoscale and is sufficient to directly observe the charge transfer at polymer/SWNT interface.

3.2 EXPERIMENTAL SETUP AND PROCEDURE

In this section, experimental setup and procedures are discussed. To observe the charge transport between SWNTs and polymer, SWNTs were deposited on the surface of P3HT:PCBM blend. The reason we choose P3HT:PCBM blend instead of P3HT is that the P3HT:PCBM blend will generate an apparent photovoltaic effect under illumination. Thus, electron-enriched surface as well as hole-enriched surface can be created with P3HT:PCBM blend using different buffer layers.

3.2.1 Experiment design

To generate electron-enriched and hole-enriched surfaces, solar cell devices with normal structure and inverted structure were fabricated respectively. Shown in Figure 3.1, Figure 3.1 (a) is the schematic and band structure of solar cells with regular structure and Figure 3.1 (b) is the schematic and band structure of solar cells with inverted structure. For cells with regular structure, after the generation of free charge carriers in the active layer (P3HT/PCBM), according to the band alignment, holes will be transported to PEDOT:PSS and electrons will be kept on the sample surface, this generates an electron-enriched surface. On the other hand, for cells with inverted structures, after the generation of free charge carriers in the active layer, electrons will be transported to ZnO thin film and the active layer will be a hole-enriched surface.

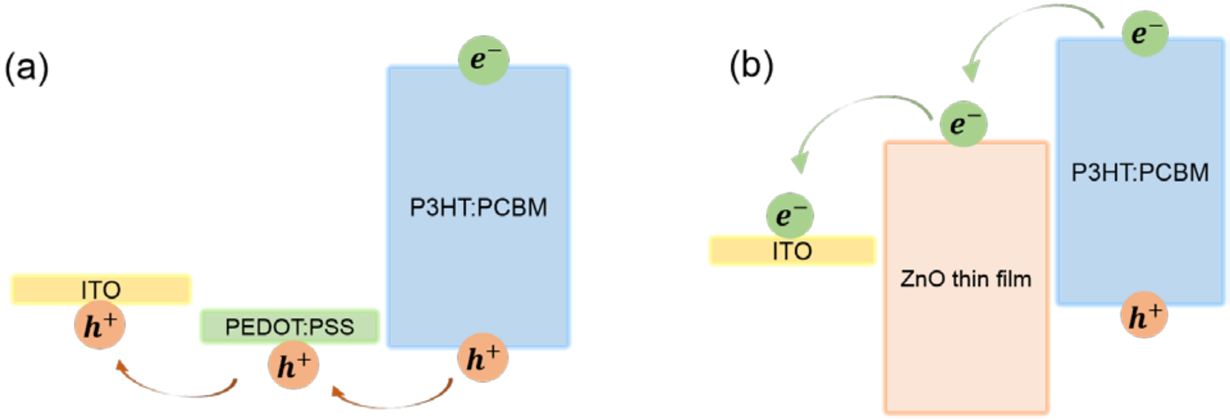

Figure 3.1. Schematic of solar cells. (a) Normal structure and (b) Inverted structure.

Next, to observe the charge transfer between polymer and SWNT, SWNTs are coated on the surface of the active layer. SWNT is dispersed in IPA by sonication before it is coated on the active layer. The coating of SWNT is completed by treating the devices in vacuum while annealing at a low temperature to help the evaporation of IPA solvent. After IPA is evaporated, SWNT is in good contact with the active layer, forming a P3HT/SWNT heterojunction.

Finally, samples were mounted onto KPFM with wiring shown in Figure 3.2. ITO was grounded to give a reference to KPFM system and also neutralize excessive charge carriers transferred to ITO electrode from the active layer. KPFM measurements were performed in dark and under illumination respectively. The whole measurement was completed in chamber filled with Argon gas to prevent samples from being oxidized. By comparing the SP change of sample surface as well as SWNT in dark and under illumination, charge transfer mechanism between SWNT and polymer was revealed.

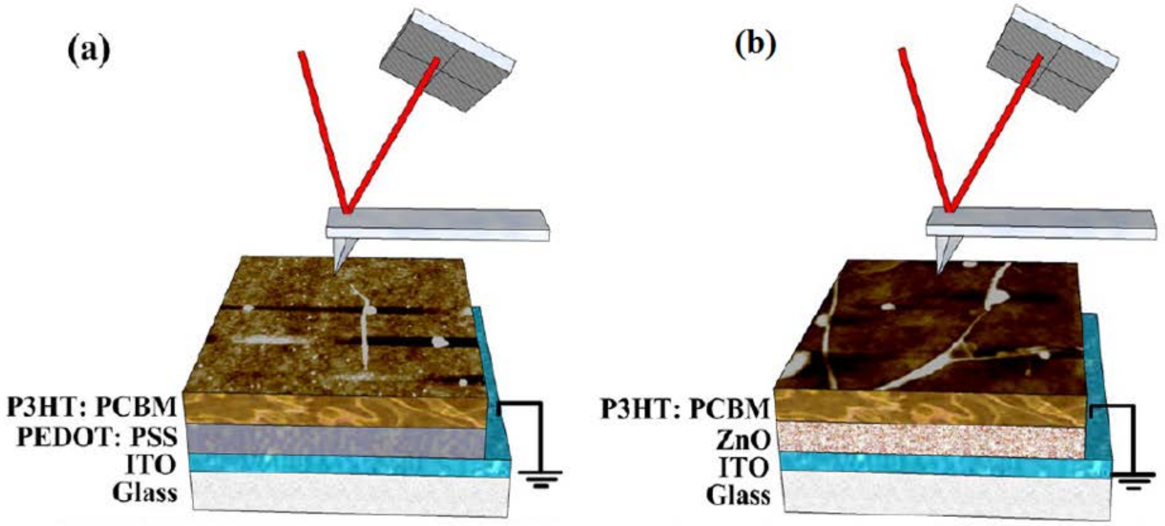

Figure 3.2. Experiment set up and device structure for KPFM study. (a) for normal structure and (b) for inverted structure.

3.2.2 Device fabrication procedures and parameters

To fabricate devices needed for KPFM study, firstly, ITO glasses were cleaned in Acetone, DI water, IPA respectively in ultra-sonication. For normal structure device, PEDOT:PSS in aqueous solution (as purchased from Sigma-Aldrich) was spin coated on ITO glass at a spin speed of 1500 rpm for 15 seconds following by 3500 rpm for 30 seconds to obtain a thin layer of several tens nanometers. After the coating of PEDOT:PSS thin film, the sample was annealed on hot plate in nitrogen atmosphere at 120 ℃ to get rid of excessive water. Concentration for P3HT:PCBM were chosen to be a typical value of 20mg/mL: 20mg/mL in Chlorobenzene solution. Filter was used to filter out large particles in P3HT:PCBM solution so as to get a smooth surface. Because the diameter of SWNT is less than 10 nm, smooth active layer is essential for us to locate and differentiate SWNT on the active layer. Spin coating was again used to coat a thin layer (around 100 nm) of P3HT:PCBM onto the previous substrate. Spin coat speed of 1500 rpm for 10 seconds following by 2500 rpm for 35 seconds were used this time. Then the substrate was annealed again at 120 ℃ for the evaporation of excessive Chlorobenzene. Finally, SWNTs dispersed in IPA were coated on the fabricated devices before being annealed at a low temperature in glove box in nitrogen environment.

Fabrication process for inverted structure was similar to that of normal structure except for the fabrication process for ZnO thin layer: ZnO thin film was deposited using 0.5M $Zn(AC)_2$ precursor and was followed by annealing in ambient condition for 30 min at temperature 350 ℃. (To avoid the unevenness of ZnO, sometimes, the coating procedure is repeated before annealing.) Next, active layer was deposited on ZnO thin film following the procedure and parameters described above, and finally, SWNT (dispersed in IPA) was deposited on the active layer.

3.3 RESULTS AND ANALYSES

In this section, KFPM measurements of the normal structure as well as the inverted structure are demonstrated and analyzed.

3.3.1 KPFM characterization of normal structure devices

Firstly, devices with a regular structure of ITO/PEDOT:PSS/P3HT:PCBM/SWNT was characterized on the sample surface. KPFM measurement was carried out in an argon environment protecting the sample from being oxidized. Figure 3.3 (a) illustrates the KPFM setup and device structure, Figure 3.4 (b) is the topography image of SWNT coated on P3HT:PCBM layer, and Figure 3 (c) and (d) are SP images of our device in dark and under illumination, respectively. The darkened SP image shown in Figure 3 (d) compare to Figure 3 (c) suggests that electrons were accumulating on P3HT:PCBM surface while holes were transported to the ITO electrode which was connected to the ground. This observation agrees with the fact that PEDOT:PSS layer blocks electrons but allows holes to transfer. Further, to examine the SP change in SWNT, we extracted and compared SP values of the cross section lines drawn on SP images acquired both in dark and under illumination. These SP values are shown in Figure 3.3 (e). Shown in Figure 3.3 (e), the blue solid curve is the cross section of SP image measured in dark and the red dashed curve is the cross section of SP image measured under illumination. It can be observed that while SP values of active layer decreased due to electron accumulation under illumination, SP values of SWNT stayed the same although SWNT was in an electron-enriched environment. This indicates that electrons transfer from P3HT to SWNT is blocked. This experiment with the same setup was repeated to confirm the fidelity of our conclusion, corresponding results are shown in Figure 3.4.

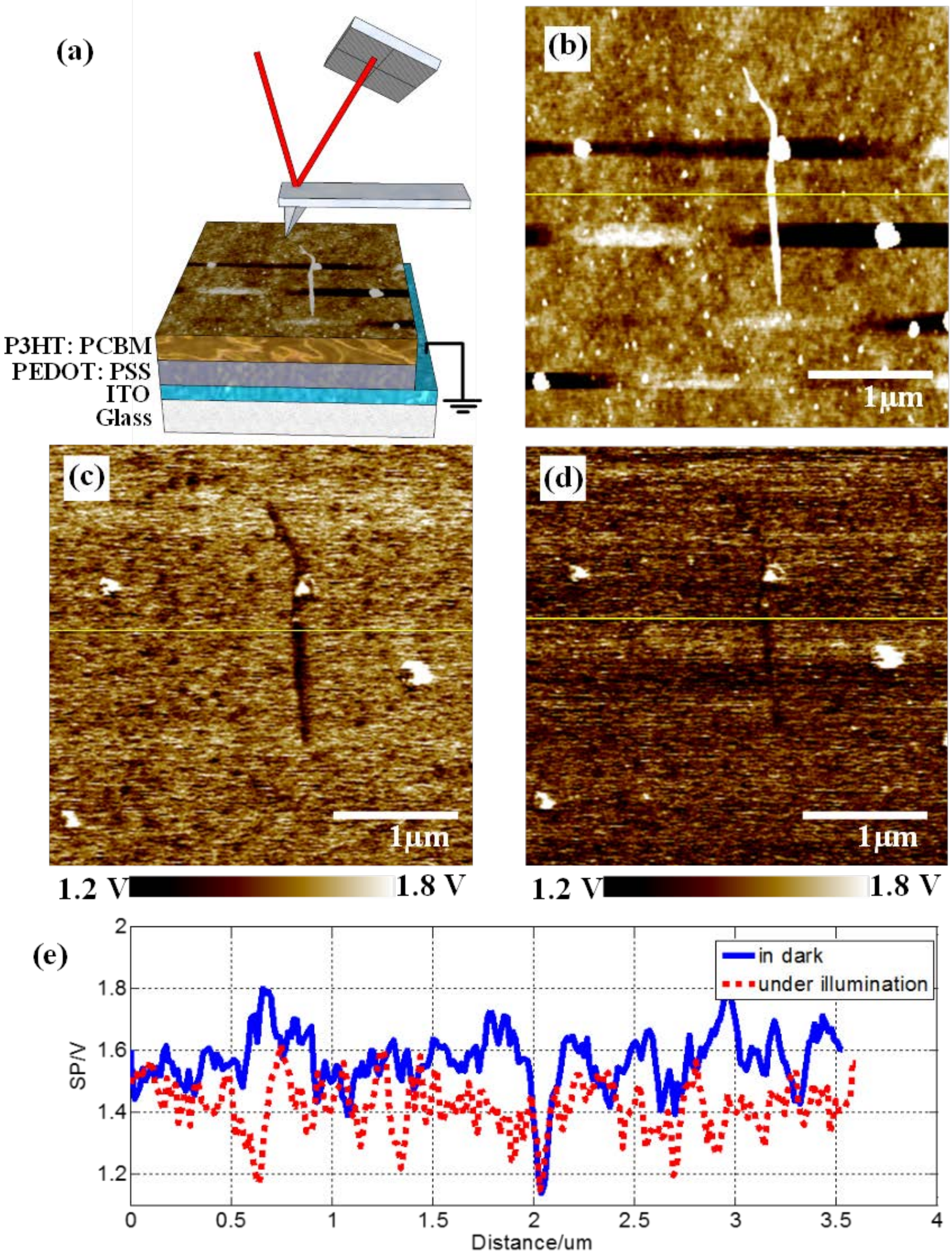

Figure 3.3. KPFM study of CNTs on top of P3HT:PCBM blend with a regular photovoltaic structure. (a) The illustration of device structure; (b) The topography image; (c) SP images in the dark; (d) SP image under illumination; (e) SP values of the cross section indicated by the yellow line in dark (blue solid curve) and under illumination (red dashed curve).

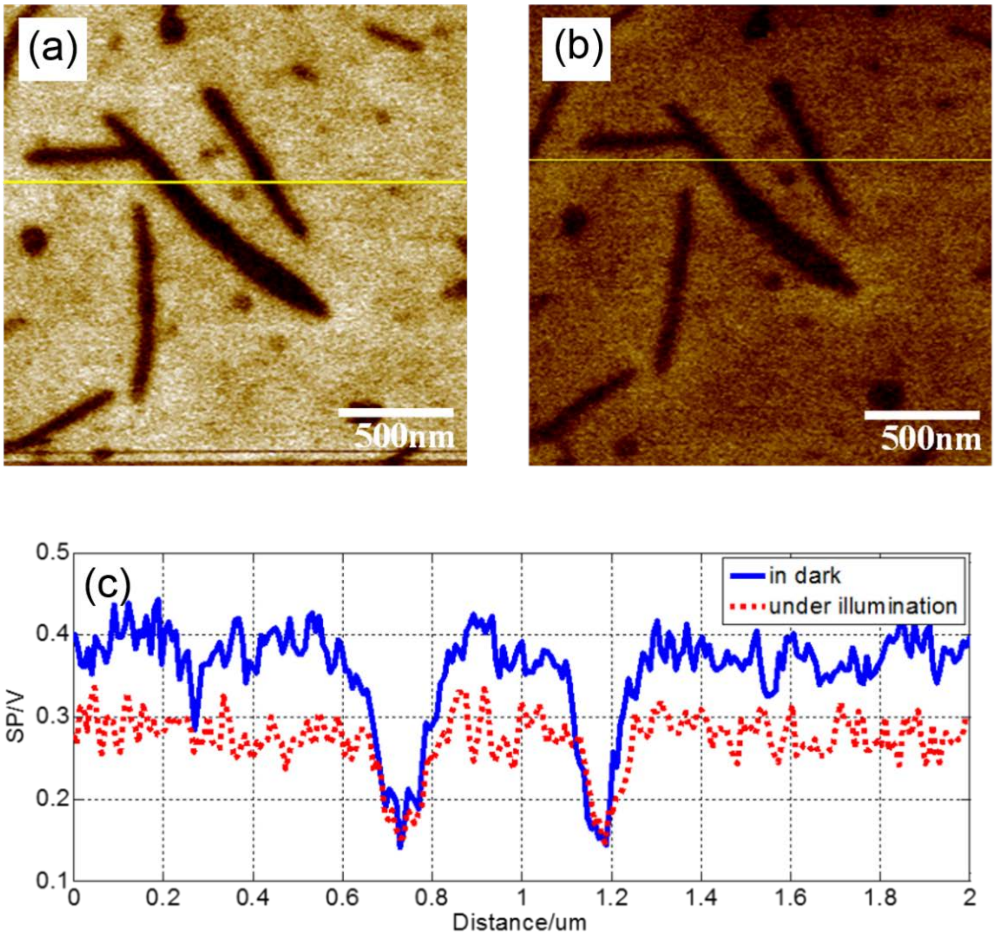

Figure 3.4. KPFM study of CNTs on top of P3HT:PCBM blend with a regular photovoltaic structure. (a) SP images in the dark; (b) SP image under illumination; (c) SP values of the cross section indicated by the yellow line in dark (blue solid curve) and under illumination (red dashed curve).

Shown in Figure 3.4, Figure 3.4 (a) is the SP image of the SWNTs on P3HT:PCBM blend measured in dark, and Figure 3.4 (b) is the SP image of the sample measured under illumination. Similar to our observation in Figure 3.3, when exposed to light, sample surface darkened due to the accumulation of electrons. The cross sections of the SP images were shown in Figure 3.4 (c), where the blue solid curve is the cross section of SP image measured in dark and the red dashed curve is the cross section of SP image measured under illumination. Similarly, although the SP signals of the sample surface decreased due to the accumulation of electrons, SP values of the

SWNTs stayed the same, indicating the transport of electrons from P3HT phase to SWNTs is blocked. This observation confirms that our experiment results are repeatable.

3.3.2 KPFM characterization of inverted structure devices

Next, devices with an inverted structure of ITO/ZnO/P3HT:PCBM/SWNT were characterized. SWNT dispersed in IPA was again coated on top of the P3HT:PCBM layer before drying in vacuum. Contrary to the electron blocking nature of PEDOT:PSS, ZnO is a hole blocking layer which allows the transporting of electrons while keeping the holes on the active layer. KPFM measurement was conducted in an argon environment in dark and under illumination, respectively. Figure 3.5 (a) shows the experiment setup and device structure. Figure 3.5 (b) presents the topography image of the sample, and Figure 3.5 (c) and (d) are SP images in dark and under illumination, respectively. Compare with Figure 3.5 (c), the brightened SP image in Figure 3.5 (d) indicates that holes were accumulating on P3HT:PCBM surface. This agrees with our understanding since ZnO is an electron conducting layer based on its band structure. To examine the change of SP value of SWNT in hole enriched environment, cross section lines were drawn on SP images obtained both in dark and under illumination. Corresponding results are illustrated in Figure 3.5 (e). In Figure 3.5 (e), the blue solid curve is the cross section of the SP image measured in dark and the red dashed curve is the cross section of the SP image measured under illumination. Contrary to the unchanged SP values of SWNT in electron enriched environment, SP values of SWNT in the hole enriched surface increased, indicating holes were transported to SWNT. Considering the band structures of P3HT and PCBM, we believe that holes are mostly likely transferred from P3HT to SWNT. Again, experiment with the same setup was repeated to ensure our conclusions are valid. The characterization results are shown in Figure 3.6.

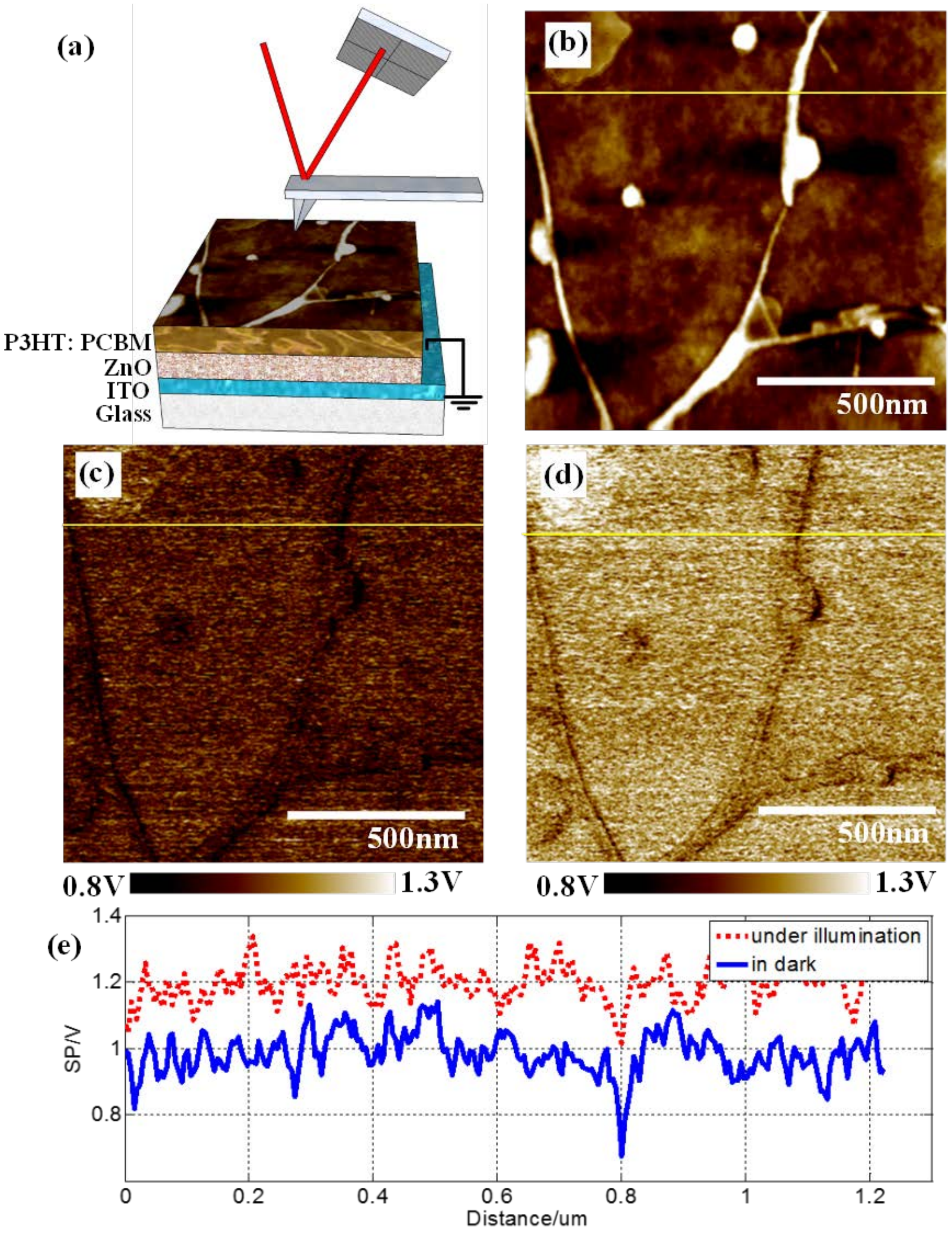

Figure 3.5. KPFM study of CNTs on top of P3HT:PCBM blend with an inverted photovoltaic structure. (a) The illustration of device structure; (b)The topography image; (c) SP images in the dark; (d) SP image under illumination; (e) SP values of the cross section indicated by the yellow line in dark (blue solid curve) and under illumination (red dashed curve).

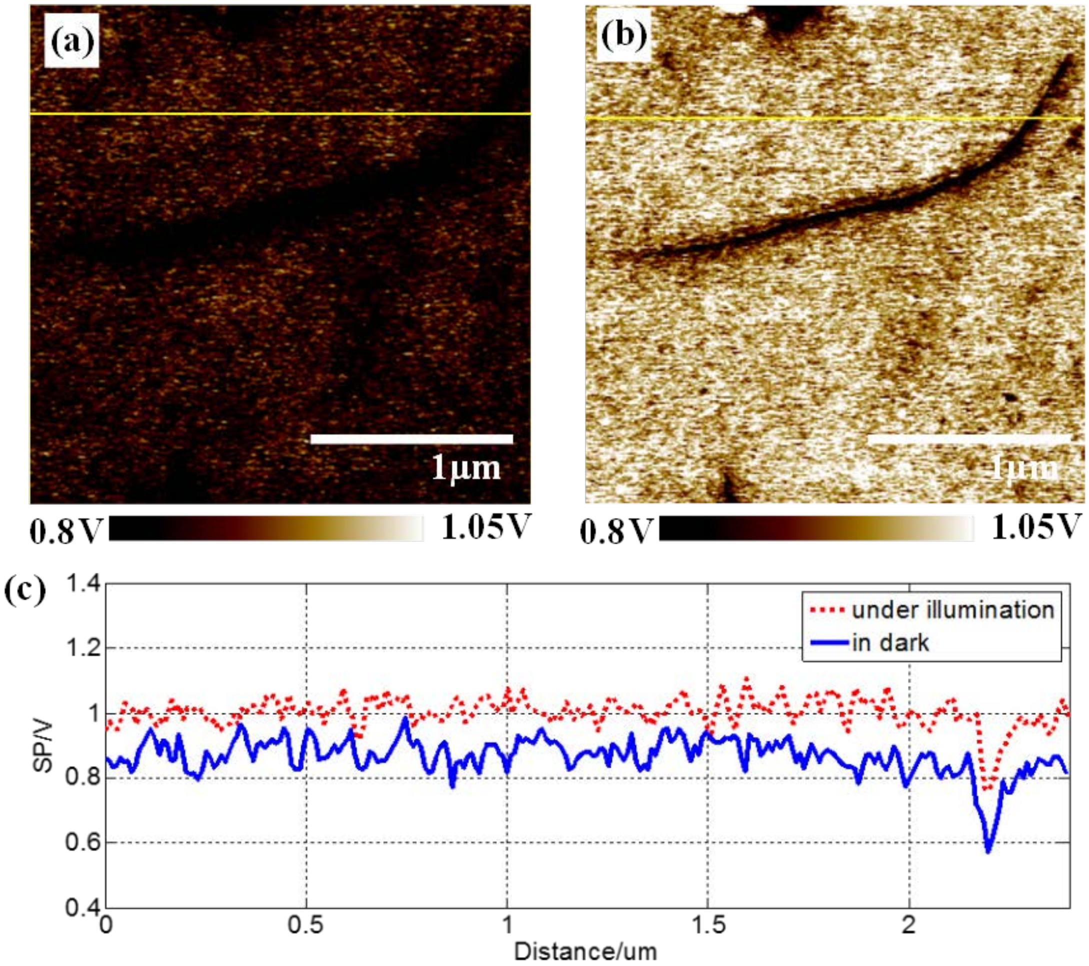

Figure 3.6. KPFM study of CNTs on top of P3HT:PCBM blend with an inverted photovoltaic structure. (a) SP images in the dark; (b) SP image under illumination; (c) SP values of the cross section indicated by the yellow line in dark (blue solid curve) and under illumination (red dashed curve).

Figure 3.6 (a) is the SP images of SWNTs on P3HT:PCBM blend with an inverted photovoltaic structure measured in dark, and Figure 3.6 (b) is the SP image measured under illumination. Compare with the SP value of the active layer in Figure 3.6 (a), the increased SP values in Figure 3.6 (b) indicates the accumulation of holes on sample surface. Similarly, cross sections indicated by the yellow solid lines drawn on Figure 3.6 (a) and (b) are shown in Figure 3.6 (c), where the solid blue curve is the SP signals measured in dark and the dashed red curve is the SP signals acquired under illumination. It can be observed from the cross section signals that

SP values of both SWNT and P3HT:PCBM surface increased when exposed to light. The increase of SP in active layer indicates that generated electrons were transported to ground while holes were kept on the sample surface, while the increase of SP of SWNT confirmed that holes can be transported from the polymer phase to SWNTs. This measurement indicates that our experiments are repeatable and conclusions are solid.

3.4 BAND ALIGNMENT MODEL

Based on KPFM measurement results shown in the previous section, band alignment model between SWNT and polymer is propose: the hole transfer at P3HT/SWNT interface can be explained by the band alignment of P3HT and SWNTs when they form heterojunctions. Due to the Fermi level alignment, bands of P3HT are bent up, and bands of SWNTs are bent down at their interface (shown in Figure 3.7 (a)). Because of such band bending, a potential barrier (Schottky barrier like) for electrons in the P3HT phase is formed, preventing the electrons transferring from P3HT phase to SWNTs. On the contrary, such band bending creates driving potential for hole transfer, and holes from dissociated excitons can thus be easily driven to SWNTs.

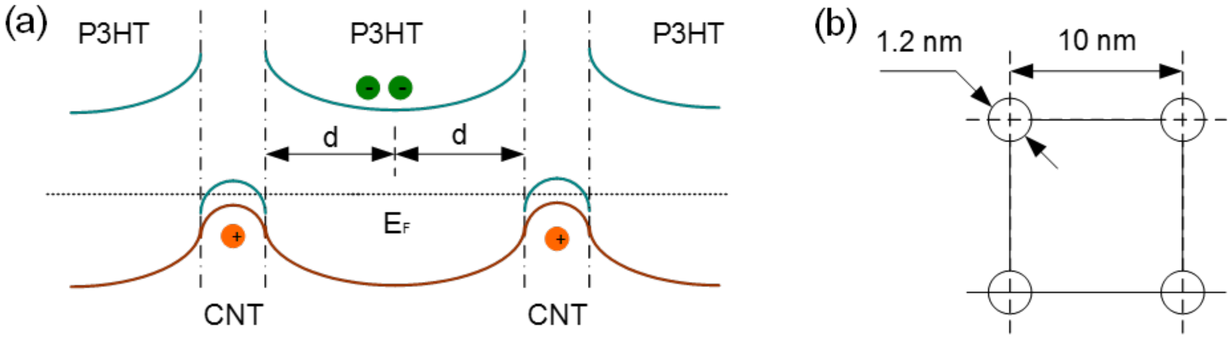

Figure 3.7. Band alignment model. (a) Band alignment of P3HT and SWNT blend; (b) Illustration for the volume ratio of SWNTs and P3HT.

This band alignment and charge transfer model also provides a good explanation to the high open-circuit voltage constantly observed in polymer/CNTs photovoltaic devices. According to this charge transfer model, the effective band gap between P3HT and CNT becomes the offset between the LUMO of P3HT (−3 eV) and the HOMO of CNT (−5 eV), which is about 2 eV, much larger than that of P3HT HOMO and CNT LUMO (only a few hundred millivolts). Because the open circuit voltage is linearly dependent on the effective band gap, the high open-circuit voltage reported in the literatures [37-39, 44] can be well-explained. On the other hand, electrons now need to be transported through polymer phase, which usually possess low electron mobility. Because of the imbalanced mobility, charge accumulation will occur, and thus most free electrons will be lost via recombination at surface states or midband states before being collected by the electrode. As a result, low efficiency is often observed in these devices.

This model also explains many phenomena for which existing theories cannot offer plausible explanations, for instance, energy transfer observed at the interface [59-61], and decreased performance after adding excessive CNTs [42, 46, 55]. According to this model, the space among CNTs has to be large enough to avoid the electrons in polymers tunneling into CNTs. Assuming the largest tunneling distance for the electron in P3HT is d = 5 nm (this value may need further evaluation by considering the exact band bending), the average distance among CNTs should be maintained at least 10 nm to avoid electron tunneling (shown in Figure 3.7 (b)). Considering the diameter of SWNTs is about 1.2 nm, the maximum volume ratio of CNTs to P3HT should be around 2.3% so as to avoid electron tunneling. The maximum weight ratio should be about 2.0% considering the mass density of SWNTs (1.0 g/cm^3) [62] and P3HT (1.1 g/cm^3) [63]. This prediction agrees with the experimental result of observing an optimal weight ratio of 3% for best device performance [64]. Apparently, excessive loading of CNTs will cause the free electrons to tunnel into the CNTs and results in quick bimolecular recombination with the holes inside CNTs. This can explain the observation of extremely short carrier lifetime (less than 10−100 ps) for excessive loading of CNTs but a very long carrier lifetime for loading of 1% only [54]. This can also explain why energy transfer instead of charge transfer is observed in many experiments [59, 65] with excessive loading of CNTs. Such a model also explains why the bimolecular recombination becomes dominant when excessive CNTs are added in the P3HT:PCBM blend in our previous study [46].

3.5 SPACE CHARGE LIMITED CURRENT (SCLC) MEASUREMENT

To verify that holes are transported from polymer phase to SWNT phase in SWNT doped organic solar cells, space charge limited current (SCLC) measurement was carried out to measure the hole mobility in devices with and without SWNTs. In SCLC region, the current in organic layers are dominated by the charge injections at the contacts. If the work functions of the contacts are chosen so that only one kind of charge carriers can be injected in to the device (hole-only device or electron-only device), carrier mobility of that type of carrier can be derived from J-V measurements. In this section, by carefully choosing the contact metals and buffer layers, hole-only devices are fabricated and hole mobility is measured using SCLC method.

3.5.1 SCLC measurement setup

Among the commonly used techniques to measure mobility, time-of-flight (TOF) is the most accurate one by far. However, to perform TOF, samples required are usually several micro meters thick which would be a waste of material, in addition, the setup of the measurement is complicated. On the other hand, SCLC is much more flexible in the requirement of film thickness. Also, experimental set up in SCLC is much simpler compared with that of TOF: to conduct SCLC measurement, instrument we need is a source meter which can detects the carrier density with applied voltage.

In order to specifically measure the hole mobility, injection of electrons into device is suppressed by carefully choosing electrodes with proper work functions. A hole-only device structure as ITO/PEDOT:PSS/P3HT-(SWNT)/Ag is adopted in our measurement (shown in Figure 3.8), in which the hole is injected into device from the ITO electrode.

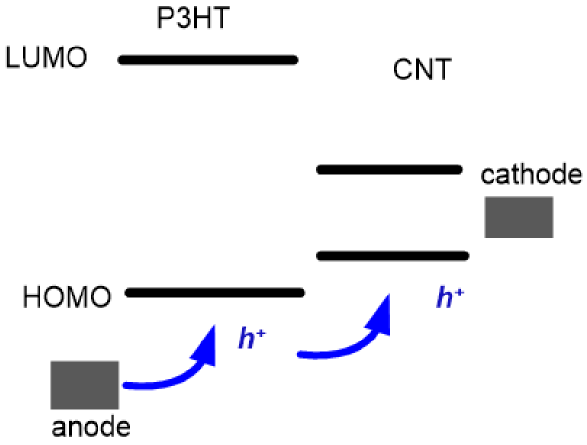

Figure 3.8. Schematic of hole-only device.

The work function of ITO/PEDOT:PSS is close to the HOMO of P3HT, forming an Ohmic contact [66] that ensures the effective hole transport in this device. On the other hand, the work function of Ag (4.7 eV) mismatches the LUMO of P3HT (3 eV), building up an electron injection barrier of about 1.7 eV which effectively suppresses electron injection into our hole-only device. In devices with SWNT, the weight ratio of SWNT with respect to P3HT is chosen to be 0.5% so as to avoid electron tunneling (based on our previous analysis). SWNT is dispersed in chlorobenzene (CB) by sonication. We find out that a negligible amount of P3HT helps dispersion of SWNT in CB. When SWNT with a concentration of 1 mg/mL is dispersed in CB by sonication for several hours, after leaving this solution standing overnight, SWNT solution with negligible P3HT is transparent without observable bundle or sediment while SWNT solution without P3HT has noticeable sediment. Hole mobility is measured before and after device annealing with an annealing temperature of 120 °C with an interval of 10 min. After correcting applied voltage for built-in voltage V_{bi} and voltage drop across series resistance V_{Rs}, hole mobility is calculated from current density J and effective voltage across polymer layer following equation [67]:

$$J = \frac{9}{8}\varepsilon_r\varepsilon_0\mu_{h0}e^{0.891\beta\sqrt{E}}\frac{V^2}{d^3} \tag{3.1}$$

where V is the effective voltage, μ_{h0} is the zero field hole mobility, and d is the active layer thickness.

Thickness of P3HT layer is measured by AFM tapping mode: after P3HT layer is coated, CB is used to wash away part of the P3HT layer. AFM is then utilized to measure the height difference between surface with P3HT layer and without P3HT layer. The difference at the boundary represents the layer thickness. Figure 3.9 (a) is AFM topography image taken just at the boundary and Figure 3.9 (b) is a cross section of the topography. A peak is observed at the boundary due to the damage of P3HT layer by CB solution. To avoid the error caused by the peak, we put markers at the very edge of the peak. From markers placed on the cross section, we obtain the thickness of P3HT layer after tilt correction. The thickness of P3HT layer is calculated to be 125nm.

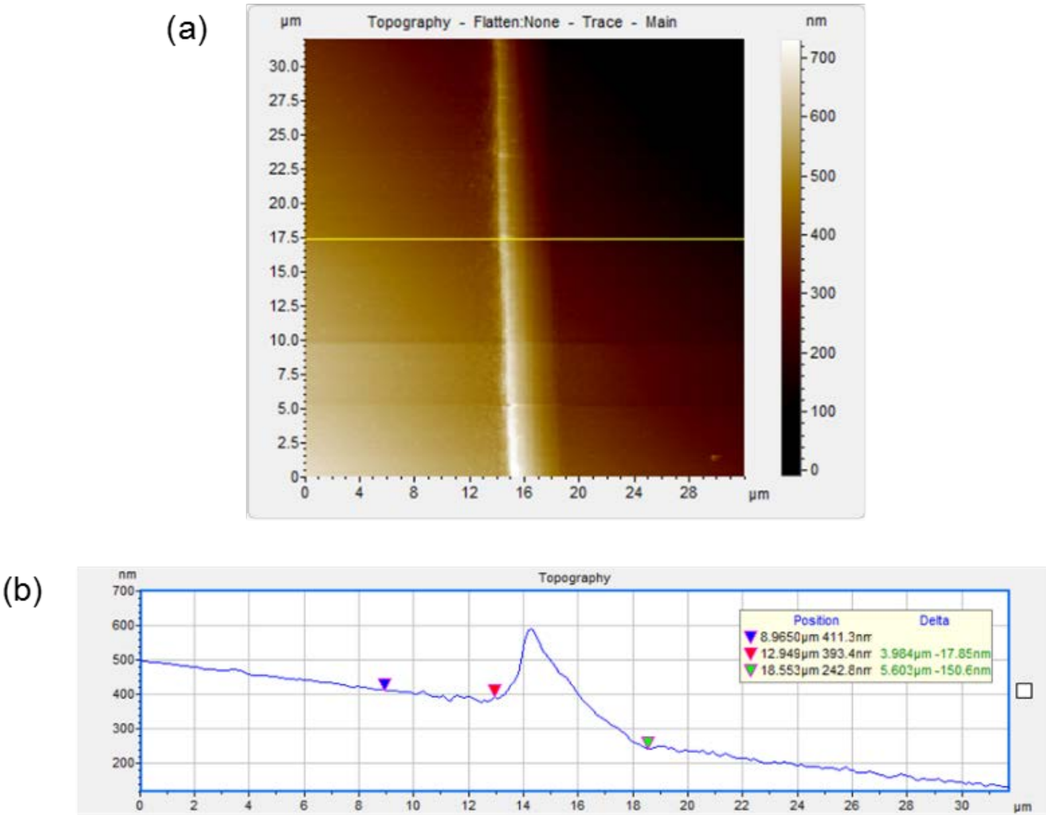

Figure 3.9. P3HT layer thickness measurement. (a) AFM topography image of the boundary; (b) Cross section of the topography image indicated by the yellow line.

3.5.2 SCLC measurement results

We repeated our SCLC measurement more than 5 times for a single temperature and for conditions with and without the doping of SWNT. Measurement data (average) of hole mobility is recorded in Table 3-1 and plotted in Figure 3.10.

Table 3-1 Hole Mobility Measurement Result of Devices with and without SWNT

Anneal time (min)	Hole mobility w/ SWNT (cm^2V^{-1}/S^{-1})	Hole mobility w/o SWNT (cm^2V^{-1}/S^{-1})
0	3.34×10^{-4}	2.25×10^{-5}
10	1.90×10^{-3}	2.63×10^{-4}
20	2.10×10^{-3}	3.01×10^{-4}
30	2.10×10^{-3}	4.82×10^{-4}

From the above table, it is concluded that without annealing, the hole mobility of samples with SWNT is about 15 fold larger than ones without SWNT, suggesting that hole mobility is increased at the presence of SWNT. This confirms our conclusion of SWNT acting as hole transporting channel in P3HT/SWNT heterojunctions. Moreover, after annealing, the difference between hole mobility of samples with and without SWNT decreased to around 4 fold. This is due to the ameliorated nanoscale morphology of P3HT which results in a significant enhancement in hole mobility (more than 20 fold larger) compared with ones without annealing.

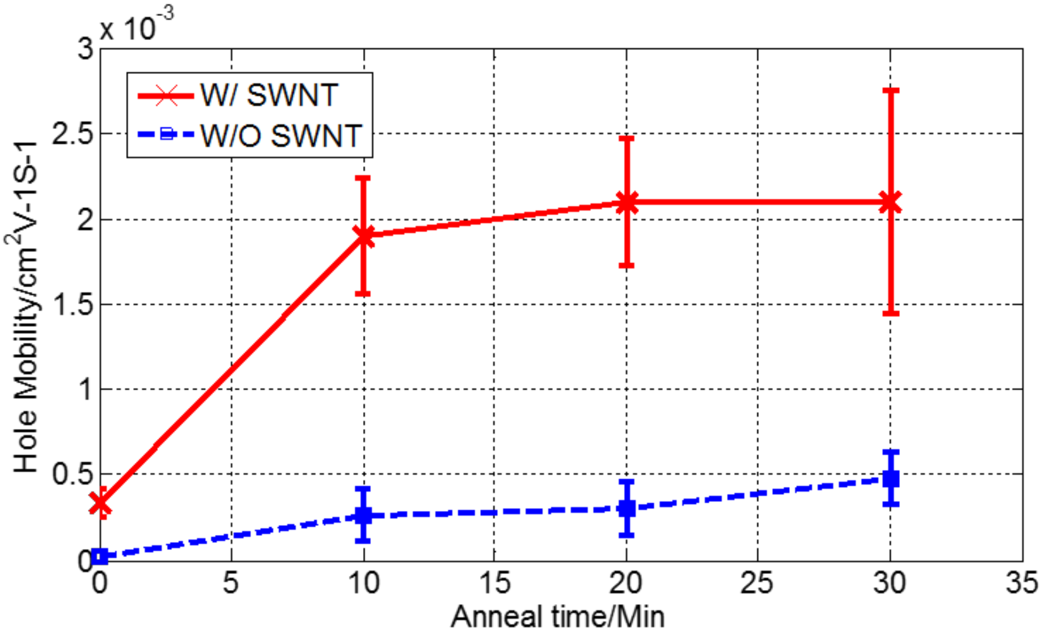

Figure 3.10. Hole mobility measurement results of devices with (red solid line) and without (blue dashed line) SWNT at different annealing times.

3.6 SUMMARY

To summarize, this chapter demonstrates the application of KPFM in the characterization of charge transport mechanisms between SWNT and polymer in organic solar cells. We proved that SWNTs act as hole transporting channel in P3HT/SWNT heterojunction by directly observing the SP change of SWNTs in electron-enriched and hole-enriched environment. We noticed that, when SWNT is in an electron-enriched environment, the SP value of SWNT stays the same while it increases when SWNT is in hole-enriched environment. This observation indicates that electrons are blocked from SWNT but holes can be transferred to SWNT.

Our band alignment model of P3HT/SWNT heterojunction provides a good explanation for our observation: when bands of P3HT and SWNT align with each other after the formation of

P3HT/SWNT heterojunction, a potential barrier is formed in P3HT phase which prevent electrons from entering SWNT but drive holes to SWNT. Our presented model can also explain many other observed phenomena in the literatures, such as high open-circuit voltage, requirement of low concentration of CNTs in the device, and energy transfer under high concentration of CNTs, which cannot be well explained before. Further, by directly measuring the hole mobility of samples with and without SWNT, we again verified the hole transporting behavior of SWNT.

We believe that proving the hole transporting behavior of SWNT is significant in enhancing the performance of organic solar cells by CNTs. Considering the imbalanced carrier mobility in polymer/fullerene bulk heterojunction based solar cell, the doping of SWNT will greatly reduce the imbalance by improving hole mobility and finally will be promising for the improvement of efficiencies of such solar cells.

4.0 REVEALING THE WORKING MECHANISMS OF PLANAR PEROVSKITE SOLAR CELLS WITH CROSS-SECTIONAL SURFACE POTENTIAL PROFILING

This chapter is another application of KPFM in the characterization of solar cells. In this chapter, KPFM is utilized in the characterization of the cross-sectional surface of perovskite solar cells. Devices with regular structure ITO/ZnO/perovskite/spiro-OMeTAD/Au and inverted structure FTO/NiO_x/perovskite/ZnO/Ag were studied. The analysis of KPFM measurement indicates that, while p-n junction forms at perovskite/ZnO interface in regular planar perovskite solar cells, p-i-n junction exists in inverted planar perovskite solar cells with electric field peaks at perovskite/NiO_x and perovskite/ZnO interfaces. In addition, charge injection barriers in planar perovskite solar cells were revealed with relative SP profiles obtained under different biases. In regular perovskite solar cells, the drop of bias voltages was observed only at perovskite/ZnO interface, indicating that charge injection between perovskite and ZnO is inefficient but the contact between perovskite and spiro-OMeTAD is an ideal ohmic contact. While in inverted perovskite solar cells, voltage drop was observed at both perovskite/NiO_x and perovskite/ZnO interfaces, suggesting the existence of charge injection barriers at both contacts. The appearance of charge injection barriers at both perovskite/NiO_x and perovskite/ZnO contacts exacerbates the charge recombination in inverted perovskite solar cells which leads to their relatively low open circuit voltages. Our results indicate that the inefficient charge extraction is a major problem affecting the performance of planar perovskite solar cells.

4.1 BACKGROUND

The newly emerging organic-inorganic hybrid lead halide perovskite solar cell has attracted much attention due to its potential to reach high PCE with low manufactural cost [68-70]. Perovskite solar cells utilize earth abundant materials and low-cost solution based processing techniques which greatly reduce their manufacturing expense [71]. In addition, the potential of perovskite solar cells has been demonstrated by their rapid improvement on PCEs which exceeded 20% within a few years [72]. The typical device structure of a perovskite solar cell consists of a light absorption layer organometal halide ($\mathrm{CH_3NH_3PbX_3}, \mathrm{X} = \mathrm{Cl}, \mathrm{Br}$ or I) sandwiched in between two buffer layers [73]. A mesoporous metal-oxide scaffold (TiO_2) was initially used as a porous substrate to support the growth of light absorbing layer while conducting electrons [74]. However, the fabrication of such mesoporous scaffold usually requires a temperature as high as 500 ℃ which renders it incompatible with flexible substrates [75]. Later, to simplify manufacturing process and reduce manufacturing cost, researchers came up with planar cell structures which replace the mesoporous metal-oxide scaffold with compact electron conducting layer (ZnO thin film, for instance), such thin film perovskite solar cells allow low-temperature process and greatly simplify the fabrication process [70]. Attentions have also been paid to the lifetime of perovskite solar cells. Usually, an organic layer, 2,2′,7,-7′-tetrakis(N,N-di-p-methoxyphenylamine)-9,9′-spirobifluorene (Spiro-OMeTAD), is used as hole transporting layer (HTL) in regular perovskite solar cells due to the good match of its HOMO level to that of perovskite layer. However, spiro-OMeTAD quickly degrades when exposed to ambient conditions (moisture and heat). To tackle the degradation problem, the most straightforward method is to replace the organic spiro-OMeTAD layer with more stable HTLs. One group of materials that have been intensively studied for this replacement is the p-type inorganic semiconductors. Since inorganic buffer layers have been widely used and intensively studied in organic solar cells [76-78], they can be readily adapted to perovskite solar cells. In the work by You *et al.*, with the inorganic p-type semiconductor Nickel oxide (NiO_x) substituting Spiro-OMeTAD as the HTL, they fabricated perovskite solar cells with an inverted structure of ITO/NiO_x/perovskite/ZnO/Al. After testing the device in air at room temperature for 60 days, they claimed that this inverted structure has an improved stability against water and oxygen degradation [79].

While we witness the rapid increase of PCE and great improvement on the stability of perovskite solar cells, understanding their working mechanism becomes more and more critical for their further development. It is now clear that free charge carriers are generated in perovskite layer upon light absorption because thermal energy is sufficient to overcome the excitons binding energy in these cells [80]. However, questions such as how do the free charge carriers transport to their respective electrodes and what are the junction structures inside perovskite solar cells are still unclear and under debate [81-83]. Jiang et al., for instance, studied the electric field inside regular perovskite solar cells with a structure of TCO/TiO_2/perovskite/Spiro-OMeTAD/Ag in their work [81]. They reported that a p-n junction formed at the interface between TiO_2 layer and perovskite layer while no junction was observed at Spiro-OMeTAD/perovskite interface. On the other hand, Bergmann et al. reported that by comparing KPFM measurement performed on perovskite solar cells with a regular structure in dark and under illumination, they found that electrical potential barrier was also present at Spiro-OMeTAD/perovskite interface, and that the junction structure inside the cell is p-i-n [82].

In this chapter, to clarify the working mechanisms of both regular and inverted planar perovskite solar cells and more importantly, to identify the defects that undermine the performance of inverted planar perovskite solar cells, KPFM was employed to map the SP distribution on the cross-sectional surfaces of both types of solar cells. With the obtained SP distribution of the cross-sectional surfaces, we are able to identify the junction structures located inside the cells, also, charge injection barriers that undermine the performance of perovskite solar cells are revealed.

4.2 DEVICE FABRICATION

For regular perovskite solar cells with a structure of ITO/ZnO/perovskite/Spiro-MeOTAD/Au, methylammonium iodide (MAI) was synthesized as previously reported by our group [84]. lead(II) iodide (PbI_2) of 99.999% purity was purchased from Sigma-Aldrich and used as received. ZnO particles were synthesized as previously reported [85], and was dissolved in solution of methanol, chloroform and n-butanol with volume ration 1:1:14. The resultant ZnO nanoparticle solution has a concentration of 5 mg/ml. ZnO nanoparticle solution was then spin coated on patterned ITO substrate with a speed of 2000 rpm for 30 S. The spin coating was repeated twice to obtain a continuous film. The obtained ZnO thin film was annealed on hot plate at 200℃ for 30 min to remove solvent and improve film quality. For the fabrication of perovskite layer, methylammonium iodide (80mg), PbI_2 (506mg) was dissolved in dimethyl sulfoxide (39 µl) and N,N-Dimethylformamide (318 µl) by stirring for an hour in room temperature. The resultant solution was deposited by spin coating at a speed of 4000 rpm for 22 S. Diethyl ether was used to remove solvent N,N-Dimethylformamide during the spin coating process. The sample was followed by annealing at a temperature of 100 ℃ on hotplate for 12 min. The resultant perovskite thin film has a thickness around 350 nm. Spiro-OMeTAD (80 mg), 4-tert-butylpyridine (28.5 µl) and bis(trifluoromethanesulfonyl)imide (Li-TFSI) (from 520 mg Li-TFSI in 1 ml acetonitrile) (17.5 µl) were dissolved in 1ml chlorobenzene by stirring for 10 min. The resultant solution was deposited by spin coating at 4000 rpm for 30 S. Finally, Au was deposited through a shadow mask with a size of 3×4 mm^2 with E-beam evaporation.

For inverted cells with a structure of FTO/NiO_x/perovskite/ZnO/Ag, NiO_x sol-gel was synthesized by dissolving 746.52 mg nickel acetate tetrahydrate and 29.94 mg copper acetate monohydrate in 0.1 ml hydrochloric acid and 10 ml 2-methoxyethanol. The resultant solution was stirred at 400 rpm for 1h in 60 ℃ water bath. The as obtained solution was deposited on patterned FTO by spin coating at a speed of 3000 rpm for 30 S. The coating was repeated twice for a continuous film. The obtained thin film was annealed on hotplate at 450 ℃ for 1h. Then perovskite layer was spin coated with the same method as we previously mentioned. ZnO nanoparticles were deposited by spin coating at a speed of 2000 rpm for 30 S. Finally, Ag was deposited by e-beam evaporator through the same shadow mask.

4.3 CHARACTERIZATION OF CROSS SECTIONAL SURFACE OF PEROVSKITE SOLAR CELLS

4.3.1 Experiment setup

In the characterization of cross-sectional surfaces of solar cells, one of the most commonly used techniques is to bias the solar cell with different DC voltages [86, 87]. As pointed out by Chen *et al.*, SP distribution within a cell under illumination in an open-circuit condition is equivalent to the SP distribution within the cell when it is measured in dark while being forward biased at its open circuit voltage [87]. This indicates that, by biasing a solar cell with different voltages in dark, we can study the SP distribution of the cell at its operating condition. In this work, a single-path scan KFPM, Agilent SPM 5500, was used in the characterization of planar perovskite solar cells. All KPFM measurements were carried out in dark ambient condition with different DC biases provide by a power supply. Shown in Figure 4.1 is the experimental set up and the working principle of KPFM working in amplitude modulation mode. Cathodes of planar perovskite solar cells were connected to the common ground of KPFM and power supply while various DC bias voltages were applied to the anodes of perovskite solar cells. In operation, KPFM system records the DC voltages biased to its conductive probe at the point when the electrostatic force between probe and sample is nullified at the electrical frequency. The corresponding DC values can then be further processed to acquire SP distribution of the sample [16].

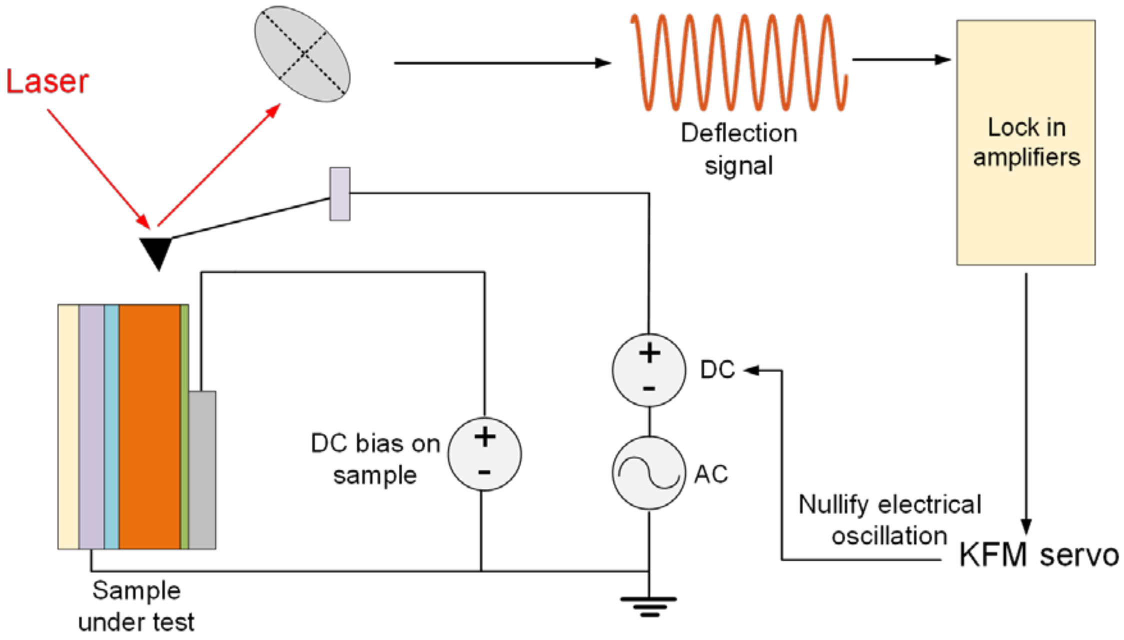

Figure 4.1. Experimental set up and working principle of KPFM in amplitude modulation mode.

4.3.2 Characterization result and analysis

Planar perovskite solar cells with regular and inverted structures were fabricated for this study. The regular perovskite cell has a structure of ITO/ZnO/perovskite/Spiro-OMeTAD/Au, and the inverted perovskite solar cell has a structure of FTO/NiO_x/perovskite/ZnO/Ag. In the fabrication of inverted perovskite solar cells, we used FTO as the substrate instead of ITO. The reason for this is that, in the preparation of inverted perovskite solar cells, annealing temperature of higher than 300 ℃ was needed for a high quality NiO_x thin film. Such high temperature causes the increase of ITO impedance which not only degrades the performance of perovskite solar cells but also leads to the drop of extra potential across ITO layer, making it difficult to interpret SP profiles correctly. The efficiencies of the fabricated cells were measured under one sun conditions (100 mW cm^2, AM 1.5G). Two perfectly working cells were chosen for the cross-sectional characterization and their I-V curves are shown in Figure 4.2.

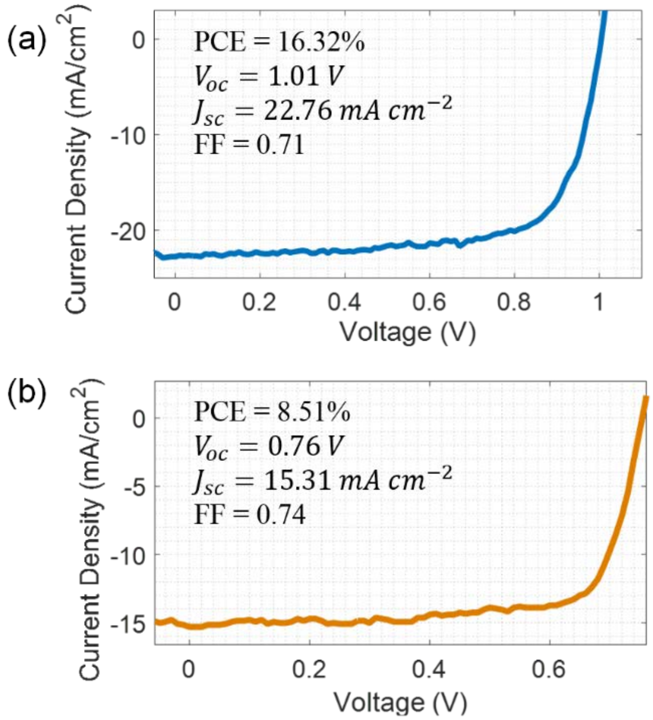

Figure 4.2. I-V curves of perovskite cells under test. (a) I-V curve of the regular perovskite cell under test; (b) I-V curve of the inverted perovskite cell under test.

Figure 4.2 (a) is the I-V curve of the regular perovskite solar cell used in the cross-sectional measurement. With an open circuit voltage of 1.01 V, a short circuit current of 22.76 mA/cm^2 and a fill factor (FF) of 0.71, the regular perovskite cell has a PCE of 16.32%. Figure 4.2 (b) is the I-V curve of the inverted perovskite cell used in the measurement. This cell has an open circuit voltage of 0.76 V, a short circuit current of 15.31 mA/cm^2 and a FF of 0.74, leading to an efficiency of 8.51%. From the I-V curves, it is safe to conclude that both cells have decent efficiencies to ensure our KPFM characterizations were conducted on working devices and the measurement results reflect typical working mechanisms of both types of cells. Comparing the efficiencies of the two cells, the performance of the inverted one is not as good as the one with normal structure. The lower efficiency mainly resulted from the lower open circuit voltage and lower short circuit current. Usually, the open circuit voltage of a perovskite solar cell is determined by the bandgap of the active layer and the HOMO level of the HTL [88]. But even with the same active layer ($CH_3NH_3PbI_3$) and similar HOMO levels [79, 89], regular and inverted planar perovskite solar cells demonstrated large differences in their open circuit voltages. Statistical data on the distribution of open circuit voltages for regular and inverted perovskite solar cells were collected from 96 regular perovskite solar cells and 135 inverted perovskite solar cells, corresponding results are shown in Figure 4.3. Figure 4.3 (a) and 3 (b) are the histograms of the open circuit voltages and PCEs of regular perovskite solar cells while Figure 4.3 (c) and (d) are the histograms of the open circuit voltages and PCEs of inverted perovskite solar cells. Shown in Figure 4.3 (a), over 90% percent of the regular perovskite solar cells have an open circuit voltage of 1.0 V or above, but the majority of inverted perovskite solar cells have an open circuit voltage within the range of 0.7 V to 0.9 V, as shown in Figure 4.3 (c). The observation of low open circuit voltages in inverted perovskite solar cells were also reported by other groups: while the open circuit voltages of regular perovskite solar cells generally exceed 1.0 V [70], the open circuit voltages of inverted perovskite solar cells are mostly less than 0.9 V [90]. The observation of the differences in open circuit voltages gives rise to doubts on whether these two types of cells have similar working mechanisms.

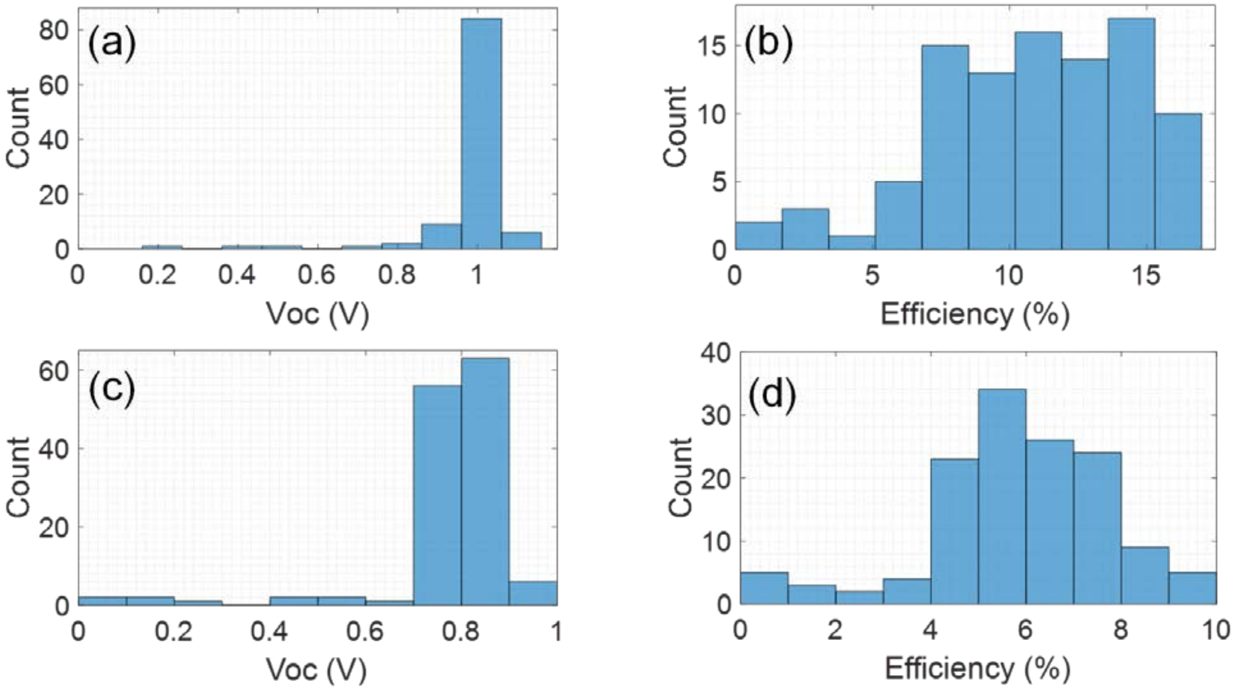

Figure 4.3. Statistical results of open circuit voltages and PCEs of regular and inverted perovskite solar cells. (a) Histogram of open circuit voltages of regular perovskite solar cells; (b) Histogram of PCEs of regular perovskite solar cells; (c) Histogram of open circuit voltages of inverted perovskite solar cells; (d) Histogram of PCEs of inverted perovskite solar cells.

Prior to KPFM measurement, SEM measurement was carried out on the cross-sectional surfaces of perovskite solar cells as a guide for the identification of different layers in KPFM images. In the sample preparation process for both SEM and KPFM measurements, fabricated cells were cut at the back of the glass substrates and the cleaved surfaces were directly characterized by SEM and KPFM. KPFM characterization on the cross-sectional surfaces of solar cells has always been a very challenging problem in community due to the rough surface resultant from sample preparation [81, 82, 87, 91]. Some groups used ion-beam milling to polish the cross-sectional surface prior to KPFM measurement [82, 87]. However, such treatment has a great possibility to introduce defects and charge doping to the cross-sectional surfaces, which could affect the SP distribution. To avoid any uncontrollable factors, we performed KPFM characterization on the fresh cut cross-sectional surfaces. We found that, with proper pressure, it is possible to obtain cleaved surfaces with roughness tolerable by KPFM. Also, before KPFM measurement was performed, distance compensation was done to make sure SP signals were not affected by the tip-sample distance, this means that the relatively rough cross-sectional surfaces would have minor effects on KPFM characterizations.

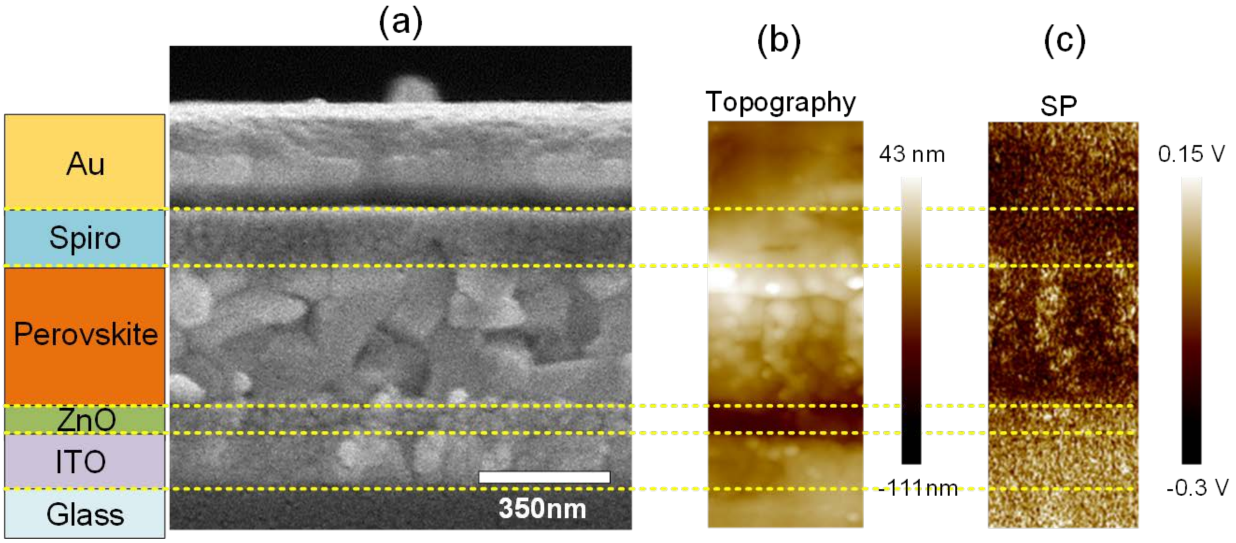

Figure 4.4. Cross-sectional images of the regular perovskite solar cell. (a) SEM image of the cross-sectional surface from regular perovskite solar cell, different layers in the cell are annotated on the left side; (b) Topography image of the cross-sectional surface; (c) SP image of the cross-sectional surface when the cell was under short circuit condition.

Figure 4.4 (a) is the SEM image of the cross-sectional surface of the regular perovskite solar cell, different layers in the cell were annotated with different colors on the left side. Figure 4.4 (b) and 4.4 (c) are topography image and SP image of the cross-sectional surface respectively. As can be observed from Figure 4.4 (b), the thickness of each layer obtained from KFPM measurement matches that of SEM image very well. Figure 4.4 (c) is the SP distribution of the cross-sectional surface when the cell was under short circuit condition. The differences in topography and variations in potential also helped the identification of each layer.

To observe the SP distribution inside the regular planar perovskite solar cell when it was at different working conditions, DC biases varied from -1.0 V to +1.2 V were applied to Au electrode while ITO was connected to the common ground. The positive sign here stands for forward bias while the negative sign stands for reverse bias. The corresponding results are shown in Figure 4.5. Figure 4.5 (a) is the KPFM images of the cross-sectional surface with bias voltage of -1.0 V, 0 V and +1.2 V, respectively. KPFM images from all biases are shown in Figure 4.6. Usually, a single scan line on the SP image is largely affected by the local features of the sample . To get a reliable SP profile of the device, 45 scan lines were averaged to obtain the SP profiles, electric field distribution inside the cell was then calculated with equation: $E = -\frac{d(\mathrm{SP})}{d(\mathrm{Distance})}$. Because KPFM signals usually contain a certain amount of Gaussian noise , taking the derivative directly will further exaggerate the noise and obscure the meaningful signals. To solve this issue, wiener filter was used to alleviate the Gaussian noises. The resultant SP profiles and electric distributions are shown in Figure 4.5 (b) and 4.5 (c), respectively. In Figure 4.5 (c), the electric field maximizes at perovskite/ZnO interface with depletion width of about 310 nm into perovskite layer (this number might be exaggerated due to the convolution effect of KPFM measurements [16]), while electric field is almost zero at perovskite/Spiro-OMeTAD interface and in Spiro-OMeTAD layer. This indicates that a p-n junction forms at perovskite/ZnO interface while an ohmic contact is formed at perovskite/Spiro-OMeTAD contact. Our observation supports the report by Jiang et al. that single junction was observed at electron transporting layer (ETL)/perovskite (TiO_2/perovskite in their case) interface and the cell has a junction structure of p-n type. On the other hand, we did not observe a potential barrier at perovskite/Spiro-OMeTAD interface as Bergmann et al. reported. Also from the electric field distribution we can infer that charge transport near perovskite/ZnO junction is affected by the electric field inside the depletion region while free charge carriers mainly diffuse through Spiro-OMeTAD layer before they are collected by the anode.

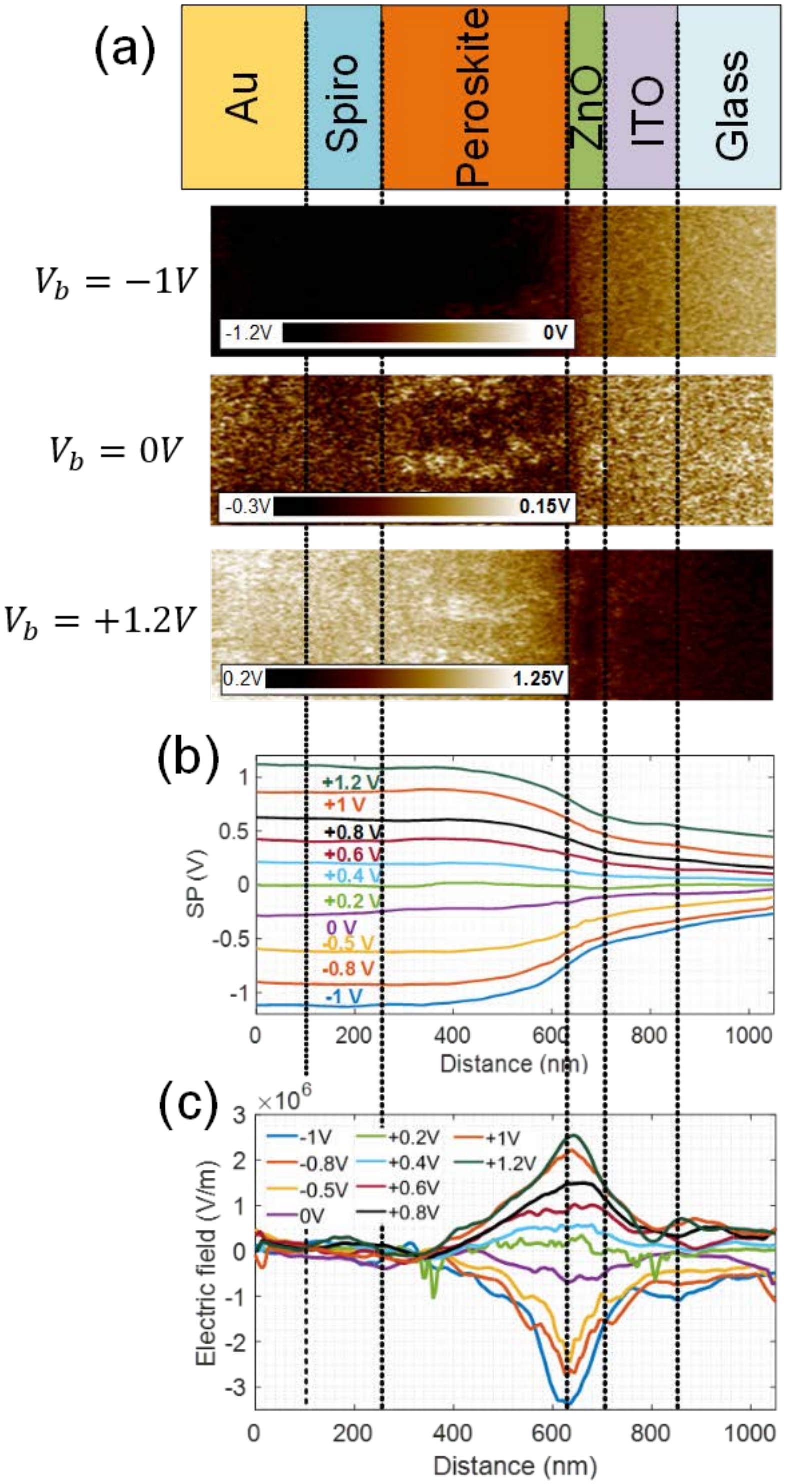

Figure 4.5. SP distribution on the cross-sectional surface of regular perovskite solar cell. (a) SP images of the cross-sectional surface under different biases; (b) SP profiles of the cross-sectional surface under different biases; (c) Electric field distribution of the cross-sectional surface under different biases.

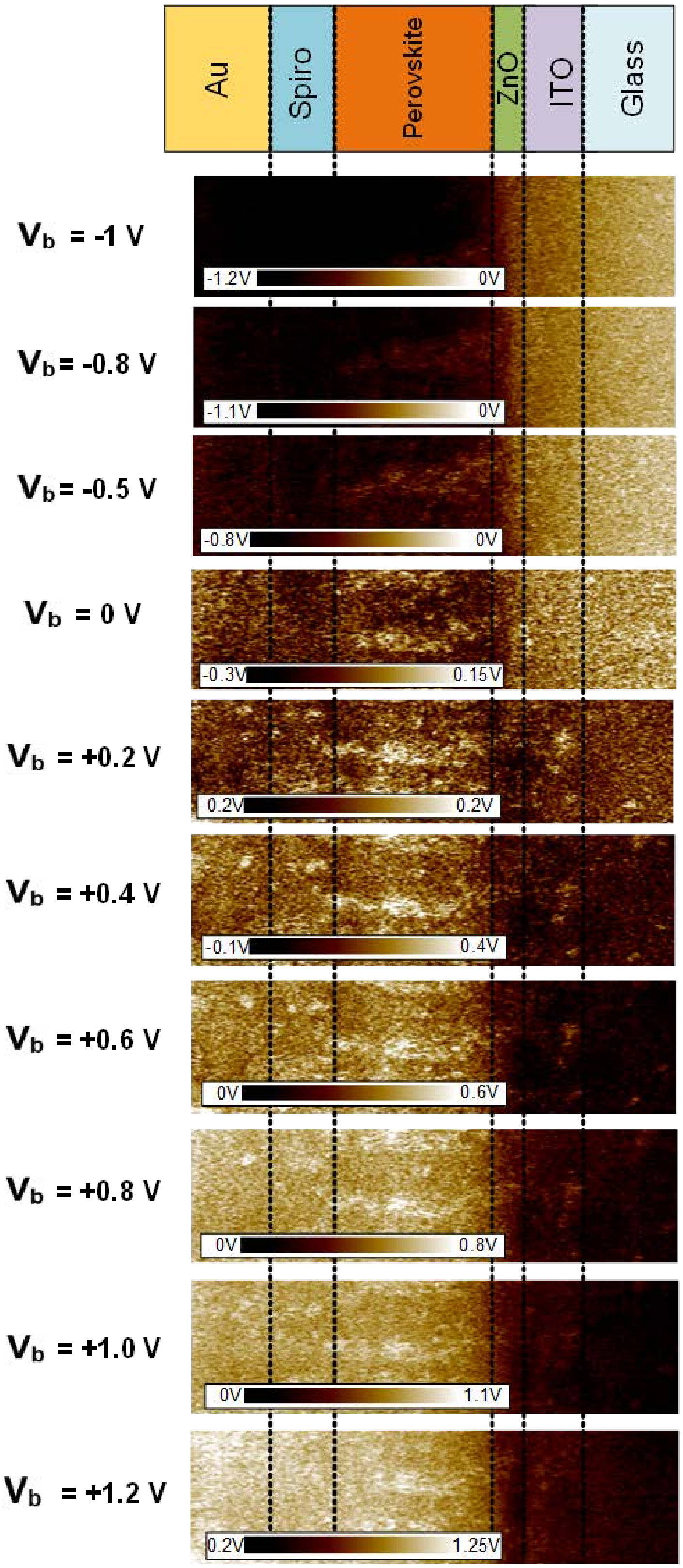

Figure 4.6. KPFM images of regular planar perovskite solar cells with different DC biases.

In comparison with the SP distribution of regular planar perovskite solar cell, the SP profiles inside inverted planar perovskite cell were also investigated. Similarly, SEM together with KPFM measurement were carried out to cross validate the identification of each layer on the cross-sectional surface. Shown in Figure 4.7, Figure 4.7 (a) is the SEM image of the cross-sectional surface, with each layer annotated with different color on the left side. Figure 4.7 (b) is the topography image of the cross-sectional surface and Figure 4.7 (c) is the corresponding SP image when the cell is under short circuit condition. Again, it can be told from Figure 4.7 that layers in KPFM measurement are in good accordance with the ones observed from SEM image.

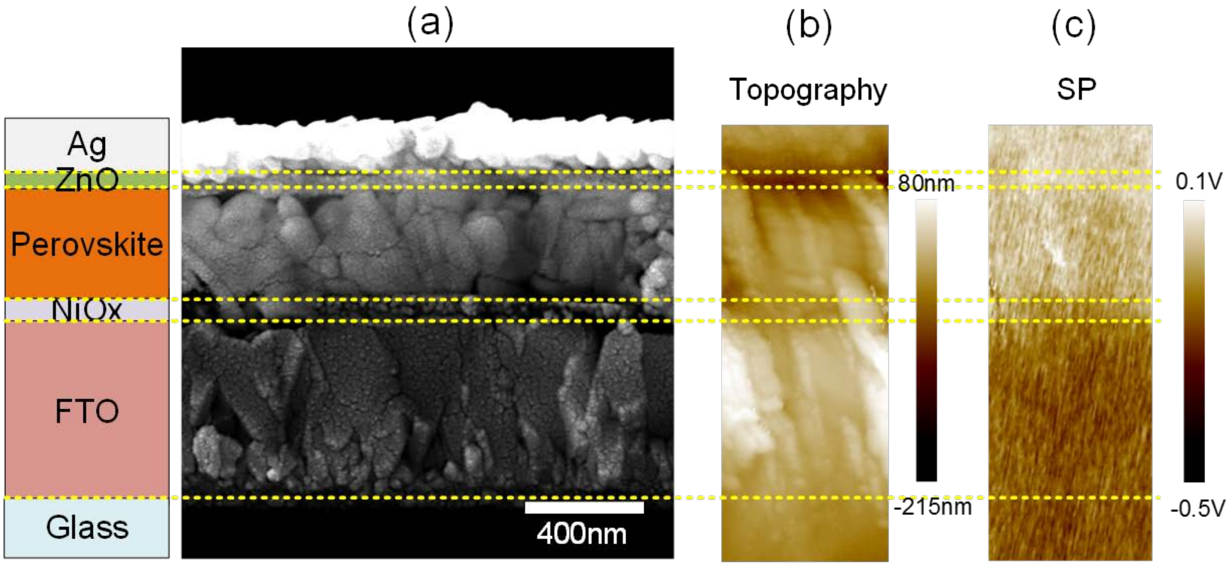

Figure 4.7. Cross-sectional images of the inverted perovskite solar cell. (a) SEM image of the cross-sectional surface from inverted perovskite solar cell, different layers in the cell are annotated on the left side; (b) Topography image of the cross-sectional surface; (c) SP image of the cross-sectional surface when the cell was under short circuit condition.

KPFM characterization on the cross-sectional surface was then carried out when the cell was biased at different DC voltages. During the measurement, Ag electrode was connected to the common ground while different biases were applied to FTO. The corresponding measurement results are shown in Figure 4.8. Figure 4.8 (a) shows the SP images of the cross-sectional surface when the cell was biased at -0.2 V, 0 V and +1.5 V, respectively. All KPFM images are shown in Figure 4.9. Again, 45 scan lines of the KPFM image were averaged to obtain SP profiles of the cross-sectional surface, as shown in Figure 4.8 (b). We noticed in our I-V characterization that, for most of the inverted perovskite solar cells, when biases below -0.2 V were applied to FTO electrode, the cell would break down with high current, thus, it is improper to bias the cell with voltage lower than -0.2 V in KPFM characterization. Again, electric field inside the cell was calculated and corresponding results are shown in Figure 4.8 (c). Similar calculation and filter techniques were applied during the data processing. Shown in Figure 4.8 (c), electric field inside the inverted perovskite solar cell has two local maxima, one of which occurs at perovskite/ZnO interface while the other one locates at perovskite/NiO_x interface. The electric field inside perovskite layer is relatively constant compare to the drop at perovskite/ZnO and perovskite/NiO_x interfaces. This observation indicates that, different from the p-n junction we observed in regular perovskite solar cells, the junction inside inverted perovskite solar cell is a p-i-n junction. Charge transportation inside inverted perovskite solar cells is affected by drift due to the existence of electric field all through the device.

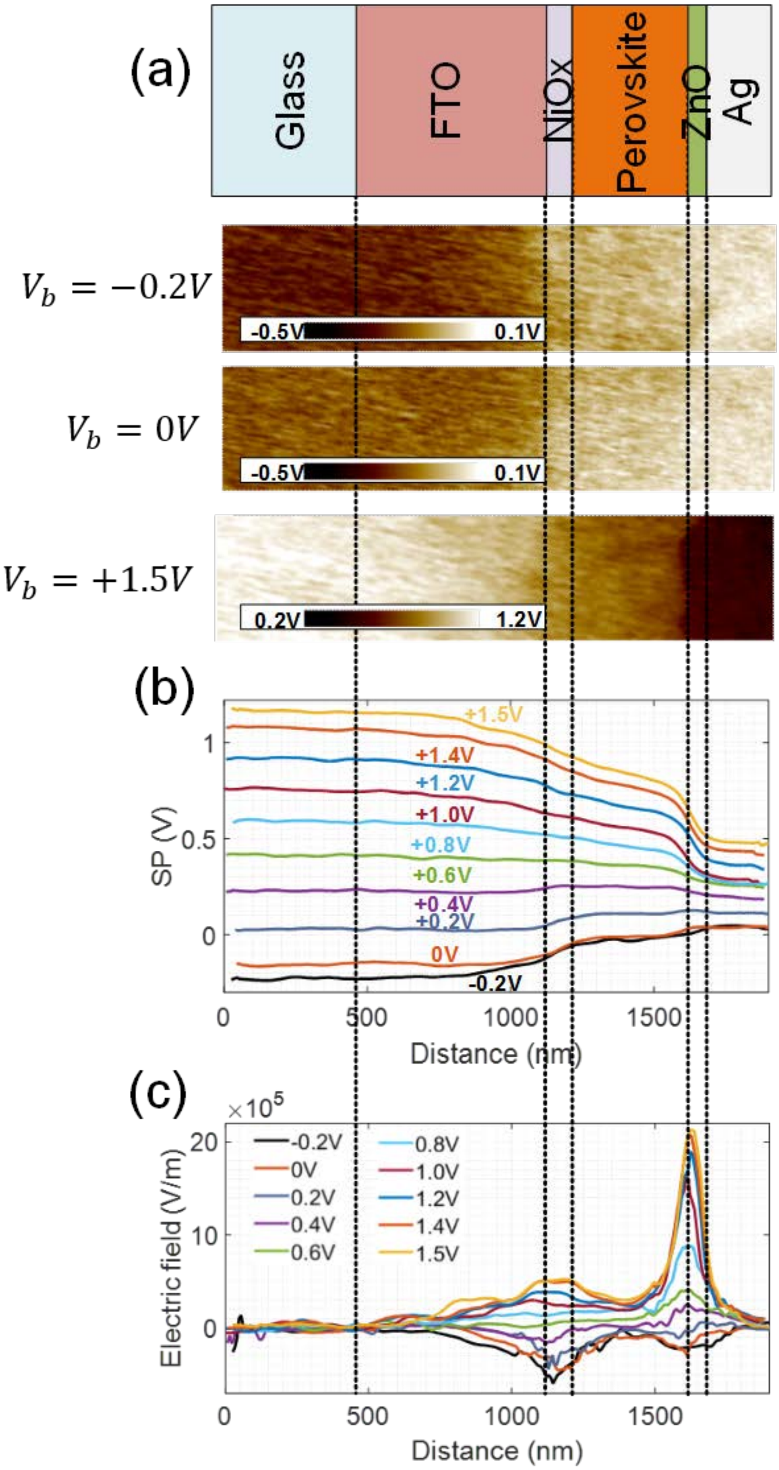

Figure 4.8. SP distribution on cross-sectional surface of the inverted perovskite solar cell. (a) SP image of the cross-sectional surface under different biases; (b) SP profiles of the cross-sectional surface under different biases; (c) Electric field distribution of the cross-sectional surface under different biases.

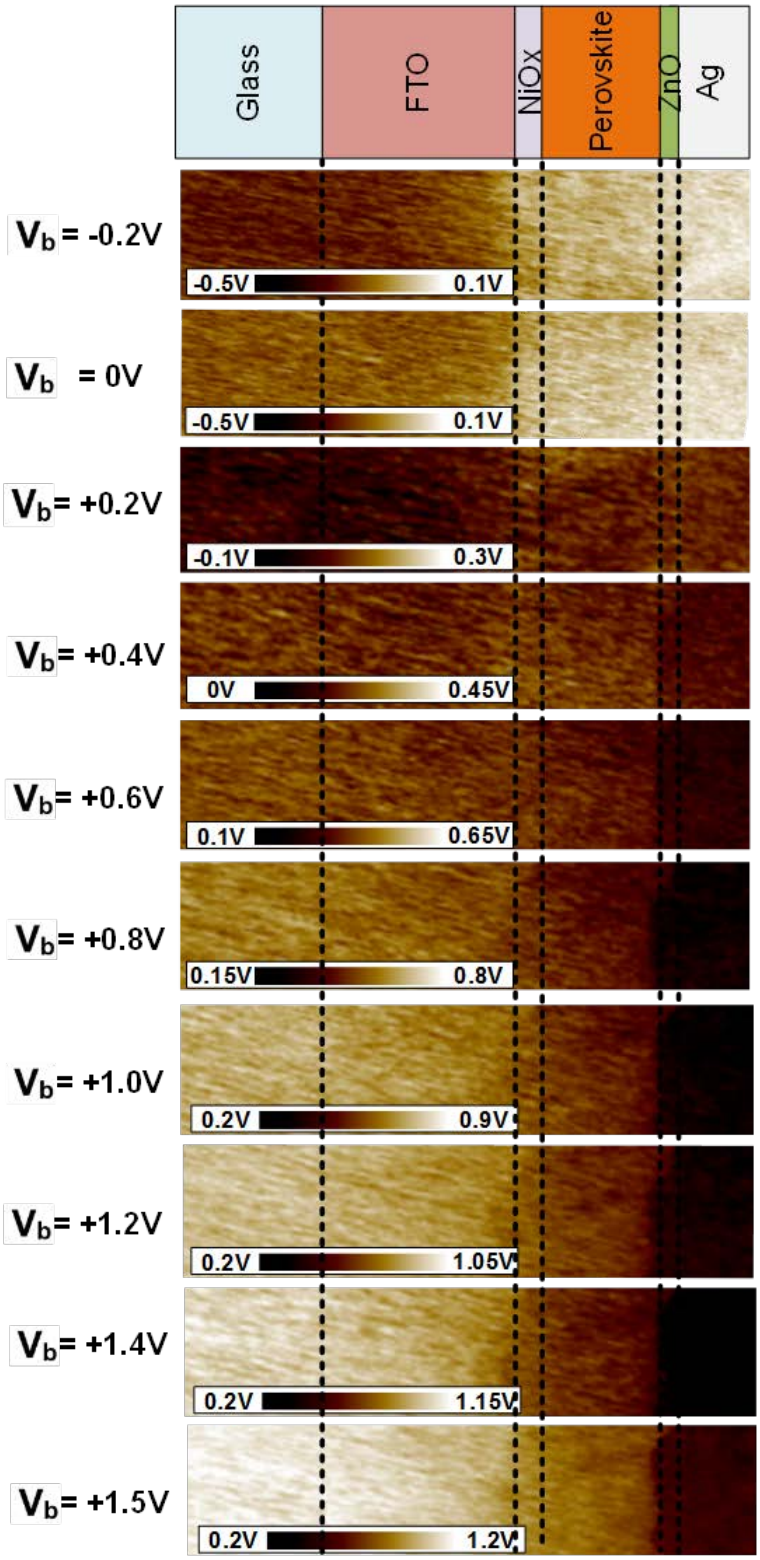

Figure 4.9. KPFM images of inverted planar perovskite solar cells with different DC biases.

To clarify the cause of low open circuit voltages observed in inverted planar perovskite cells, we substrate the SP profiles obtained at different biases with the SP profile obtained at short circuit condition. This subtraction removes the SP signals contributed from the work function of different layers, and the voltage drop in the resultant profiles is governed by charge injection impedance [86]. Thus, it is possible for us to identify charge injection barriers at large voltage drop locations. The resultant relative SP profiles are shown in Figure 4.10. Figure 4.10 (a) is the relative SP profiles in regular perovskite solar cell while Figure 4.10 (b) shows the relative SP profiles in inverted perovskite solar cell. As can be observed from Figure 4.10 (a), in regular perovskite solar cells, the applied voltages mainly drop at perovskite/ZnO interface. This indicates that the charge injection barriers only appear at perovskite/ZnO contact while the resistance from perovskite layer, spiro-OMeTAD layer as well as perovskite/spiro-OMeTAD contact are negligible in this type of cell. However, for inverted perovskite solar cell, besides the voltage drop at perovskite/ZnO interface, voltage drop was also observed at perovskite/NiO_x interface. This implies the existence of an additional charge injection barrier at perovskite/NiOx contact. We did notice the drop of bias voltages in FTO and ITO layers, considering the conductivity of FTO and ITO are much higher than that of perovskite, such voltage drop is probably due to the nonlocal coupling between KPFM probe and the sample surface [92]. The schematic of the charge injections barriers in regular and inverted perovskite solar cells are demonstrated in Figure 4.10 (c) and (d), respectively.

We want to point out that open circuit voltages of both cells were measured after KPFM characterization to ensure our cells were working during our measurement. Decreases in open circuit voltages were noticed for both cells, but the changes were within 10% of the original open circuit voltages. This ensures that the SP profiles we acquired are from working cells and they reflect typical SP/electric field distributions. In addition, one may notice that not all SP profiles start from 0 nm. This is due to the compensation we made for the thermal drift in KPFM measurement. We aligned all the images for each cell to a common feature found in topography.

For each type of perovskite solar cell, cross-sectional characterization work was repeated to ensure our experiments are reproducible and results are reliable.

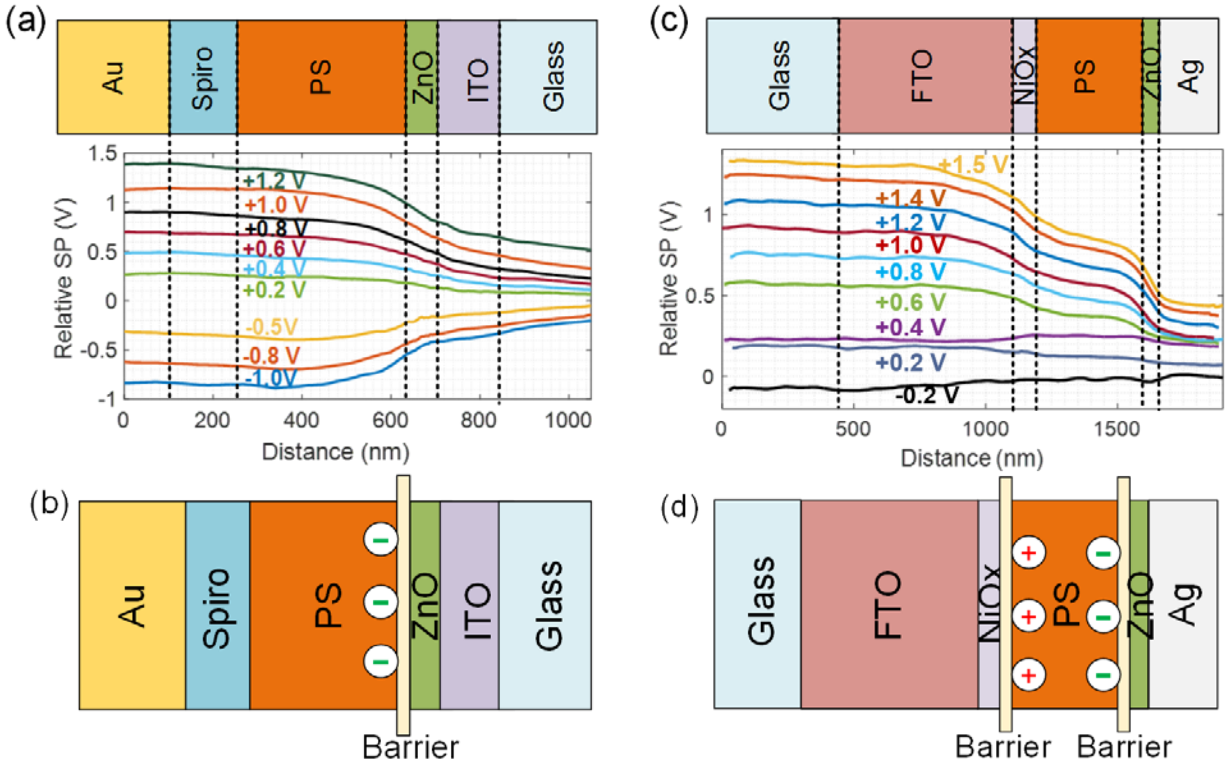

Figure 4.10. Relative SP profiles in regular and inverted planar perovskite solar cells and the schematics of charge injection barriers inside the cells. (a) Relative SP profiles in regular perovskite solar cell under different biases; (b) Relative SP distribution in inverted perovskite solar cell under different biases; (c) Schematic of charge injection barriers in regular perovskite solar cell; (d) Schematic of charge injection barriers in inverted perovskite solar cell. (PS is abbreviation for perovskite)

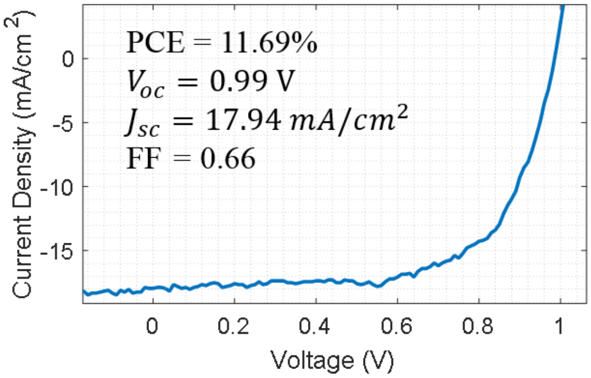

Figure 4.11. I-V curve of the second perovskite solar cell with regular structure tested in the cross-sectional characterization.

Shown in Figure 4.11 is the I-V curve of the second regular perovskite solar cell that was characterized. The cell has an open circuit voltage of 0.99 V, a short circuit current of 17.94 mA/cm^2, a FF of 0.66 and an overall PCE of 11.69%. SP profiles of the cell with different biased are shown in Figure 4.12. Figure 4.12 (a) is the SP profiles of the cross-sectional surface, Figure 4.12 (b) is the electric field calculated from the SP profiles and Figure 4.12 (c) is the relative SP profiles of the cell under different biases. Similarly, single p-n junction is observed at perovskite/ZnO interface, while an ohmic contact forms at perovskite/Spiro-OMeTAD interface. Also, as can be observed from the relative SP profiles, voltage drop mainly occurs at perovskite/ZnO interface, indicating the formation of charge injection barriers. Topography image as well as KPFM images from all biases are shown in Figure 4.13.

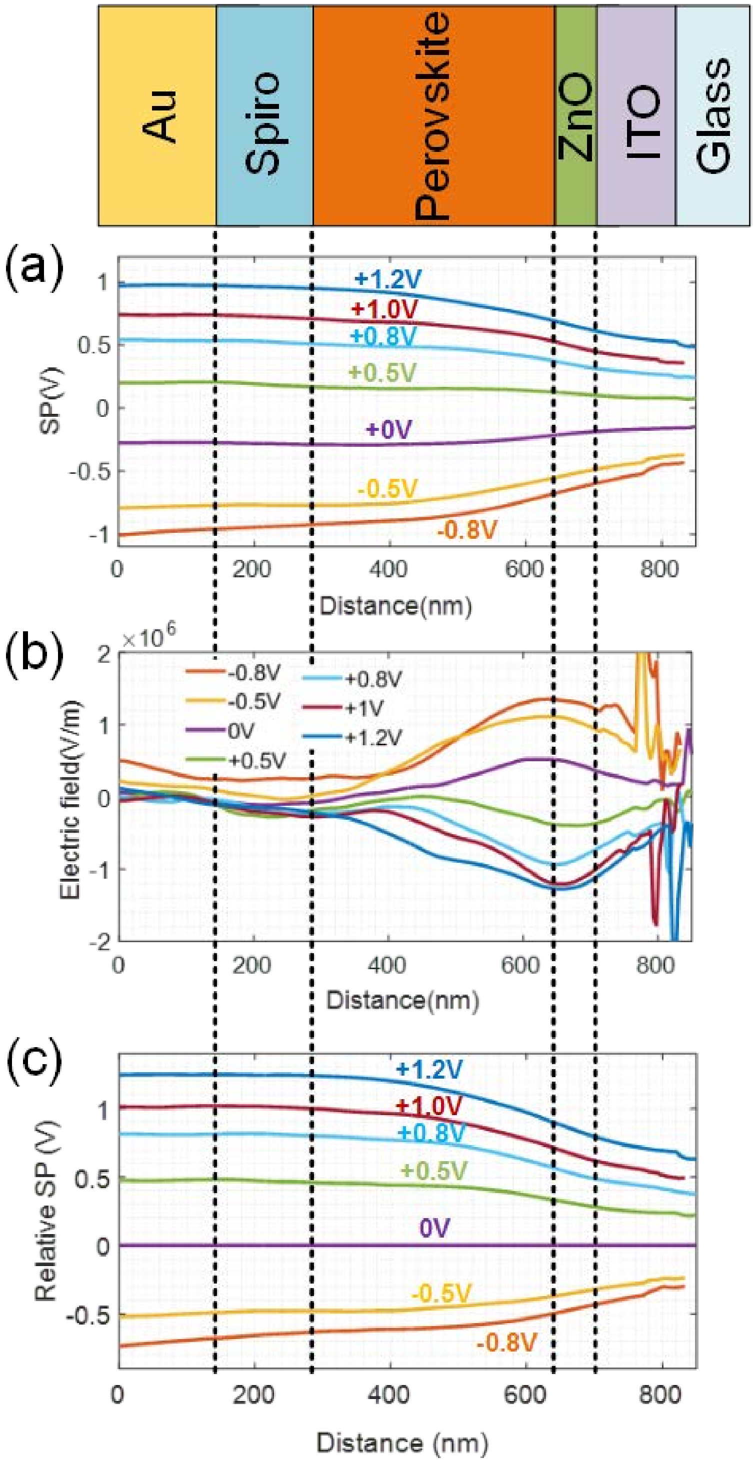

Figure 4.12. KPFM characterization result of the regular perovskite solar cell. (a) The SP profiles of the regular perovskite solar cell under different bias voltages; (b) Electric field of the cross-sectional surface calculated from the SP profiles and (c) Relative SP profiles of the regular perovskite solar cell under different biases.

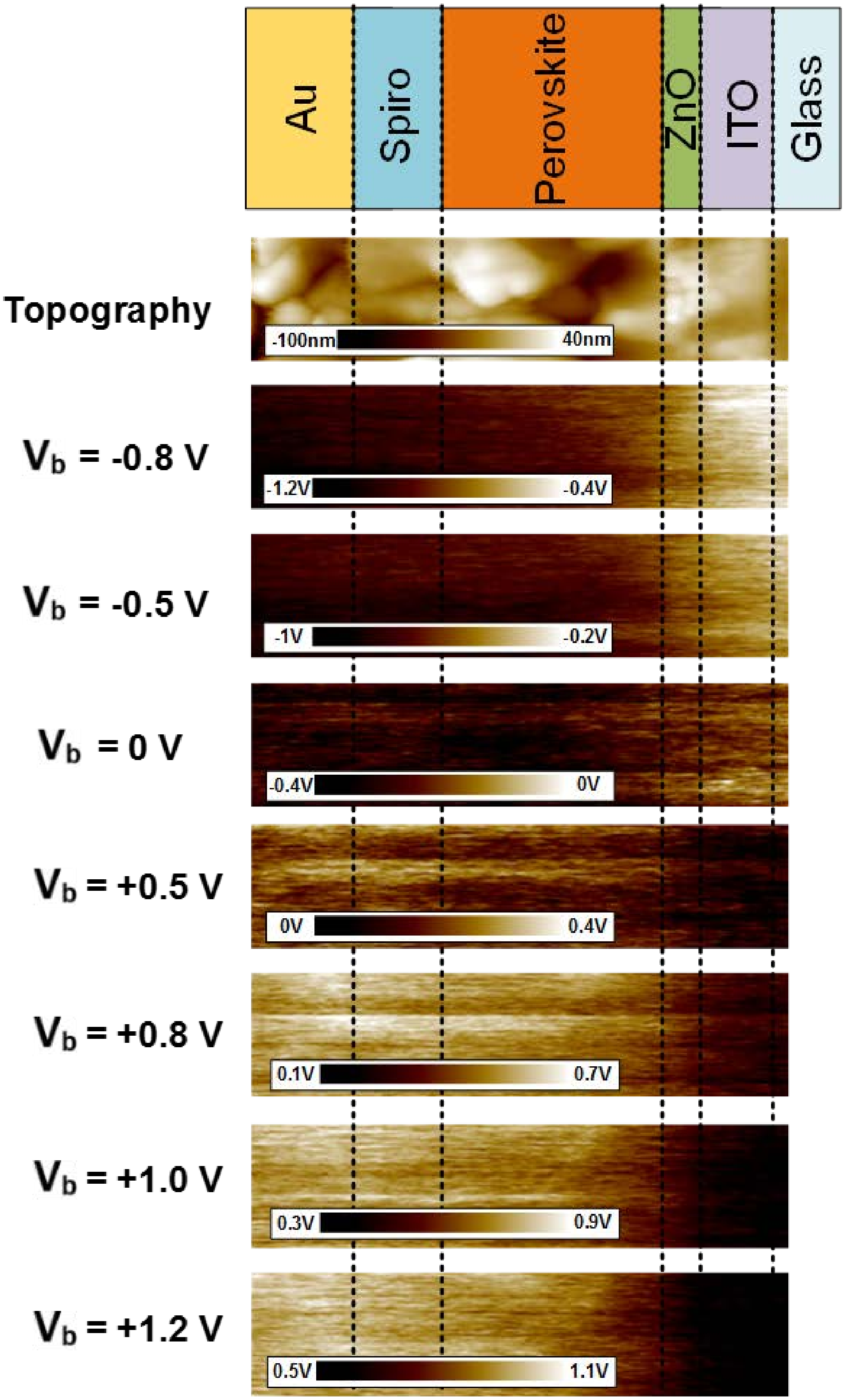

Figure 4.13 Topography image and SP images of the second regular perovskite solar cell with different DC biases.

KPFM characterization on inverted perovskite solar cells was also repeated. Figure 4.14 is the I-V curve of the inverted perovskite solar cells used in the characterization. With an open circuit voltage of 0.77 V, a short circuit current of 10.55 mA/cm^2 and a FF of 0.72, the cell has a PCE of 5.85%. SP profiles of its cross-sectional surface were obtained under different biases and are shown in Figure 4.15.

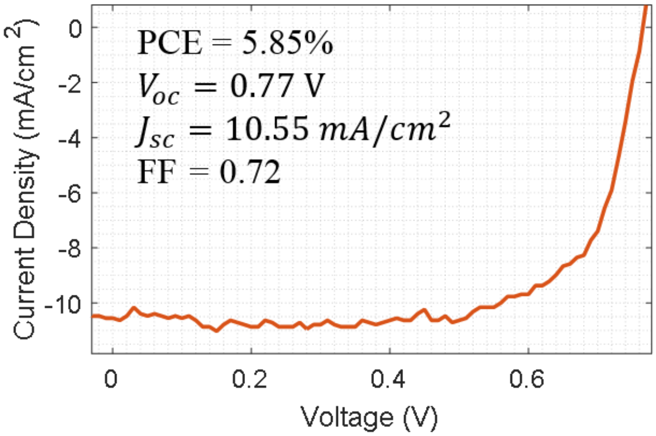

Figure 4.14. I-V curve of the second perovskite solar cell with inverted structure tested in the cross-sectional characterization.

In Figure 4.15, (a) is the SP profiles of the cross-sectional surface obtained at different biases; (b) is the electric field distribution within the cell calculated from the SP profiles and (c) is the relative SP profiles at different biases. From the electric field distribution curves, two local maxima were observed at perovskite/ZnO and perovskite/NiO$_x$ interfaces respectively. This confirms that the junction structure inside the inverted perovskite solar cells is p-i-n. In addition, from the relative SP profiles, charge injection barriers were observed at both perovskite/ZnO and perovskite/NiO$_x$ contacts, which confirms our previous observation. Figure 4.16 shows the topography image as well as all SP images of the inverted perovskite solar cell under different biases.

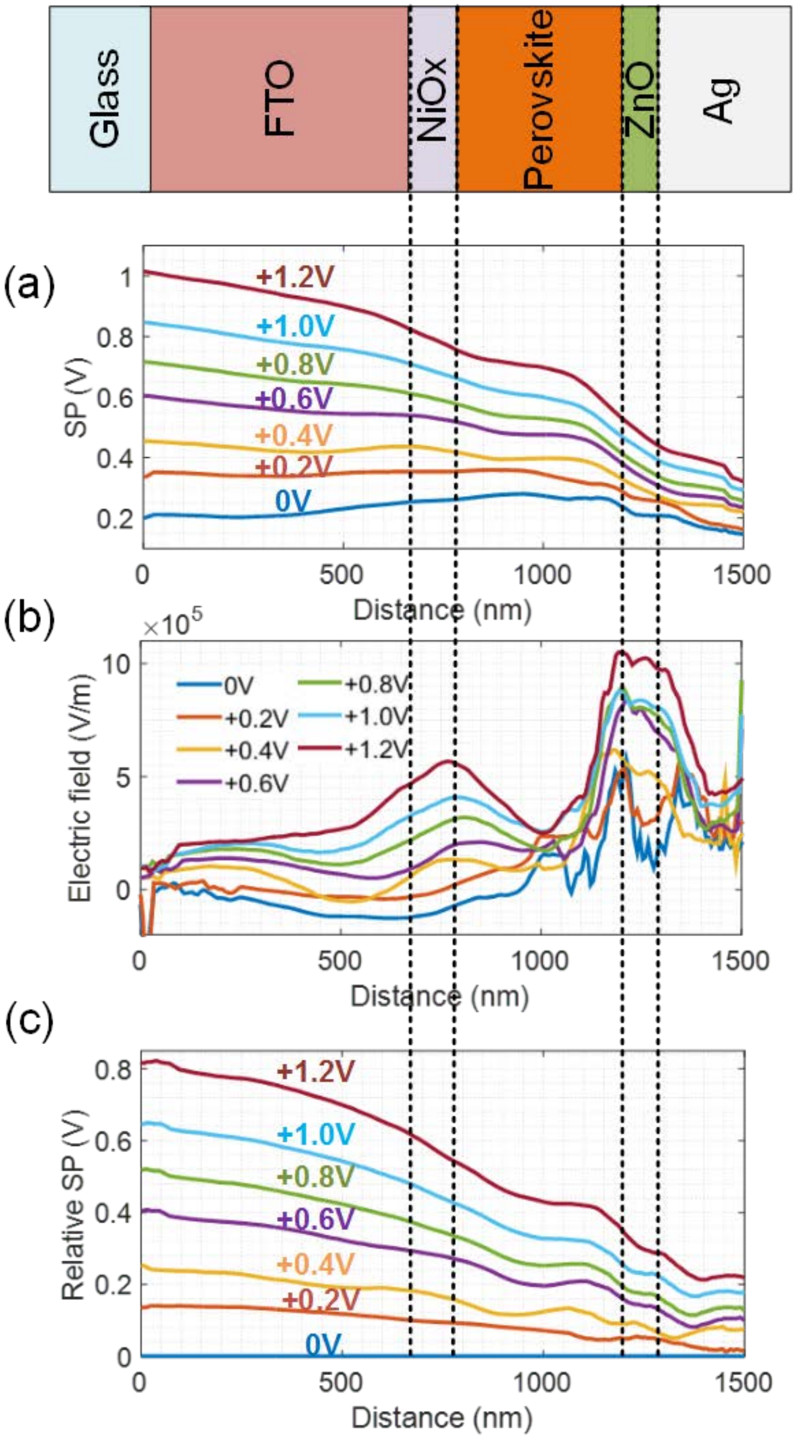

Figure 4.15. KPFM characterization result of the inverted perovskite solar cell. (a) The SP profiles of the inverted perovskite solar cell under different bias voltages; (b) Electric field of the cross-sectional surface calculated from the SP profiles and (c) Relative SP profiles of the inverted perovskite solar cell under different biases.

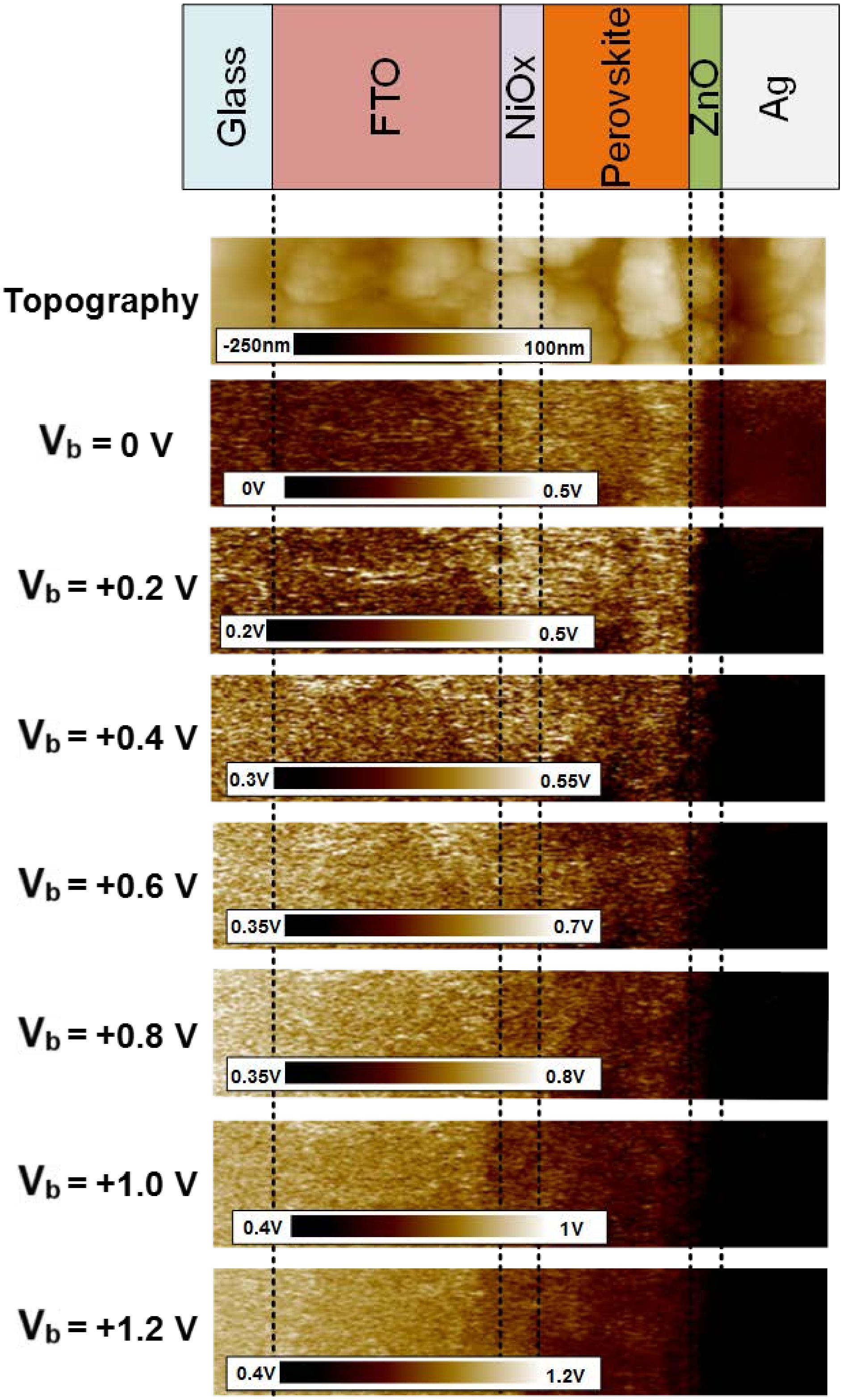

Figure 4.16. Topography image and SP images of the second inverted perovskite solar cell with different DC biases.

The observation of barriers at perovskite/NiO_x contact in inverted perovskite cells provides explanations for their low open circuit voltages. For regular planar perovskite cells, injection barriers were only observed at perovskite/ZnO contact, while for inverted planar perovskite cells, charge injection barriers appeared at both perovskite/ZnO and perovskite/NiOx contacts, the additional barriers increase the probability of charge recombination in inverted perovskite solar cells, as a result, low open circuit voltages were generally observed in this type of solar cells.

4.4 OPEN CIRCUIT VOLTAGE DECAY (OCVD) MEASUREMENT

Our conjecture was verified by the measurement of electron lifetime using open circuit voltage decay (OCVD) technique. In OCVD measurement, fabricated perovskite solar cells were illuminated by solar simulator at open circuit voltage, after the establishment of a steady open circuit voltage, light was block from perovskite solar cells and the decay of open circuit voltage was recorded as a function of time. Then, electron life time was calculated using equation [93]:

$$\tau_n = -\frac{k_B T}{q}\left(\frac{dV_{oc}}{dt}\right)^{-1} \tag{4.1}$$

where $k_B T$ is the thermal energy, q is the elementary charge and $\frac{dV_{oc}}{dt}$ is the derivative of open circuit voltage with respective to time. Four regular perovskite solar cells and four inverted perovskite solar cells with different PCEs were chosen for the measurement. The PCEs of regular perovskite solar cells ranged from 10.7% to 16.7% while the PCEs of inverted perovskite solar cells ranged from 3.6% to 7.7% (I-V curves of all the cells used in the characterization are shown in Figure 4.18, and their I-V characterizations are shown in Table 4-1 and 4-2 respectively). Shown in Figure 4.17, the electron lifetimes for both regular and inverted perovskite solar cells are in the timescale of 10^{-2} to 10 s, demonstrating a persistent photovoltage decay. As pointed out by Baumann et al. and Nagaoka et al. in their work [94, 95], while a fast decay with a timescale of $<10^{-4}$ s indicates the direct recombination of free charge carriers inside the active layer, the persistent photovoltage decay with a time scale of millisecond to second should be caused by the recombination of free charge carriers that were already in the active layer with the oppositely charged carriers that were transported back to the active layer from transporting layers due to injection barriers [94]. In our OCVD measurement, with lifetimes in the timescale of 10^{-2} to 10 s, direct charge recombination was not observed in our perovskite solar cells and the charge recombination were mainly governed by the second type mentioned above. The shorter electron lifetime in inverted planar perovskite solar cells implies a stronger charge recombination which confirms the presence of additional barriers in inverted perovskite solar cells.

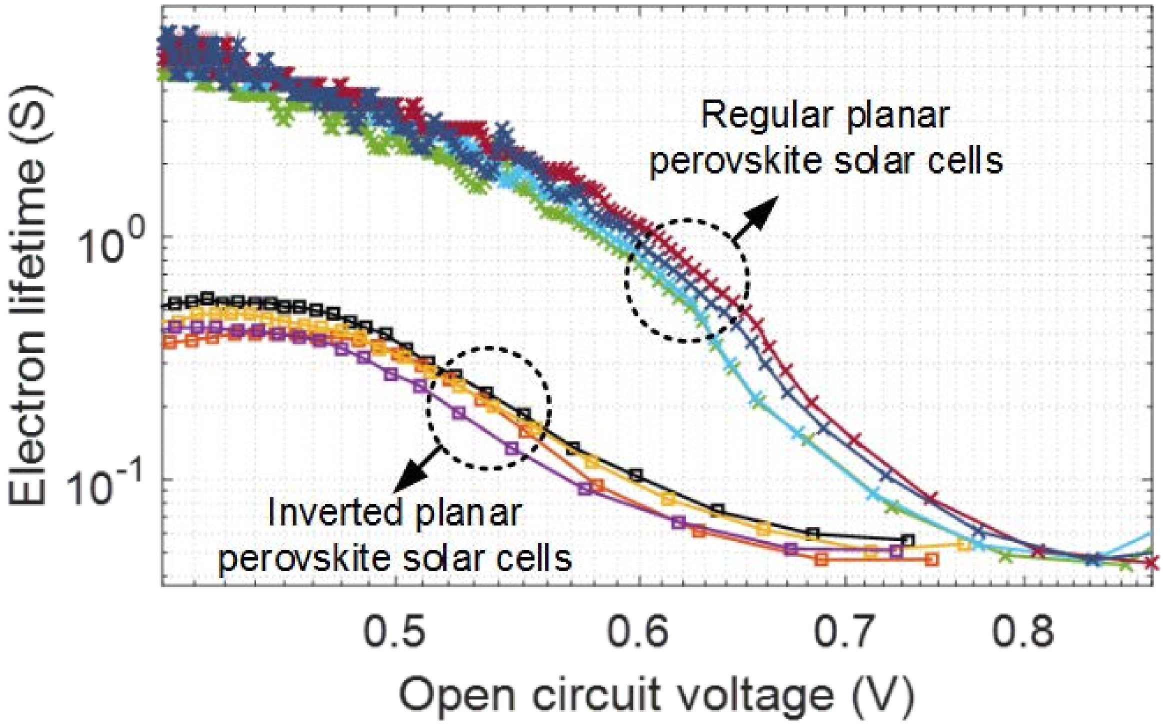

Figure 4.17. Electron lifetime of regular and inverted perovskite solar cells measured by OCVD.

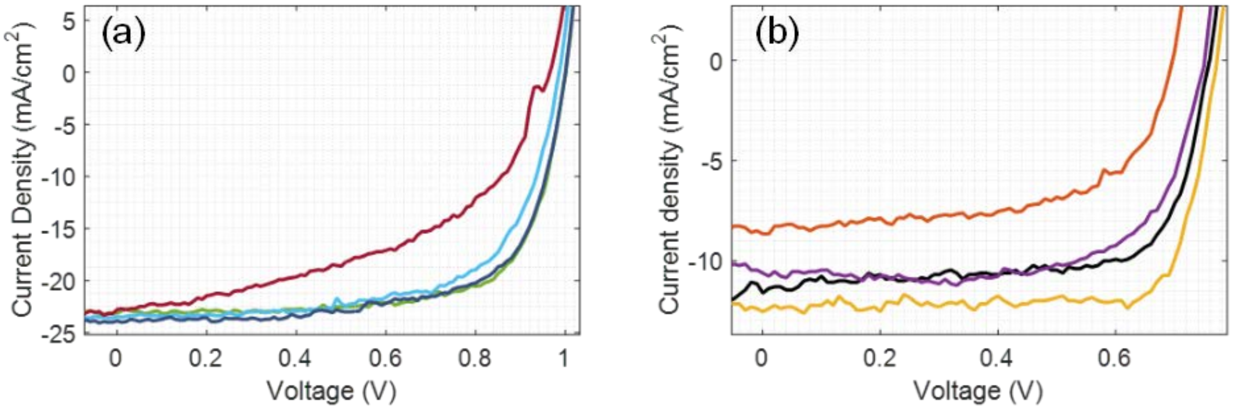

Figure 4.18. I-V curves of the perovskite solar cells used in OCVD measurements. (a) I-V curves of the regular perovskite solar cells used in OCVD measurements; (b) I-V curves of the inverted perovskite solar cells used in OCVD measurements.

Table 4-1 I-V characterization of the regular perovskite solar cells tested in the OCVD measurement

	PCE (%)	Short circuit current (mA/cm^2)	Open circuit voltage (V)	Fill factor
Cell 1	10.69	22.77	0.97	0.48
Cell 2	15.17	23.44	0.99	0.65
Cell 3	16.21	23.87	1	0.68
Cell 4	16.69	23.12	1	0.72

Table 4-2 I-V characterization of the inverted perovskite solar cells tested in the OCVD measurement

	PCE (%)	Short circuit current (mA/cm^2)	Open circuit voltage (V)	Fill factor
Cell 1	3.62	8.66	0.7	0.6
Cell 2	5.24	10.62	0.75	0.69
Cell 3	6.16	11.61	0.76	0.69
Cell 4	7.68	12.54	0.77	0.79

4.5 SUMMARY

To sum up, with KPFM measurement on the cross-sectional surface of planar perovskite solar cells, a clear picture on charge transport mechanisms and charge injection barriers are obtained. In regular planar perovskite solar cells, p-n junction forms at perovskite/ZnO interface with a depletion region of around 310 nm into perovskite layer. Charges transport in this region is affected by electric field while they diffuse through spiro-OMeTAD layer with negligible resistance. On the other hand, p-i-n junction forms in inverted perovskite solar cells and charge transport is affected by electric fields in such devices. The locations of charge injection barriers were also identified with KPFM measurements. For regular planar perovskite solar cells, charge injection barriers were only observed at perovskite/ZnO contact while in inverted perovskite solar cells, charge injection barriers were observed at both perovskite/ZnO and perovskite/NiO_x interfaces, the appearance of charge injection barriers exacerbates the charge recombination in perovskite solar cells and as a result, inverted perovskite solar cells demonstrated lower open circuit voltages.

The reasons for the appearance of charge injection barriers at perovskite/metal oxide interface could due to unfavorable band alignment or the limited interface contact between perovskite layer and metal oxide layer [96], in either case, contact engineering is highly desired for further optimization of both regular and inverted planar perovskite solar cells.

5.0 CONCLUSION AND FUTURE WORK

5.1 MAJOR ACCOMPLISHMENTS

In this thesis, the modeling of KPFM imaging system and the application of KPFM in the characterization of solar cells are discussed.

KPFM imaging system is modeled as a time-invariant system with measurement equals to the convolution of true SP distribution of the sample with the PSF of the KPFM system. The convolution degrades the resolution and accuracy of the acquired SP image. To restore the resolution as well as accuracy, PSF of our KPFM system is calibrated experimentally with calibration electrode pair. Compared with PSF calculated with theoretical models, our method takes into consideration the real probe shape and cantilever effect which makes the PSF more accurate. Then, with the calibrated PSF, a non-linear deconvolution algorithm based on total-variation regularization is utilized to suppress the noises as well as restore the resolution in measured KPFM images. As shown in chapter 2, the deconvoluted images not only demonstrated much lower noise level, the signal intensities in deconvoluted images are enhanced, indicating the improvement of resolution as well as accuracy.

The application of KPFM in the characterization of solar cells are demonstrated in chapter 3 and chapter 4. In chapter 3, KPFM is utilized in clarifying the charge transport mechanism between SWNT and polymers in organic solar cells. By observing the SP change in SWNTs in electron-enriched and hole-enriched environment respectively, we find that holes can be transfer to SWNTs from polymer phase while electrons are blocked in the polymer phase from SWNTs.

This finding indicates that SWNTs doping improves the hole mobility in organic solar cells and is beneficial for the balance of carrier mobility in organic solar cells.

In chapter 4, KPFM is utilized in the understanding of working mechanisms of perovskite solar cells. SP profiles of the cross-sectional surfaces of both regular and inverted planar perovskite solar cells are characterized with KPFM. Junction structures and charge transport mechanisms in planar perovskite solar cells are revealed from analyzing the SP profiles. In addition, charge injection barriers in planar perovskite solar cells are identified with relative SP profiles. Our measurement indicates that the inefficient charge extraction is a major problem affecting the performance of planar perovskite solar cells.

5.2 DISCUSSION AND FUTURE WORK

5.2.1 Experimental calibration of PSF of the KPFM system

In the calibration of the PSF of our KPFM system, PSF is obtained by comparing the ideal SP potential of the calibrate electrode with the measurement by our KPFM system. The choice of using electrode pair as the calibration pattern is based on the goal of creating a step response of our KPFM system. However, due to our limited proficiency with EBL, the electrode pair we fabricated still has a gap of couple hundred nanometers. In fact, the accuracy of the calibrated PSF is highly affected by the calibration pattern since it needs an accurate modeling of the ideal SP distribution and a rigor alignment between the simulation and the measurement. On the other hand, such difficulties can be waived if point calibration pattern can be fabricated, as shown in Figure

5.1. With the point calibration pattern, the measurement of the pattern itself will be the PSF of the KPFM system. This is the most accurate and direct way to calibrate the PSF of a KPFM system.

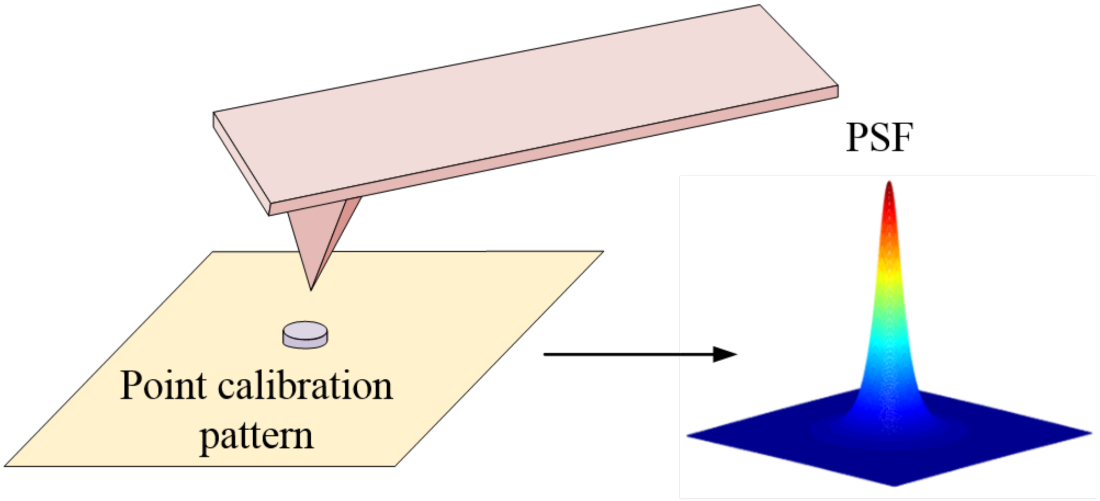

Figure 5.1. Calibration of PSF using point calibration pattern, the measurement by KPFM is the PSF of the system.

The biggest challenge in the fabrication of point calibration pattern is achieving a pattern size of several nanometer or sub nanometer since the resolution of the KPFM is determined by the point source response. One way to fabricate the point calibration pattern is through EBL. As demonstrated in Figure 5.2, a layer of insulator is coated on top of a metal substrate before EBL is used to write a point pattern. With development, coating of another metal and finally liftoff, point calibration pattern can be obtained. Obviously, the size of the point calibration pattern is limited by the resolution of EBL, but considering that EBL has been demonstrated to be capable of fabricating features less than 10 nm [97], such method should be practical.

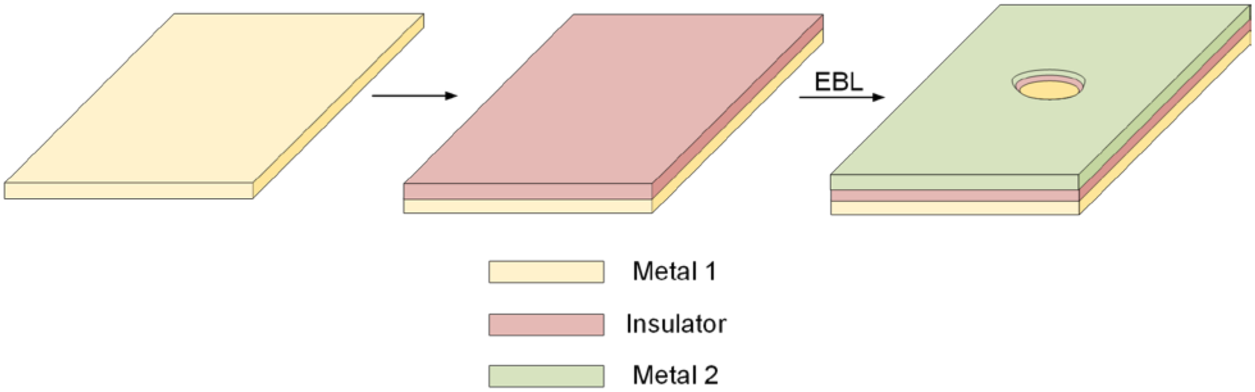

Figure 5.2. Demonstration of fabricating point calibration pattern using EBL.

The other technique that can be utilized in the fabrication of point calibration pattern with nanometer size is nanoimprint. Demonstrated by Chou et al. in their work [98], they can already fabricate metal dot with diameter of 6 nm in 1997. Austin et al. reported that they were able to fabricate a linewidth of 5 nm with nanoimprint in 2004 [99]. With the development of the technique, the fabrication of point calibration pattern with a size of nanometer or sub-nanometer is promising.

In additional, with the point calibration pattern, a systematic measurement with different tip-sample distance and different measurement parameters can be carried out to give a comprehensive library of PSFs. For the deconvolution of a specific tip-sample system and a specific set of parameters, PSF can be directly read from the library and applied in the deconvolution process. This should provide a straightforward solution to obtaining the PSF of a KPFM system with different parameters.

5.2.2 Applications of KPFM

5.2.2.1 Further research in the cross-sectional characterization

In our characterization of the cross-sectional surface of perovskite solar cells, all the characterizations were performed in dark ambient condition with different biases provided by a voltage supplier. As reported by Chen et al. [87] and verified by ourselves, SP profiles of the cross-sectional surface under illumination can be simulated with the SP profiles measured in dark with certain biases. As demonstrated in Figure 5.3. Figure 5.3 (a) is the device structure under test; Figure 5.3 (b) through (g) are SP images of the cross-sectional surface of the sample measured in dark with different biases; Figure 5.3 (h) shows the SP distribution of the cross-sectional surface measured in short circuit condition under illumination and Figure 5.3 (i) shows the SP distribution of the cross-sectional surface measured in open circuit condition under illumination. As can be observed from Figure 5.3, the SP distribution measured in dark with a forward bias voltage of 0.8 V is similar to the measurement obtained under illumination in open circuit condition, indicating that the SP distribution measured under illumination can be simulated by the SP distribution measured in dark with proper biases. Ideally, we expect that SP distribution measured under one sun condition in open circuit condition to be equivalent to the SP distribution measured in dark with forward bias at the open circuit voltage. However, since the light source used in our KPFM measurement is not calibrated, such predictions still need to be verified.

In addition, although it is possible to bias the solar cells with different voltages to simulate their working conditions, characterizing the SP distribution of the solar cells with different illuminating conditions is more straightforward. In the future, SP distribution of the cross-sectional surface should be characterized under different illumination and biases for a more comprehensive study.

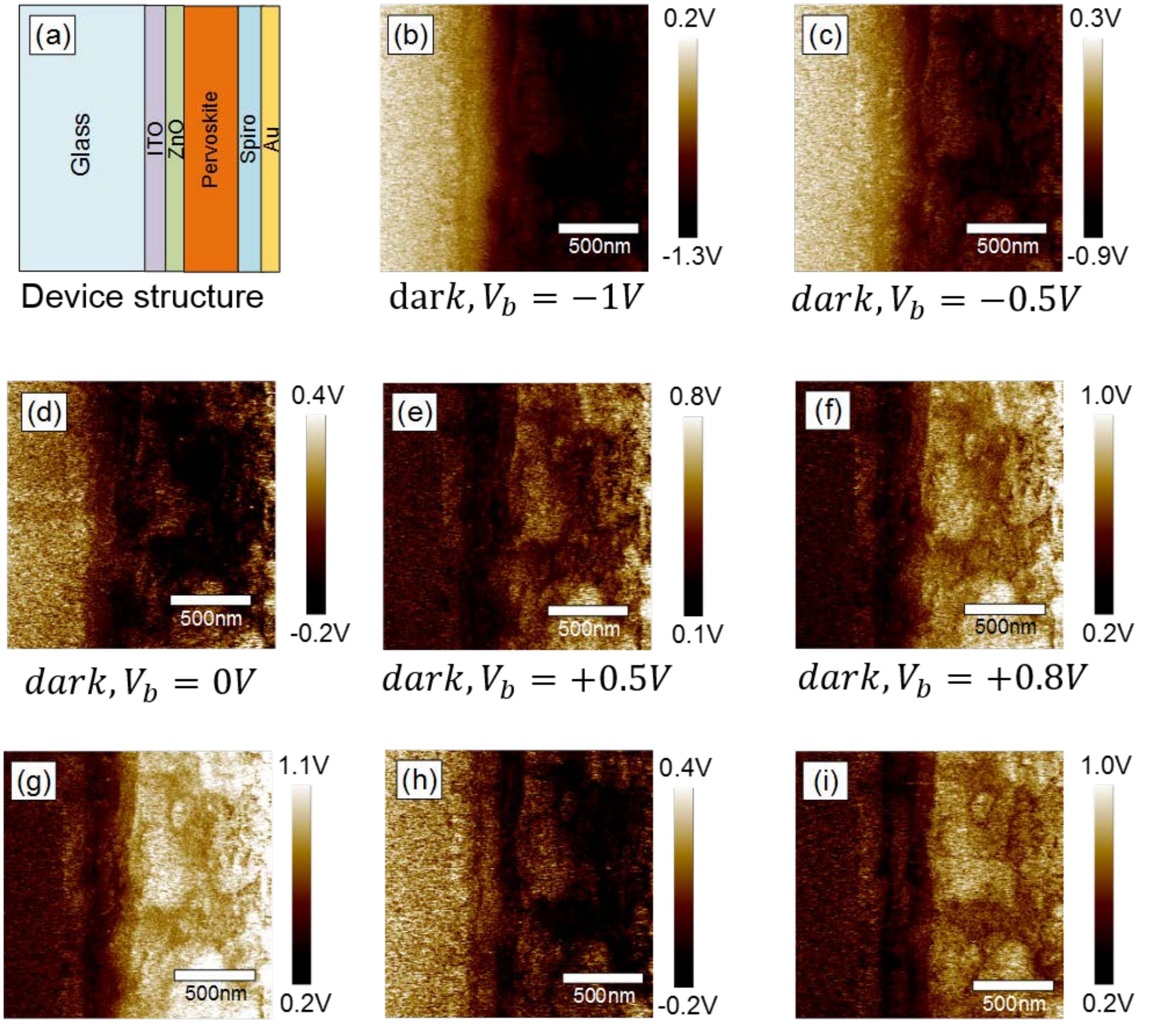

Device structure

$dark, V_b = -1V$

$dark, V_b = -0.5V$

$dark, V_b = 0V$

$dark, V_b = +0.5V$

$dark, V_b = +0.8V$

$dark, V_b = +1V$

Short circuit under illumination

Open circuit under illumination

Figure 5.3. SP distribution of regular planar perovskite solar cell under different illumination and bias conditions. (a) Device structure of the cell under test; (b) SP distribution measured in dark with bias voltage of -1 V (negative sign means reverse bias); (c) SP distribution measured in dark with bias voltage of -0.5 V; (d) SP distribution measured in dark under short circuit condition; (e) SP image measured in dark with bias voltage of +0.5 V (positive sign means forward bias); (f) SP image measured in dark with bias voltage of +0.8 V; (g) SP image measured in dark with bias voltage of +1 V; (h) SP image measured under illumination and short circuit condition and (i) SP image measured under illumination and open circuit condition.

5.2.2.2 Study the degradation in perovskite layer using KPFM

One of the main problems of the perovskite solar cells is their instability. Even after substituting the buffer layers with inorganic materials, perovskite solar cells still degrade quickly in moisture because the perovskite layer itself is unstable. To improve the stability, it is essential to locate the degradation center first. Researchers conjecture that the degradation starts at grain boundaries and perovskite solar cells with different grain sizes were fabricated to test their stability [100]. With KPFM, the degradation center can be directly observed by performing in-situ characterization of the SP change in grain and grain boundaries of perovskite layer while it being exposed to moisture. Since the change in SP comes with the degradation of the perovskite layer, by monitoring the SP change, degradation centers can be identified.

To sum up, KPFM is an important tool in the characterization of semiconductor devices. This thesis provided a way to improve the resolution of KPFM system and demonstrated its application in the characterizations of solar cells.

BIBLIOGRAPHY

[1] W. Melitz, J. Shen, A. C. Kummel, and S. Lee, "Kelvin probe force microscopy and its application," *Surface Science Reports,* vol. 66, pp. 1-27, Jan 2011.

[2] A. Doukkali, S. Ledain, C. Guasch, and J. Bonnet, "Surface potential mapping of biased pn junction with kelvin probe force microscopy: application to cross-section devices," *Applied Surface Science,* vol. 235, pp. 507-512, Aug 31 2004.

[3] S. A. Burke, J. M. LeDue, Y. Miyahara, J. M. Topple, S. Fostner, and P. Grutter, "Determination of the local contact potential difference of PTCDA on NaCl: a comparison of techniques," *Nanotechnology,* vol. 20, Jul 1 2009.

[4] T. Machleidt, E. Sparrer, D. Kapusi, and K. H. Franke, "Deconvolution of Kelvin probe force microscopy measurements-methodology and application," *Measurement Science & Technology,* vol. 20, Aug 2009.

[5] H. O. Jacobs, P. Leuchtmann, O. J. Homan, and A. Stemmer, "Resolution and contrast in Kelvin probe force microscopy," *Journal of Applied Physics,* vol. 84, pp. 1168-1173, 1998.

[6] E. Strassburg, A. Boag, and Y. Rosenwaks, "Reconstruction of electrostatic force microscopy images," *Review of Scientific Instruments,* vol. 76, p. 083705, 2005.

[7] A. Schwarzman, E. Grunbaum, E. Strassburg, E. Lepkifker, A. Boag, Y. Rosenwaks, *et al.*, "Nanoscale potential distribution across multiquantum well structures: Kelvin probe force microscopy and secondary electron imaging," *Journal of Applied Physics,* vol. 98, p. 084310, 2005.

[8] G. Cohen, E. Halpern, S. U. Nanayakkara, J. M. Luther, C. Held, R. Bennewitz, *et al.*, "Reconstruction of surface potential from Kelvin probe force microscopy images," *Nanotechnology,* vol. 24, p. 295702, 2013.

[9] G. Binnig, C. F. Quate, and C. Gerber, "Atomic Force Microscope," *Physical Review Letters,* vol. 56, pp. 930-933, Mar 3 1986.

[10] Y. Martin, C. C. Williams, and H. K. Wickramasinghe, "Atomic force microscope ‐ force mapping and profiling on a sub 100 ‐ Å scale," *Journal of Applied Physics,* vol. 61, pp. 4723-4729, 1987.

[11] G. X. Li, Y. L. Li, H. B. Liu, Y. B. Guo, Y. J. Li, and D. B. Zhu, "Architecture of graphdiyne nanoscale films," *Chemical Communications,* vol. 46, pp. 3256-3258, 2010.

[12] J. R. Matey and J. Blanc, "Scanning Capacitance Microscopy," *Journal of Applied Physics,* vol. 57, pp. 1437-1444, 1985.

[13] J. W. Hong, S. I. Park, and Z. G. Khim, "Measurement of hardness, surface potential, and charge distribution with dynamic contact mode electrostatic force microscope," *Review of Scientific Instruments*, vol. 70, pp. 1735-1739, Mar 1999.

[14] P. Eyben, M. Xu, N. Duhayon, T. Clarysse, S. Callewaert, and W. Vandervorst, "Scanning spreading resistance microscopy and spectroscopy for routine and quantitative two-dimensional carrier profiling," *Journal of Vacuum Science & Technology B*, vol. 20, pp. 471-478, Jan-Feb 2002.

[15] C. C. Williams, W. P. Hough, and S. A. Rishton, "Scanning Capacitance Microscopy on a 25 Nm Scale," *Applied Physics Letters*, vol. 55, pp. 203-205, Jul 10 1989.

[16] G. Y. Li, B. Mao, F. Lan, and L. M. Liu, "Practical aspects of single-pass scan Kelvin probe force microscopy," *Review of Scientific Instruments*, vol. 83, Nov 2012.

[17] M. Nonnenmacher, M. o'Boyle, and H. K. Wickramasinghe, "Kelvin probe force microscopy," *Applied physics letters*, vol. 58, pp. 2921-2923, 1991.

[18] D. Ziegler, J. Rychen, N. Naujoks, and A. Stemmer, "Compensating electrostatic forces by single-scan Kelvin probe force microscopy," *Nanotechnology*, vol. 18, p. 225505, 2007.

[19] N. Dey, L. Blanc‐Feraud, C. Zimmer, P. Roux, Z. Kam, J. C. Olivo‐Marin, *et al.*, "Richardson–Lucy algorithm with total variation regularization for 3D confocal microscope deconvolution," *Microscopy research and technique*, vol. 69, pp. 260-266, 2006.

[20] See http://www.brukerafmprobes.com/p-3392-scm-pit.aspx for SEM images and detailed parameters of the SCM-PIT probe.

[21] X.-C. Tai and C. Wu, "Augmented Lagrangian method, dual methods and split Bregman iteration for ROF model," in *International Conference on Scale Space and Variational Methods in Computer Vision*, 2009, pp. 502-513.

[22] C. Li, W. Yin, H. Jiang, and Y. Zhang, "An efficient augmented Lagrangian method with applications to total variation minimization," *Computational Optimization and Applications*, vol. 56, pp. 507-530, 2013.

[23] S. H. Chan, R. Khoshabeh, K. B. Gibson, P. E. Gill, and T. Q. Nguyen, "An augmented Lagrangian method for total variation video restoration," *IEEE Transactions on Image Processing*, vol. 20, pp. 3097-3111, 2011.

[24] A. Caboussat, R. Glowinski, and V. Pons, "An augmented Lagrangian approach to the numerical solution of a non-smooth eigenvalue problem," *Journal of Numerical Mathematics*, vol. 17, pp. 3-26, 2009.

[25] Y. Wang, J. Yang, W. Yin, and Y. Zhang, "A new alternating minimization algorithm for total variation image reconstruction," *SIAM Journal on Imaging Sciences*, vol. 1, pp. 248-272, 2008.

[26] F. C. Krebs, "Fabrication and processing of polymer solar cells: A review of printing and coating techniques," *Solar Energy Materials and Solar Cells,* vol. 93, pp. 394-412, Apr 2009.

[27] H. Hoppe and N. S. Sariciftci, "Organic solar cells: An overview," *Journal of Materials Research,* vol. 19, pp. 1924-1945, Jul 2004.

[28] T. L. Benanti and D. Venkataraman, "Organic solar cells: An overview focusing on active layer morphology," *Photosynthesis Research,* vol. 87, pp. 73-81, Jan 2006.

[29] S. E. Shaheen, D. S. Ginley, and G. E. Jabbour, "Organic-based photovoltaics. toward low-cost power generation," *Mrs Bulletin,* vol. 30, pp. 10-19, Jan 2005.

[30] S. I. Na, S. S. Kim, J. Jo, and D. Y. Kim, "Efficient and Flexible ITO-Free Organic Solar Cells Using Highly Conductive Polymer Anodes," *Advanced Materials,* vol. 20, pp. 4061-+, Nov 3 2008.

[31] C. J. Brabec, N. S. Sariciftci, and J. C. Hummelen, "Plastic solar cells," *Advanced Functional Materials,* vol. 11, pp. 15-26, Feb 2001.

[32] H. Kallmann and M. Pope, "Photovoltaic effect in organic crystals," *The Journal of Chemical Physics,* vol. 30, pp. 585-586, 1959.

[33] C. W. Tang, "Two ‐ layer organic photovoltaic cell," *Applied Physics Letters,* vol. 48, pp. 183-185, 1986.

[34] G. Yu, J. Gao, J. C. Hummelen, F. Wudl, and A. J. Heeger, "Polymer Photovoltaic Cells - Enhanced Efficiencies Via a Network of Internal Donor-Acceptor Heterojunctions," *Science,* vol. 270, pp. 1789-1791, Dec 15 1995.

[35] M. A. Green, K. Emery, Y. Hishikawa, W. Warta, and E. D. Dunlop, "Solar cell efficiency tables (Version 45)," *Progress in Photovoltaics,* vol. 23, pp. 1-9, Jan 2015.

[36] F. Lan and G. Li, "Direct observation of hole transfer from semiconducting polymer to carbon nanotubes," *Nano letters,* vol. 13, pp. 2086-2091, 2013.

[37] E. Kymakis, I. Alexandrou, and G. A. J. Amaratunga, "High open-circuit voltage photovoltaic devices from carbon-nanotube-polymer composites," *Journal of Applied Physics,* vol. 93, pp. 1764-1768, Feb 1 2003.

[38] S. Q. Ren, M. Bernardi, R. R. Lunt, V. Bulovic, J. C. Grossman, and S. Gradecak, "Toward Efficient Carbon Nanotube/P3HT Solar Cells: Active Layer Morphology, Electrical, and Optical Properties," *Nano Letters,* vol. 11, pp. 5316-5321, Dec 2011.

[39] B. J. Landi, R. P. Raffaelle, S. L. Castro, and S. G. Bailey, "Single-wall carbon nanotube-polymer solar cells," *Progress in Photovoltaics,* vol. 13, pp. 165-172, Mar 2005.

[40] E. Kymakis and G. A. J. Amaratunga, "Single-wall carbon nanotube/conjugated polymer photovoltaic devices," *Applied Physics Letters,* vol. 80, pp. 112-114, Jan 7 2002.

[41] C. Bounioux, E. A. Katz, and R. Yerushalmi-Rozen, "Conjugated polymers - carbon nanotubes-based functional materials for organic photovoltaics: a critical review," *Polymers for Advanced Technologies,* vol. 23, pp. 1129-1140, Aug 2012.

[42] S. Berson, R. de Bettignies, S. Bailly, S. Guillerez, and B. Jousselme, "Elaboration of P3HT/CNT/PCBM composites for organic photovoltaic cells," *Advanced Functional Materials,* vol. 17, pp. 3363-3370, Nov 5 2007.

[43] L. Q. Ren, S. R. Wang, M. Holtz, and J. J. Qiu, "The synergistic effect of nanocrystal integration and process optimization on solar cell efficiency," *Nanotechnology,* vol. 23, Feb 24 2012.

[44] R. L. Patyk, B. S. Lomba, A. F. Nogueira, C. A. Furtado, A. P. Santos, R. M. Q. Mello*, et al.*, "Carbon nanotube-polybithiophene photovoltaic devices with high open-circuit voltage," *Physica Status Solidi-Rapid Research Letters,* vol. 1, pp. R43-R45, Jan 2007.

[45] E. Kymakis and G. A. J. Amaratunga, "Carbon nanotubes as electron acceptors in polymeric photovoltaics," *Reviews on Advanced Materials Science,* vol. 10, pp. 300-305, Oct 2005.

[46] L. M. Liu, W. E. Stanchina, and G. Y. Li, "Effects of semiconducting and metallic single-walled carbon nanotubes on performance of bulk heterojunction organic solar cells," *Applied Physics Letters,* vol. 94, Jun 8 2009.

[47] E. Kymakis, N. Kornilios, and E. Koudoumas, "Carbon nanotube doping of P3HT: PCBM photovoltaic devices," *Journal of Physics D-Applied Physics,* vol. 41, Aug 21 2008.

[48] H. Derbal-Habak, C. Bergeret, J. Cousseau, and J. M. Nunzi, "Improving the current density J(SC) of organic solar cells P3HT:PCBM by structuring the photoactive layer with functionalized SWCNTs," *Solar Energy Materials and Solar Cells,* vol. 95, pp. S53-S56, May 2011.

[49] C. Li, Y. H. Chen, Y. B. Wang, Z. Iqbal, M. Chhowalla, and S. Mitra, "A fullerene-single wall carbon nanotube complex for polymer bulk heterojunction photovoltaic cells," *Journal of Materials Chemistry,* vol. 17, pp. 2406-2411, Jun 21 2007.

[50] M. C. Wu, Y. Y. Lin, S. Chen, H. C. Liao, Y. J. Wu, C. W. Chen*, et al.*, "Enhancing light absorption and carrier transport of P3HT by doping multi-wall carbon nanotubes," *Chemical Physics Letters,* vol. 468, pp. 64-68, Jan 13 2009.

[51] S. Chaudhary, H. W. Lu, A. M. Muller, C. J. Bardeen, and M. Ozkan, "Hierarchical placement and associated optoelectronic impact of carbon nanotubes in polymer-fullerene solar cells," *Nano Letters,* vol. 7, pp. 1973-1979, Jul 2007.

[52] J. Geng, B. S. Kong, S. B. Yang, S. C. Youn, S. Park, T. Joo, *et al.*, "Effect of SWNT defects on the electron transfer properties in P3HT/SWNT hybrid materials," *Advanced Functional Materials,* vol. 18, pp. 2659-2665, 2008.

[53] A. Nish, J.-Y. Hwang, J. Doig, and R. J. Nicholas, "Direct spectroscopic evidence of energy transfer from photo-excited semiconducting polymers to single-walled carbon nanotubes," *Nanotechnology,* vol. 19, p. 095603, 2008.

[54] S. D. Stranks, C. Weisspfennig, P. Parkinson, M. B. Johnston, L. M. Herz, and R. J. Nicholas, "Ultrafast Charge Separation at a Polymer-Single-Walled Carbon Nanotube Molecular Junction," *Nano Letters,* vol. 11, pp. 66-72, Jan 2011.

[55] J. S. Lauret, C. Voisin, G. Cassabois, C. Delalande, P. Roussignol, O. Jost, *et al.*, "Ultrafast carrier dynamics in single-wall carbon nanotubes," *Physical Review Letters,* vol. 90, Feb 7 2003.

[56] S. Reich, M. Dworzak, A. Hoffmann, C. Thomsen, and M. S. Strano, "Excited-state carrier lifetime in single-walled carbon nanotubes," *Physical Review B,* vol. 71, Jan 2005.

[57] N. M. Dissanayake and Z. H. Zhong, "Unexpected Hole Transfer Leads to High Efficiency Single-Walled Carbon Nanotube Hybrid Photovoltaic," *Nano Letters,* vol. 11, pp. 286-290, Jan 2011.

[58] N. A. Nismy, K. D. G. I. Jayawardena, A. A. D. T. Adikaari, and S. R. P. Silva, "Photoluminescence Quenching in Carbon Nanotube-Polymer/Fullerene Films: Carbon Nanotubes as Exciton Dissociation Centres in Organic Photovoltaics," *Advanced Materials,* vol. 23, pp. 3796-+, Sep 1 2011.

[59] T. Umeyama, N. Kadota, N. Tezuka, Y. Matano, and H. Imahori, "Photoinduced energy transfer in composites of poly[(p-phenylene-1,2-vinylene)-co-(p-phenylene-1,1-vinylidene)] and single-walled carbon nanotubes," *Chemical Physics Letters,* vol. 444, pp. 263-267, Aug 27 2007.

[60] P. H. Tan, A. G. Rozhin, T. Hasan, P. Hu, V. Scardaci, W. I. Milne, *et al.*, "Photoluminescence spectroscopy of carbon nanotube bundles: Evidence for exciton energy transfer," *Physical Review Letters,* vol. 99, Sep 28 2007.

[61] T. Schuettfort, H. J. Snaith, A. Nish, and R. J. Nicholas, "Synthesis and spectroscopic characterization of solution processable highly ordered polythiophene-carbon nanotube nanohybrid structures," *Nanotechnology,* vol. 21, Jan 15 2010.

[62] B. J. Bauer, J. A. Fagan, E. K. Hobbie, J. Chun, and V. Bajpai, "Chromatographic fractionation of SWNT/DNA dispersions with on-line multi-angle light scattering," *Journal of Physical Chemistry C,* vol. 112, pp. 1842-1850, Feb 14 2008.

[63] T. J. Prosa, M. J. Winokur, J. Moulton, P. Smith, and A. J. Heeger, "X-Ray Structural Studies of Poly(3-Alkylthiophenes) - an Example of an Inverse Comb," *Macromolecules,* vol. 25, pp. 4364-4372, Aug 17 1992.

[64] S. Ren, M. Bernardi, R. R. Lunt, V. Bulovic, J. C. Grossman, and S. Gradecak, "Toward efficient carbon nanotube/P3HT solar cells: Active layer morphology, electrical, and optical properties," *Nano letters,* vol. 11, pp. 5316-5321, 2011.

[65] A. Nish, J. Y. Hwang, J. Doig, and R. J. Nicholas, "Direct spectroscopic evidence of energy transfer from photo-excited semiconducting polymers to single-walled carbon nanotubes," *Nanotechnology,* vol. 19, Mar 5 2008.

[66] C. Goh, R. J. Kline, M. D. McGehee, E. N. Kadnikova, and J. M. J. Frechet, "Molecular-weight-dependent mobilities in regioregular poly(3-hexyl-thiophene) diodes," *Applied Physics Letters,* vol. 86, Mar 21 2005.

[67] Murgatro.Pn, "Theory of Space-Charge-Limited Current Enhanced by Frenkel Effect," *Journal of Physics D-Applied Physics,* vol. 3, pp. 151-&, 1970.

[68] J. M. Ball, M. M. Lee, A. Hey, and H. J. Snaith, "Low-temperature processed meso-superstructured to thin-film perovskite solar cells," *Energy & Environmental Science,* vol. 6, pp. 1739-1743, 2013.

[69] N. J. Jeon, J. H. Noh, Y. C. Kim, W. S. Yang, S. Ryu, and S. I. Seok, "Solvent engineering for high-performance inorganic–organic hybrid perovskite solar cells," *Nature materials,* vol. 13, pp. 897-903, 2014.

[70] D. Liu and T. L. Kelly, "Perovskite solar cells with a planar heterojunction structure prepared using room-temperature solution processing techniques," *Nature photonics,* vol. 8, pp. 133-138, 2014.

[71] H. S. Jung and N. G. Park, "Perovskite solar cells: from materials to devices," *small,* vol. 11, pp. 10-25, 2015.

[72] J.-P. Correa-Baena, A. Abate, M. Saliba, W. Tress, T. J. Jacobsson, M. Grätzel, *et al.*, "The rapid evolution of highly efficient perovskite solar cells," *Energy & Environmental Science,* 2017.

[73] M. Liu, M. B. Johnston, and H. J. Snaith, "Efficient planar heterojunction perovskite solar cells by vapour deposition," *Nature,* vol. 501, pp. 395-398, 2013.

[74] A. Kojima, K. Teshima, Y. Shirai, and T. Miyasaka, "Organometal halide perovskites as visible-light sensitizers for photovoltaic cells," *Journal of the American Chemical Society,* vol. 131, pp. 6050-6051, 2009.

[75] P. Docampo, J. M. Ball, M. Darwich, G. E. Eperon, and H. J. Snaith, "Efficient organometal trihalide perovskite planar-heterojunction solar cells on flexible polymer substrates," *Nature communications,* vol. 4, 2013.

[76] Y. Sun, J. H. Seo, C. J. Takacs, J. Seifter, and A. J. Heeger, "Inverted polymer solar cells integrated with a low ‐ temperature ‐ annealed sol ‐ gel ‐ derived ZnO film as an electron transport layer," *Advanced Materials,* vol. 23, pp. 1679-1683, 2011.

[77] Z. He, C. Zhong, S. Su, M. Xu, H. Wu, and Y. Cao, "Enhanced power-conversion efficiency in polymer solar cells using an inverted device structure," *Nature Photonics,* vol. 6, pp. 591-595, 2012.

[78] Z. Zhai, X. Huang, M. Xu, J. Yuan, J. Peng, and W. Ma, "Greatly Reduced Processing Temperature for a Solution‐Processed NiOx Buffer Layer in Polymer Solar Cells," *Advanced Energy Materials,* vol. 3, pp. 1614-1622, 2013.

[79] J. You, L. Meng, T.-B. Song, T.-F. Guo, Y. M. Yang, W.-H. Chang, *et al.*, "Improved air stability of perovskite solar cells via solution-processed metal oxide transport layers," *Nature nanotechnology,* vol. 11, pp. 75-81, 2016.

[80] A. Miyata, A. Mitioglu, P. Plochocka, O. Portugall, J. T.-W. Wang, S. D. Stranks, *et al.*, "Direct measurement of the exciton binding energy and effective masses for charge carriers in organic-inorganic tri-halide perovskites," *Nature Physics,* vol. 11, pp. 582-587, 2015.

[81] C.-S. Jiang, M. Yang, Y. Zhou, B. To, S. U. Nanayakkara, J. M. Luther, *et al.*, "Carrier separation and transport in perovskite solar cells studied by nanometre-scale profiling of electrical potential," *Nature communications,* vol. 6, 2015.

[82] V. W. Bergmann, S. A. Weber, F. J. Ramos, M. K. Nazeeruddin, M. Grätzel, D. Li, *et al.*, "Real-space observation of unbalanced charge distribution inside a perovskite-sensitized solar cell," *Nature communications,* vol. 5, 2014.

[83] E. Edri, S. Kirmayer, S. Mukhopadhyay, K. Gartsman, G. Hodes, and D. Cahen, "Elucidating the charge carrier separation and working mechanism of CH3NH3PbI3−xClx perovskite solar cells," *Nature communications,* vol. 5, 2014.

[84] M. Jiang, J. Wu, F. Lan, Q. Tao, D. Gao, and G. Li, "Enhancing the performance of planar organo-lead halide perovskite solar cells by using a mixed halide source," *Journal of Materials Chemistry A,* vol. 3, pp. 963-967, 2015.

[85] C. Pacholski, A. Kornowski, and H. Weller, "Self‐assembly of ZnO: from nanodots to nanorods," *Angewandte Chemie International Edition,* vol. 41, pp. 1188-1191, 2002.

[86] R. Saive, M. Scherer, C. Mueller, D. Daume, J. Schinke, M. Kroeger, *et al.*, "Imaging the electric potential within organic solar cells," *Advanced Functional Materials,* vol. 23, pp. 5854-5860, 2013.

[87] Q. Chen, L. Mao, Y. Li, T. Kong, N. Wu, C. Ma, *et al.*, "Quantitative operando visualization of the energy band depth profile in solar cells," *Nature communications,* vol. 6, 2015.

[88] S. Ryu, J. H. Noh, N. J. Jeon, Y. C. Kim, W. S. Yang, J. Seo, *et al.*, "Voltage output of efficient perovskite solar cells with high open-circuit voltage and fill factor," *Energy & Environmental Science,* vol. 7, pp. 2614-2618, 2014.

[89] H.-W. Chen, T.-Y. Huang, T.-H. Chang, Y. Sanehira, C.-W. Kung, C.-W. Chu, *et al.*, "Efficiency Enhancement of Hybrid Perovskite Solar Cells with MEH-PPV Hole-Transporting Layers," *Scientific Reports*, vol. 6, 2016.

[90] Z. Zhu, Y. Bai, T. Zhang, Z. Liu, X. Long, Z. Wei, *et al.*, "High‐Performance Hole‐Extraction Layer of Sol–Gel‐Processed NiO Nanocrystals for Inverted Planar Perovskite Solar Cells," *Angewandte Chemie*, vol. 126, pp. 12779-12783, 2014.

[91] J. Kong, J. Lee, Y. Jeong, M. Kim, S.-O. Kang, and K. Lee, "Biased internal potential distributions in a bulk-heterojunction organic solar cell incorporated with a TiOx interlayer," *Applied Physics Letters*, vol. 100, p. 213305, 2012.

[92] D. S. Charrier, M. Kemerink, B. E. Smalbrugge, T. de Vries, and R. A. Janssen, "Real versus measured surface potentials in scanning Kelvin probe microscopy," *Acs Nano*, vol. 2, pp. 622-626, 2008.

[93] A. Zaban, M. Greenshtein, and J. Bisquert, "Determination of the electron lifetime in nanocrystalline dye solar cells by open‐circuit voltage decay measurements," *ChemPhysChem*, vol. 4, pp. 859-864, 2003.

[94] A. Baumann, K. Tvingstedt, M. Heiber, S. Väth, C. Momblona, H. Bolink, *et al.*, "Persistent photovoltage in methylammonium lead iodide perovskite solar cells," *Apl Materials*, vol. 2, p. 081501, 2014.

[95] H. Nagaoka, F. Ma, D. W. deQuilettes, S. M. Vorpahl, M. S. Glaz, A. E. Colbert, *et al.*, "Zr incorporation into TiO2 electrodes reduces hysteresis and improves performance in hybrid perovskite solar cells while increasing carrier lifetimes," *The journal of physical chemistry letters*, vol. 6, pp. 669-675, 2015.

[96] L. Meng, J. You, T.-F. Guo, and Y. Yang, "Recent advances in the inverted planar structure of perovskite solar cells," *Accounts of chemical research*, vol. 49, pp. 155-165, 2015.

[97] R. F. Pease and S. Y. Chou, "Lithography and other patterning techniques for future electronics," *Proceedings of the IEEE*, vol. 96, pp. 248-270, 2008.

[98] S. Y. Chou, P. R. Krauss, W. Zhang, L. Guo, and L. Zhuang, "Sub-10 nm imprint lithography and applications," *Journal of Vacuum Science & Technology B: Microelectronics and Nanometer Structures Processing, Measurement, and Phenomena*, vol. 15, pp. 2897-2904, 1997.

[99] M. D. Austin, H. Ge, W. Wu, M. Li, Z. Yu, D. Wasserman, *et al.*, "Fabrication of 5 nm linewidth and 14 nm pitch features by nanoimprint lithography," *Applied Physics Letters*, vol. 84, pp. 5299-5301, 2004.

[100] Q. Wang, B. Chen, Y. Liu, Y. Deng, Y. Bai, Q. Dong, *et al.*, "Scaling behavior of moisture-induced grain degradation in polycrystalline hybrid perovskite thin films," *Energy & Environmental Science*, 2017.